UNIVERSITÀ
DEGLI STUDI
DI PADOVA

Sede Amministrativa: Università degli Studi di Padova

Centro Interdipartimentale di Studi ed Attività Spaziali

SCUOLA DI DOTTORATO DI RICERCA IN : Scienze Tecnologie e Misure Spaziali
INDIRIZZO: Astronautica e Scienze da Satellite
CICLO XXIV

OPTICAL VORTEX DIFFRACTIVE OPTICS FOR TERRESTRIAL AND SPACE APPLICATIONS

Direttore della Scuola : Ch.mo Prof. Giampiero Naletto
Coordinatore d'indirizzo : Ch.mo Prof. Giampiero Naletto
Supervisore : Ch.mo Prof. Cesare Barbieri
Co-supervisore : Dott. Fabrizio Tamburini

Dottorando : Elettra Mari

A tutti quelli che hanno creduto in me,
nonostante il loro buon senso.

"What can be asserted without evidence
can also be dismissed without evidence."
Christopher Hitchens

Abstract

Optical vortices (OVs) are topological dislocations in light beams due to phase singularities associated with angular momentum (OAM). The wavefront of the waves that make up the light beam that carries OAM is twisted around its axis of propagation with a helicoidal shape. Along the axis of the helicoid the phase is undefined, so the waves cancel each other out. Hence, due to the destructive interference, the intensity (linear momentum) distribution of a vortex exhibits a dark core that is surrounded by a 'ring of light'. The vortex is characterized by a number, called the *topological charge* that indicates how many full 360 degree twists the wavefront phase makes around the beam axis within one wavelength.

In the past decade, the OAM of light beams has attained a large attention in many applications in science. Among these, the most promising are those in optical communications, nanotechnologies, biology and astronomy.

Optical vortices may be generated naturally and by a variety of different techniques, one of which is the use of a diffractive vortex mask the spiral phase plate. The spiral phase plate is a helicoidal lens that looks like a spiral staircase with a certain number of steps, that imposes an azimuthally dependent phase delay on an incident optical wavefront.

The objective of the research presented in this dissertation is to study the properties of these particular optical devices and some of their possible applications.

Firstly, we have studied the spiral phase plate in the visible light domain. We have found, through numerical simulations and experimental tests using an optical bench, a relationship between the number of steps that build the phase gap, and the topological charge imposed onto incident light beam.

This result has allowed us to optimize the design parameters of the spiral phase plates for astronomical purposes that we have manufactured on PMMA. We have assembled our first prototype of the optical vortex coronagraph based on the insertion of a spiral phase plate in the optical path of a telescope. Coronagraphs are instruments designed to block the light from a bright source so that nearby much fainter sources can be directly imaged without glare. The optical

vortex coronagraph (OVC) exploits the dark area in the intensity distribution of even-topologically charged optical vortices produced by a spiral phase plate, attenuating the light of the bright source but keeping the light from secondary sources intact.

In this framework of our project we performed coronagraphic tests at the Asiago 122 cm optical telescope and managed to extinguish the light of one component of a stellar double system by almost one order of magnitude.

The astronomical use of the spiral phase plate has prompted us to investigate the efficiency of this device with respect to the angular distance at which the secondary source crosses the central singularity. Through numerical simulations we found that the optical vortex coronagraph works also above the limit posed by the Rayleigh criterion. The research has led to the proposition of a new method to determine the angular separation between two sources above the sub-Rayleigh condition, exploiting the asymmetric intensity distribution of the OVs produced by a double system that crosses the spiral phase plate.

As Maxwell's equations are equally valid for all wavelengths, optical vortices can be produced also at radio frequencies. Based on this fundamental principle we have studied diffractive optics also in the radio domain, presenting the first experimental evidence of a radio vortex. In order to do so, we built a reflective spiral phase plate made from Styrofoam clad with aluminum foil, with a design based on the results obtained in optics. The experimental verification that OAM-carrying beams can be generated and exploited by using radio techniques paved the way to the outdoor radio communication experiment that we subsequently carried out.

In this real-world experiment we were able to show that it is possible to simultaneously transmit two radio channels on the same frequency by physically encode the channels in two different orbital angular momentum states. This novel radio technique allows, in principle, the implementation of an infinite number of channels in a given band centered on one and the same carrier frequency. Our experimental findings that electromagnetic OAM can be used for radio and TV transmission are likely to open new perspectives on wireless communications and radio-based science.

Sommario

I vortici ottici, sono caratteristiche topologiche dell'onda, legate alle singolaritá di fase nei campi elettromagnetici che trasportano momento angolare orbitale (OAM). Il fronte d'onda ha forma elicoidale, si attorciglia spiraleggiando attorno all'asse di propagazione in cui la fase é indefinita. Lungo l'asse dell'elica le onde fanno interferenza distruttiva le une con le altre, con il risultato di una distribuzione d'intensitá caratterizzato da una regione buia nel centro, circondata da luce a forma di ciambella. I vortici ottici sono caratterizzati da un valore, detto *carica topologica* che indica quante volte la fase compie una completa variazione di 360 gradi attorno all'asse ottico in una lunghezza d'onda.

I vortici ottici possono essere prodotti con l'utilizzo di strumenti ottici. In particolare in questa tesi sono state studiate delle particolare ottiche diffrattive dette spirali di fase. Le spirali di fase sono ottiche il cui spessore cresce gradualmente intorno ad un asse; somigliano a scale a chiocciola, costruite con un certo numero di scalini ed impongono al fascio incidente un ritardo di fase che dipende dall'angolo azimutale.

L'oggetto di questa ricerca é lo studio delle proprietá delle spirali di fase, la caratterizzazione e alcune possibili applicazioni.

Lo studio si é inizialmente concentrato sulle spirali da fase nel range del visibile. Attraverso simulazioni numeriche ed esperimenti al banco ottico, siamo riusciti a ricavare una relazione tra il numero degli scalini che costruiscono il salto di fase nella spirale e la carica topologica che viene imposta al fascio incidente.

Questo risultato ci ha permesso di ottimizzare i parametri di costruzione della spirale realizzata in PMMA per applicazioni astronomiche. Abbiamo infatti assemblato il primo prototipo di un coronografo a vortici ottici, nel cui cammino ottico é stata inserita la spirale di fase realizzata in base ai parametri da noi definiti. I coronografi, in generale, sono strumenti progettati per bloccare la luce proveniente da una sorgente brillante in modo tale da poter osservare direttamente delle sorgenti piú deboli nelle vicinanze. Il coronografo a vortici ottici sfrutta la regione buia nella distribuzione d'intensitá di un vortice ottico per attenuare la luce di una sorgente luminosa, senza

diminuire l'intensitá della sorgente secondaria.

Abbiamo testato il nostro prototipo al telescopio 'Galileo' 122cm di Asiago, attenuando l'intensitá di una componente del sistema stellare doppio Epsilon^2 Lyrae di quasi un ordine di magnitudine.

L'applicazione astronomica della spirale di fase ci ha spinto allo studio delle sua efficienza, ovvero del contrasto che si ottiene nella zona buia del vortice ottico, a diverse distanze angolari della sorgente secondaria rispetto alla singolaritá centrale della spirale. Simulazioni numeriche hanno mostrato che il coronografo a vortici ottici funziona anche al di sotto del limite di risoluzione di Rayleigh. La ricerca si é sviluppata fino alla formulazione di un nuovo metodo per determinare la distanza angolare tra due sorgenti distanti meno del criterio di Rayleigh. Il nuovo metodo sfrutta la distribuzione d'intensitá asimmetrica dei vortici ottici prodotti dalla sorgente secondaria che passa attraverso la spirale di fase, ma non in corrispondenza della singolaritá centrale.

Poiché le equazioni di Maxwell sono valide su tutto lo spettro elettromagnetico, i vortici possono essere prodotti anche in diverse bande rispetto al visibile. Basandoci su questo fondamentale principio abbiamo studiato delle ottiche diffrattive per la produzione di vortici nel range del radio. Abbiamo costruito con polistirolo e alluminio una spirale di fase basandoci sui risultati trovati nel visibile ed abbiamo ottenuto la prima evidenza sperimentale di un vortice radio. La verifica sperimentale della possibilitá di generare e sfruttare vortici radio ha spianato la strada all'esperimento successivo che é stato condotto nel campo della comunicazione radio.

Abbiamo compiuto la prima trasmissione OAM in cui due segnali sono stati trasmessi contemporaneamente e sulla stessa frequenza, su due canali radio codificati in due diversi stati di momento angolare orbitale. Questa nuova tecnica radio permette, in teoria, di codificare un infinito numero di canali in una singola banda centrata su una frequenza. I risultati dei nostri esperimenti nel dominio del radio aprono nuove prospettive nel mondo della comunicazione.

Contents

Chapter 1

Introduction

Vortices are an appealing feature of waves that are found in nature. The space-time evolution of a beam of waves is ruled by its phase front topology. When the phase front has a helicoidal shape owing to the circulation of momentum around the helix axis [1] the wave is carrying an *optical vortex* [2].

Optical vortices (OVs) are phase defects embedded in light beams that carry orbital angular momentum [1] (OAM). OAM of light is a new degree of freedom associated to the spatial field distribution of an optical beam. In optics, vortices are characterized by a dark core in the intensity (linear momentum) in a beam of light, due to the destructive interference along the optical axis, where the phase in undefined.

OAM and optical vortices have found practical applications in many fields such as radar [3], nanotechnology [4] and quantum experiments [5]. In particular we mention two applications in astronomy and space sciences that we have drawn on in this work: improve the resolving power of diffraction-limited optical instruments [6] and facilitate the detection of extrasolar planets [7].

Several methods may be used to imprint OVs onto a incident beam. Among them, the most efficient are phase masks [8] and computer-generated holograms [9]. In this thesis we have studied the diffractive optics called spiral phase plate, a particular kind of phase mask. The spiral phase plate is a helicoidal lens with a thickness that increases proportionally to the azimuthal angle. As a consequence, an incident beam of electromagnetic waves acquires a helicoidal phase retard on its wavefront.

This thesis covers three main topics:

1. Study of peculiar properties of an optical and high quality spiral phase plate;

2. Coronagraphic astronomical application in the visible range;

3. Study of electromagnetic vortices and their application in communication within the radio

frequency range.

The chapters in this thesis are organized as follows. A brief introduction to diffractive optics is given in Chapter 2. A literature overview about optical vortices and orbital angular momentum is presented in Chapter 3. In Chapter 4 we present the fabrication process and tests of two different types of spiral phase plates in the visible wavelength regime. We report the results obtained with our first prototype of the optical vortex coronagraph, mounted at the 122 cm Asiago telescope in Chapter 5. A new optical vortex coronagraph (OVC) method to determine the angular distance between two sources when the separation is sub-Rayleigh is introduced in Chapter 6. The first experimental evidence of a radio vortex is described in Chapter 7. The experimental demonstration of the first radio transmission that encode signals in OAM channels is reported in Chapter 8.

We have used both numerical and experimental methods.

Firstly, we have studied the spiral phase plate in the visible domain. The author of this thesis has developed specific numerical routines to simulate the behaviour of different spiral phase plates built with different number of steps, finding a relationship between the number of steps and the OAM value imposed to incident light beam. The author has confirmed the numerical conclusions in experiments performed by using an optical bench. Based on this result, the author defined the design parameters for the spiral phase plate manufactured on PMMA to be inserted into an optical vortex coronagraph.

Our first prototype of this optical instrument was assembled with the aim of detecting and imaging faint objects near much brighter sources, and it is was mounted and tested at the Asiago 122 cm telescope. We obtain an attenuation of the light from one component of a stellar double system of almost one order of magnitude. The author took part in the campaign of observations, and then she reduced and processed all data, taking into account the lucky imaging technique.

Further and deeper investigation of the properties of these spiral phase plates was then achieved with the writing of new numerical routines, written entirely by the author, that simulate the secondary source crossing the phase mask at different angular distance with respect to the central dislocation. We have discussed the superresolution capabilities of an OVC, and the author contributed to the formulation of a new method that allows the determination of the angular separation between two sources above sub-Rayleigh condition by exploiting the geometrical properties of the optical vortices.

The third part of this thesis is centered on the study of radio vortices. We have studied a solution to build a phase mask for the radio domain. We built a reflective eight steps spiral phase plate made on Styrofoam and aluminum foil, taking into account the results obtained in the visible domain. The author has participated in the preparation and realization of the experiment. The main contribution was the development of numerical routines to simulate the experiment and to

process the collected data.

Finally, we have carried out an outdoor experiment that demonstrate the feasibility of wireless information transfer over large distances that exploits the OAM states of electromagnetic waves. We have encoded and transmitted two independent channels in the same frequency, discriminated only by their OAM. Our findings extend previous indoor laboratory tests in which the transmission of optical OAM states of radio beams were discussed. We demonstrated the possibility of using different orbital angular momentum channels without increasing the frequency bandwidth. The contribution of the author to this experiment was crucial at every stage of the experiment, from the transformation of a commercial parabolic antenna to a vortex reflector for the generation of the OAM channel, to the general organization and performance of the experiment.

Chapter 2

Diffractive optics

Conventional optical devices such as lenses, mirrors and prisms used in optical instruments are based on refraction or reflection. A diffractive optical element (DOE) is a new class of optics that operates on the principle of diffraction. In conventional optical design diffraction is a limitation because it determines the limit resolution of an optical imaging system. The developments of analogue holography (demonstrated in the 1940s and made practical in the 1960s), synthetic aperture radar (1960s), and computer-generated holograms and kinoforms, more generally known as diffractive optical elements (DOE's) (late 1960s) marked the beginning of the development of optical elements based on diffraction. More recently, the combination of diffractive and refractive optical elements, such as a refractive lens corrected by diffractive optics, showed how to achieve new design strategies.

2.1 Diffraction

Diffraction is a phenomenon characteristic of the propagation of a wave which occurs when a wavefront encounters an obstacle in its path. The wavefront is thus altered in its amplitude or phase. The general problem of diffraction is to find an expression of the field over the obstacle.

2.1.1 History

The first reference to diffraction phenomena appears in the work of Leonardo da Vinci (1452-1519). The effects of diffraction were first carefully observed and characterized by Francesco Maria Grimaldi (1618 - 1663), who also coined the term diffraction, from the Latin *diffringere*, 'to break into pieces', referring to light breaking up into different directions. The results of Grimaldi's observations were published posthumously in 1665. The corpuscoular theory, which, at that time, was widely belived to described the propagation of light, could not explain diffraction. In 1818

Fresnel [10], in his memoirs, showed that diffraction can be explained by the application of the wave theory of light that had been advanced by Huygens in 17th century [11].

Diffraction problems are amongst the most difficult ones encountered in optics. The theory of Huygens and Fresnel is by far the most powerful and adequate for the treatment of the majority of problems in instrumental optics.

2.1.2 The Huygens-Fresnel principle

A wavefront that propagates beyond an obstacle may be studied in terms of secondary spherical waves that interfere with each other (Fig.2.1) [12]:

Each area element $d\Sigma$ of a wavefront Σ can be formally considered as a secondary source of spherical waves in phase with the primary one and with amplitude proportional to the amplitude of the primary wave and to that $d\Sigma$ area. The disturbance produced at a point in space can always be obtained as a superposition of all the secondary spherical waves that reach that point.

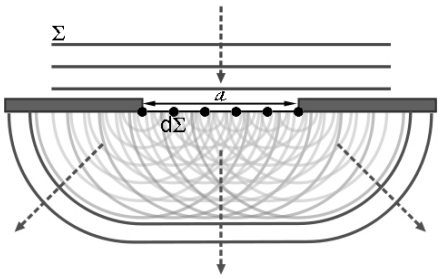

Figure 2.1: Graphical representation of the Huygens - Fresnel principle. Σ is the wavefront, $d\Sigma$ is an area element of the wavefront. a is the size of the aperture.

The Huygens-Fresnel principle provides a good basis for understanding and predicting the wave propagation of light.

The basic idea of the Huygens-Fresnel theory was put on a stronger mathematical basis by Kirchhoff [13, 12]. Kirchhoff's diffraction formula provides a rigorous mathematical foundation for diffraction, based on the wave equation. The assumptions made by Fresnel to arrive at the Huygens - Fresnel equation emerge automatically from the mathematics developed by Kirchhoff.

2.1.3 Fresnel and Fraunhofer approximations

The form of a diffraction pattern can be determined from the sum of the phases and amplitudes of the Huygens wavelets at each point in space. There are various analytical models which can be used to do this including the Fraunhofer diffraction equation for the far field and the Fresnel

diffraction equation for the near field. Most configurations cannot be solved analytically, but can find numerical solutions through finite elements and boundary element methods.

Fresnel number

The Fresnel number F is a dimensionless number used in diffraction theory. It is defined, for an electromagnetic wave passing through an aperture, as:

$$F = \frac{a^2}{L\lambda}$$

where a is the size of the aperture, L is the distance between the screen and the aperture, and λ is the wavelength.

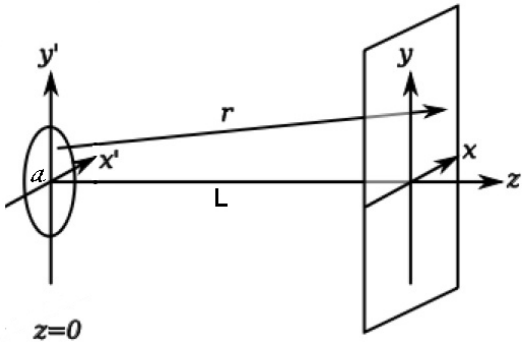

Figure 2.2: Diffraction geometry. Aperture plane (x', y') and image plane (x, y).

Depending on the value of the Fresnel number one can distinguish two different type of diffraction:

- Fresnel approximation $F \geqslant 1$
- Fraunhofer approximation $F \ll 1$

Fresnel diffraction

The electric field at the point (x, y, z) of the image plane is given by:

$$\vec{E}(x, y, z) = \frac{z}{i\lambda} \iint \vec{E}(x', y', 0) \frac{e^{ikr}}{r^2} dx' dy' \tag{2.1.1}$$

where

$$r = \sqrt{(x - x')^2 + (y - y')^2 + z^2} = z\sqrt{1 + \left(\frac{x - x'}{z}\right)^2 + \left(\frac{y - y'}{z}\right)^2} \tag{2.1.2}$$

Using the binomial series expansion

$$\sqrt{1 + \rho} = (1 + \rho)^{1/2} = 1 + \frac{\rho}{2} - \frac{\rho^2}{8} + \cdots \tag{2.1.3}$$

and defining

$$\rho = (x - x')^2 + (y - y')^2 \tag{2.1.4}$$

we can write r as

$$r = z\sqrt{1 + \frac{\rho^2}{z^2}} = z\left[1 + \frac{\rho^2}{2z^2} - \frac{1}{8}\left(\frac{\rho^2}{z^2}\right)^2 + \cdots\right] = z + \frac{\rho^2}{2z} - \frac{\rho^4}{8z^3} + \cdots \tag{2.1.5}$$

In the Fresnel approximation it is assumed that the third term is negligible. To satisfy this assumption, this term has to be much smaller than 2π:

$$k\frac{\rho^4}{8z^3} \ll 2\pi \qquad \text{with} \quad k = \frac{2\pi}{\lambda}$$

so that

$$\frac{\rho^4}{z^3\lambda} \ll 8$$

Multiplying both sides by z^3/λ^3, and substituting the eq. (2.1.4) we have:

$$\frac{[(x - x')^2 + (y - y')^2]^2}{\lambda^4} \ll 8\frac{z^3}{\lambda^3} \tag{2.1.6}$$

If this condition is true for all values of x, x', y, y' the third term in the binomial expression is negligible. In general for the wavelength the conditions $\lambda \ll z$ and $\lambda \ll \rho$ are valid. If it is also valid $\rho \ll z$, we have the *Fresnel approximation* [12]:

$$r \approx z + \frac{(x - x')^2 + (y - y')^2}{2z} \tag{2.1.7}$$

With this approximation, the equation (2.1.1) becomes:

$$\begin{aligned}\vec{E}(x, y, z) =& \frac{e^{ikz}}{i\lambda z}\iint \vec{E}(x', y', 0)\exp\left[\frac{ik}{2z}[(x - x')^2 + (y - y')^2]\right]dx'dy' = \\ =& \frac{e^{ikz}}{i\lambda z}\exp\left[i\frac{k}{2z}(x^2 + y^2)\right]\cdot \\ & \cdot\iint \vec{E}(x', y', 0)\exp\left[i\frac{k}{2z}(x'^2 + y'^2)\right]\exp\left(-i\frac{k}{2z}(xx' + yy')\right)dx'dy'\end{aligned} \tag{2.1.8}$$

This equation represents the electric field vector at point (x, y, z). The Fresnel diffraction gives good results in the region very near the diffraction plane, at distances of the order of tens of λ. Analytical solution of this expression is still only possible in rare cases.

Fraunhofer diffraction

We introduce the *Fraunhofer approximation*. It requires that the image plane, that is at distance z from the aperture plane, is such that this condition applies:

$$z \gg \frac{k(x'^2 + y'^2)}{2} = \frac{\pi(x'^2 + y'^2)}{\lambda}$$

Under these conditions the quadratic term inside the integral in (2.1.8) is negligible, so the distribution of the field in image plane becomes:

$$\vec{E}(x,y,z) = \frac{e^{ikz}}{i\lambda z} \exp\left[i\frac{k}{2z}(x^2+y^2)\right] \iint \vec{E}(x',y',0) \exp\left[-i\frac{k}{2z}(xx'+yy')\right] dx'dy' \qquad (2.1.9)$$

The term in front of the integral is a phase factor that depends on the geometry of the aperture, on the position of the image plane and on the wavelength of the incident radiation. Equation (2.1.9) describes the field in the image plane in terms of superposition of waves emitted by each point of the aperture, seen as source point. Each wave is weighted with a phase factor.

In the Fraunhofer approximation the distribution of the field in the image plane, at constant distance z from the aperture, is proportional to the *Fourier transform* of the aperture function.

2.2 Diffractive Optics

When we talk about devices that control light through diffraction, a number of terms are used: binary optics, kinoforms, computer generated holograms, holographic optical elements *etc*. All of these are diffractive optics elements (DOEs, see Fig.2.3).

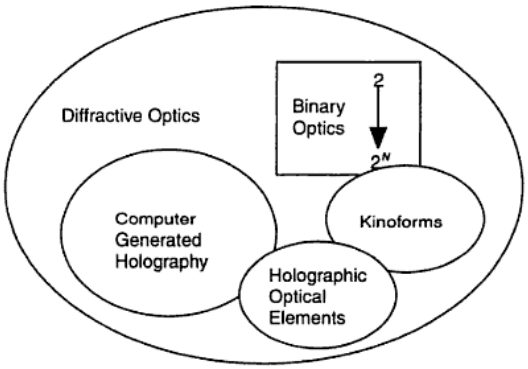

Figure 2.3: Various types of DOEs [14].

We can classify these diffractive optics as follows:

- **Diffractive Optical Elements:** Components that modify wavefronts by segmenting and redirecting the segments through the use of interference and phase control;
- **Kinoform:** Surfaces that control the phase of the incident beam varying smoothly;
- **Binary Optics:** DOE with a discrete number of phase-controlling surfaces. The simplest form is a mask, made by lithography, with two surfaces, which introduce either a 0 or a π-

phase difference on the incident wavefront. When N masks are used, a multilevel binary optic can be generated, usually resulting in 2^N phase levels;

- **Computer-Generated Hologram:** Generated by reducing a calculated interference pattern to a series of phase or amplitude masks;
- **Holographic Optical Element:** DOE generated by the interference of two wavefronts to produce a component that will be used to acts as an optical component.

This is just one possible scheme to describe diffractive optical elements. In fact, during the last three decades diffractive optics have been given numerous names, by academics, engineers or marketing managers.

Another possible classification is one that based on the design techniques and the physical implementations used to produce them. In that way we can introduce five different groups of diffractive optics, partially coinciding with the previous classification, that have been reported in literature since 1967 [15], reported in Fig. 2.4.

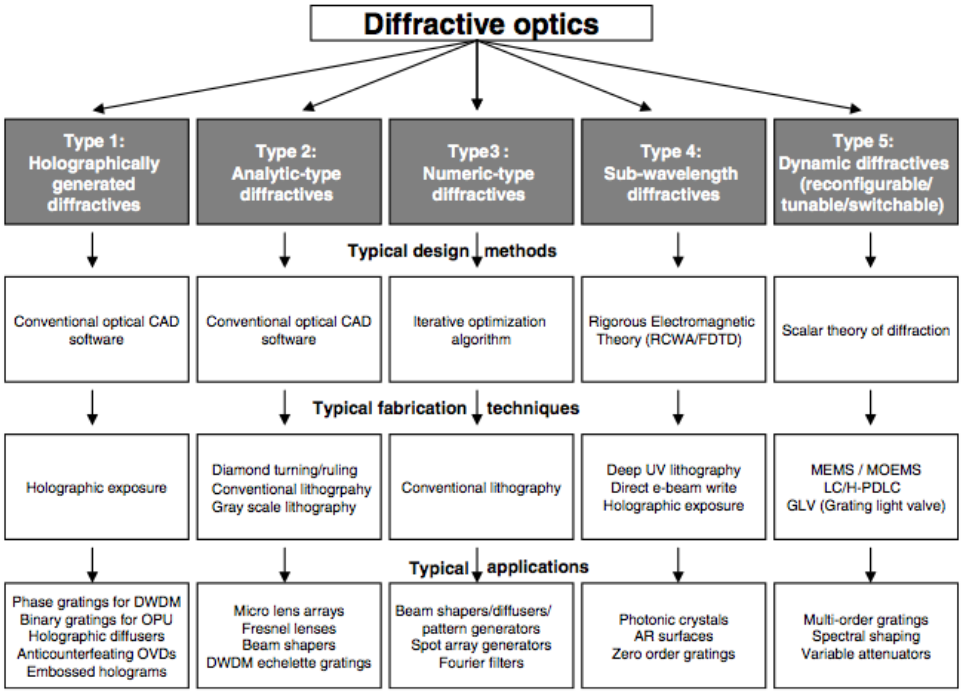

Figure 2.4: The five different diffractive elements types [16].

- **Holographic optical elements:** Refer to traditional optical holographic recording of volume phase holograms (in phase modulation materials) or surface relief holograms (in photo resist materials).

- **Analytic type diffractives:** Refer mostly to elements that can be designed or optimized by means of analytical methods, such as ray tracing or by solving an analytical equation (as is done for Fresnel lenses or gratings). These are the most common diffractives.

- **Numeric type diffractives:** Refer mostly to elements that cannot be designed or optimized by analytical methods and require stochastic iterative optimization procedures and algorithms. These elements can implement more complex optical functions than analytic-type diffractives, but have their limitations

- **Subwavelength diffractive elements:** Refer to elements which basic structures are smaller than the reconstruction wavelength and are thus highly polarization sensitive and act very differently from the previous two diffractive types.

- **Dynamic diffractives** Refer to all the technologies used to implement reconfigurable, tunable, or switchable diffractive optical functionalities. These elements can incorporate any of the four previous diffractive types

As DOEs are based on diffraction, they are highly dispersive: their properties depend on wavelength. Hence they are more commonly used with monochromatic light. However, the dispersive properties can also be used to advantage. For example, light at one wavelength can be focused at one point, and light at another wavelength can be focused at another point in space. DOEs have some advantages that we can resume as follows:

- A diffractive optics can perform more than one function. For example, it can multiple focal points, corresponding to multiple lenses on a single element. It can also be designed for use at multiple wavelengths;

- DOEs are generally much lighter and occupy less volume than refractive and reflective optical elements;

- One surface of a conventional glass lens is curved, whereas for a diffractive lens there is no such requirement. A diffractive element can be fabricated on any arbitrary shape of the substrate;

- The fabrication and replication of DOEs are relatively easy and cheap.

In addition, refractive and diffractive optical elements can be combined in order to extend existing optical functionality, or introduce additional functionality. For example, the hybrid lens consists of a conventional refractive lens with a diffractive structure etched into one of its surfaces; the diffractive surface corrects image aberrations and color aberrations.

2.3 A brief survey of Diffractive Optics

Diffraction gratings

Linear diffraction gratings have historically been the first type of diffractive element that has been studied, fabricated and used successfully in industrial applications. Some major application areas for diffraction gratings are spectroscopy, spectroscopic imaging, optical communications, and networking. They can be fabricated with a wide variety of techniques and technologies, from diamond ruling to holographic exposure and microlithography.

A diffraction grating is an optical device that periodically modulates the amplitude or the phase of an incident wave. Both the amplitude and the phase may also be modulated. In the simplest case, a grating can be considered as a large number of parallel, closely spaced slits. Regardless of the number of slits, the peak intensity occurs at diffraction angles governed by the following grating equation:

$$d \sin \alpha'_m = m\lambda \tag{2.3.1}$$

where d is the spacing between the slits, m is the *diffraction order*, and α'_m is the diffraction angle (see Fig. 2.5).

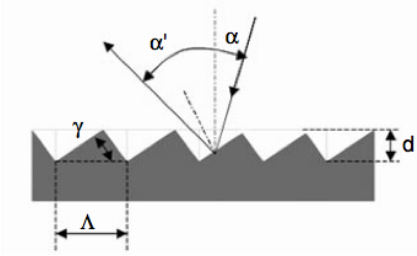

Figure 2.5: Section of a diffraction grating [17].

Linear diffraction gratings are designed according to the formula (2.3.1), and thus are analytic-type elements. Diffraction gratings are very effective to separate a wave into different wavelengths with high resolution (see Fig. 2.6).

The spectral dispersion of such a grating can be written as:

$$\frac{\partial \alpha'_m}{\partial \lambda} = \frac{m}{\Lambda \cos(\alpha'_m)} \tag{2.3.2}$$

where Λ is the period of the grating, α the incident angle. The resolution is:

$$R = mN_0 \tag{2.3.3}$$

where N_0 is the total number of grating grooves.

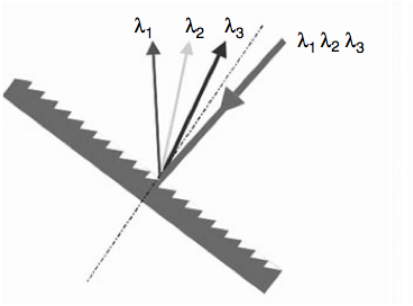

Figure 2.6: Diffraction grating as dispersor [17].

Fresnel zone plate

Fresnel zone plate (FZP) is a classical DOE, that consists of opaque and transparent circular zones (see Fig. 2.7).

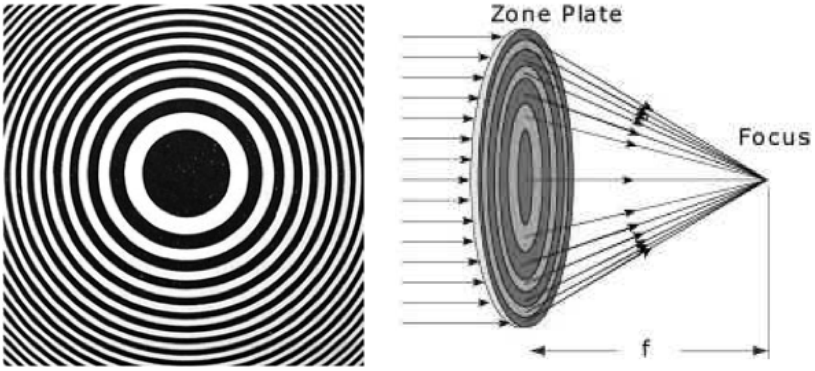

Figure 2.7: Fresnel zone plate.

Such a DOE serves as a flat lens, can be mass-manufactured and is commonly used in many technologies such as overhead projectors.

FZP is an analytic type element. The analytic equation is given by the path difference between two rays traveling along SOP and SAP (see Fig. 2.8).

$$\Delta(r) = (\rho_0 + \rho) - (z_0 - z) = \sqrt{r^2 + z_0^2} + \sqrt{r^2 + z^2} - (z_0 + z) \tag{2.3.4}$$

The Fresnel-zone parameter, n, is defined such that the path difference is an integer multiple of half wavelengths:

$$n\frac{\lambda}{2} = \Delta(r) \tag{2.3.5}$$

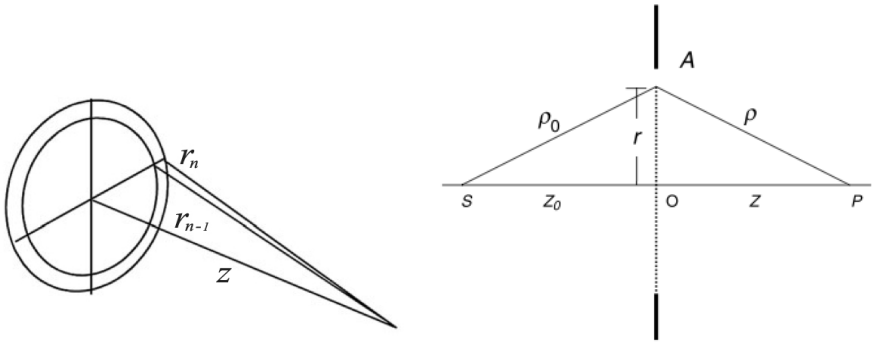

Figure 2.8: Fresnel zone plate: side view.

The nth Fresnel zone is the area between the circles with radii r_{n-1} and r_n. The field at P emanating from a point on the circle with radius r_n is half a wavelength out of phase with the field from a point on the circle with radius $r_{n\pm1}$. So the adjacent zones cancel each othereq. by destructive interference. As a consequence the total field at P will increase if either all even or all odd zones are blocked out; the remaining zones reinforce each other, thus creating a focal point at distance z. Assuming the zone plate is illuminated by a plane wave, $z_0 \approx \infty$, and setting $z = f_0$, eq.(2.3.4) becomes

$$\frac{r_n}{\lambda} = \sqrt{\frac{f_0}{\lambda}\left(n - \frac{1}{2}\right) + \frac{(2n-1)^2}{16}} \tag{2.3.6}$$

The quantity f_0 is called the focal point. Fresnel zone plate operates as a lens with focal length f_0. The equation of a FZP is:

$$r_n^2 = \left(f_0 + \frac{n\lambda}{2}\right)^2 - f_0^2 \tag{2.3.7}$$

where r_n is the radius of th n-th circle. Substituting eq.(2.3.6), the eq.(2.3.7) becomes

$$r_n^2 = f_0^2\left[\frac{n\lambda}{f_0} + \frac{1}{4}\left(\frac{n\lambda}{f_0}\right)^2\right] \tag{2.3.8}$$

When n is large, this can be approximated as

$$r_n \approx \sqrt{n\lambda f_0} \tag{2.3.9}$$

The phase profile of a diffractive element can take many forms depending on the optical software used to design and optimize it. Once the aspheric phase profile is defined in this infinitely thin surface, the phase profile is sliced into 2π phase shift slices for the considered wavelength for maximum diffraction efficiency in the fundamental positive order, a process shown in Fig. 2.9.

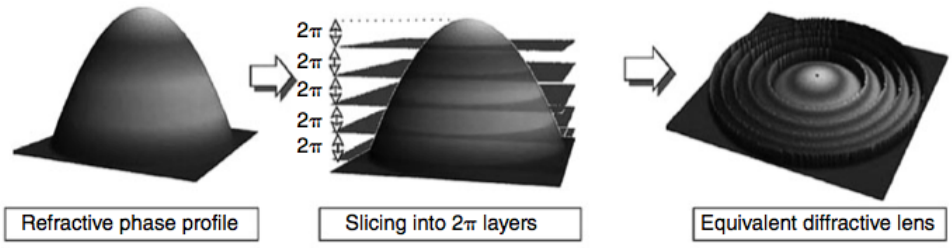

Figure 2.9: From the initial aspherical phase profile to the DOE fringes [17].

Computer Generated Holograms

Computer Generated Holograms (CGHs) are numeric type elements (see Fig. 2.4), which are often used as single standing optical elements.

An hologram represents the synthetic image of an object. This is produced by using particular plates in which the information on the EM field of the objects that one wants to reproduce is recorded. Essentially, a holographic plate records the interference pattern obtained from the superposition of the EM field diffused by the object and a coherent reference beam. For this reason, when the plate is illuminated by a beam having the same characteristics of the reference beam, an image of the object will appear (see Fig. 2.10).

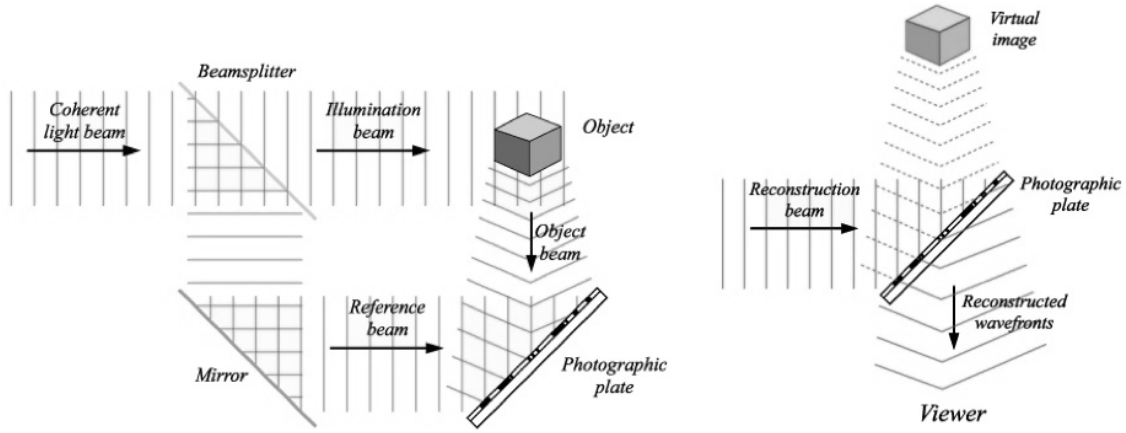

Figure 2.10: Left: production scheme of an hologram. Right: Reconstruction of 3D image.

Holography was invented in 1948 by Gabor [18]. At that time the production of holographic plates was limited by the absence of coherent sources that are strongly required to obtain stable interferograms. A great improvement of the holographic techniques was made possible only after the development of laser sources in the Sixties.

Until now, two distinct types of transmission holographic plates have been developed: the on-

axis Gabor holograms [18] and the off-axis Leith-Upatnieks holograms [19]. A Gabor hologram produces both virtual and real images of the object along the same axis. Thus, an observer will always see a superposition of the two images. Instead, with the Leith-Upatnieks holograms it is possible to separate the two images, since the holographic plate is produced by imposing an offset angle between the reference wave and the light scattered by the object.

In the mid Sixties the synthesis of holographic plates was improved with the aid of computers [20]. In fact, computers allow to easily calculate the complex amplitude of the EM field propagated from the object to the hologram plane, which is then encoded as a real non-negative function.

Computer generated holograms offer important advantages over the optical holograms since there is no need for a real object: the objects, which one wants to show, do not have to possess any physical reality at all. It is a completely synthetic hologram generation.

There are two types of CGHs, the Fourier type and the Fresnel type. The first one projects the desired pattern in the far field whereas the second one reconstructs the pattern in the near field, and thus can be considered as a complex diffractive lens. Fig. 2.11 represents a Fourier and a Fresnel CGHs which split the incoming beam into an array of 3×3 beams. Fourier type element creates nine collimated beams from a single collimated beam, whereas the second one creates nine converging beams from the same collimated beam. In other words the Fresnel-type CGH could be considered as a multifocus diffractive lens.

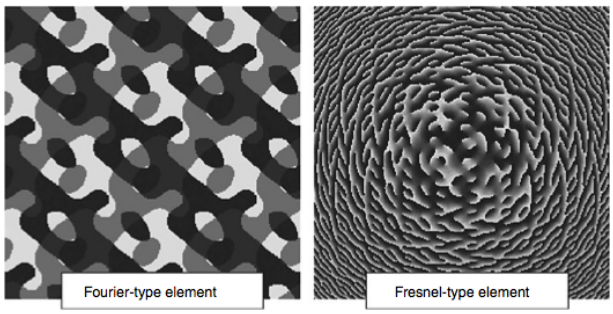

Figure 2.11: Two types of CGHs: Fourier type on the left and Fresnel-type on the right [17].

There are several steps in the creation of a CGH. These are sampling of waves, computation of wave propagation, coding of complex wave information on the hologram and recording of the resulting CGH. Many different iterative optimization algorithms have been successfully developed and applied in literature to the CGH design process. The most commonly used algorithm in industry to design both Fresnel or Fourier CGHs is an iterative Fourier transform algorithm.

Fourier transformation: Lohmann method

The Fourier transformation concept was first introduced by Brown and Lohmann [15]. It utilizes the Fourier transformation property of a lens and generate a CGH design for a Fourier transform

hologram. It is assumed that the reconstructed image is on an output plane, as shown in Fig. 2.12.

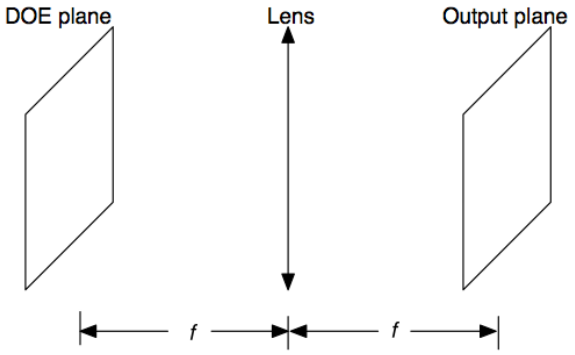

Figure 2.12: The Fourier transform system used in CGH design.

In the Lohmann method the hologram plane is divided into smaller rectangles, each containing an aperture. Amplitude modulation is achieved by controlling the sizes of the apertures, and phase modulation is achieved by controlling their positions. This results in a binary transmission pattern.

We define $H(v_x, v_y)$ as the binary transmission function of the hologram and $h(x, y)$ the output amplitude from hologram, that is proportional to the desired image $f(x', y')$. When a tilted plane wave, $\exp(2\pi i x_0 v_x)$ is incident on the binary hologram, the complex amplitude after the hologram is $H(v_x, v_y)\exp(2\pi i x_0 v_x)$. The complex amplitude at the image plane is its Fourier transform (see Fig. 2.13).

This is always valid, and in theory it is referred to an infinite number of aperture sizes and positions. But it is not practical for many methods of implementations. To overcome this obstacle, a discrete method can be used to quantize the size and position of the apertures in each cell. In the modified method, the size of each aperture still controls amplitude, and phase is controlled by shifting the aperture position. However, the possible values of amplitude and phase are now quantized. In the quantized Lohmann method, each hologram cell is divided into an $N \times N$ array. This will be referred to as N-level quantization. This restricts the possible center positions and heights of each aperture. Thus, the phase and amplitude at each cell is quantized. Specifically, there are N possible positions for the center of the aperture (phase), and $N/2+1$ potential height values (amplitudes) including zero amplitude, since the cell is symmetric in the y direction. A large N produces a pattern close to that of the exact hologram. Quantizing aperture positions is useful in practical implementations. For example, spatial light modulators (SLMs) can be used in real time to control amplitude and phase modulation at each hologram point. Unfortunately, the SLM cannot accurately generate an exact Lohmann cell, and quantization is necessary to make realization practical.

In Fig. 2.13 we show an example of computer reconstruction from an hologram.

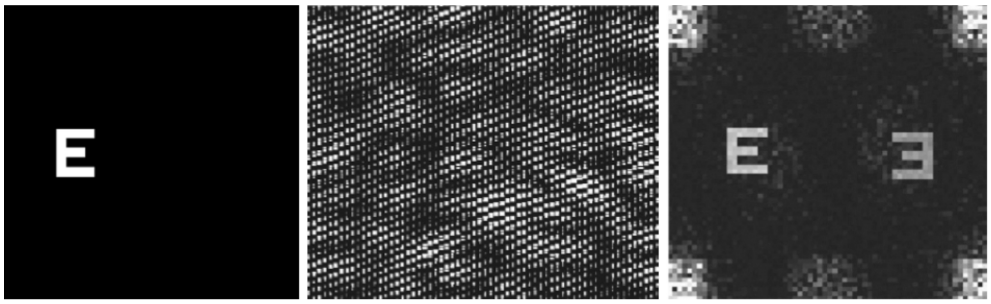

Figure 2.13: On the left there is the image used in the generation of the Lohmann hologram which is visible in the central panel. This hologram was generated with 16 levels of quantization. The computer reconstruction from its Lohmann hologram is shown in the right panel. The twin images are the real and virtual images [21].

Chapter 3

Optical vortices

3.1 Optical dislocations

In 1974, John Nye and Michael Berry broke with the conventional view of waves and their propagation and introduced the concepts of wavefront dislocations. This seminal paper marks the birth of a new branch of physics called *singular optics*. In a recent paper Berry gave a definition of singularities [22] as:

"Singularities are places where mathematical quantities become infinite, or change abruptly. In waves - of light, for example - there can be singularities in the intensity, in the phase, or in the polarization. This is a modern view, sharply different from the traditional approach where waves were simply the solutions of wave equations, and singularities - if considered at all - were regarded as awkward places where the usual treatments fail".

There exist three types of dislocations:

1. screw dislocations;

2. edge dislocations;

3. mixed screw-edge dislocations.

The first takes the name from the screw topology of the wavefronts. The second are characterized by the topology of two half-planes that are joined discontinuously, resulting in an infinitely long dislocation line or edge. Similar to dislocations in crystals, an edge dislocation can also end in a screw dislocation, resulting in the so-called mixed screw-edge dislocation, the latter type.

3.2 New electromagnetic degree of freedom

We can describe the EM field of generic beam with wavefront dislocations as

$$\psi(\vec{r},t) = A(\vec{r},t)\exp[i\Phi(\vec{r},t)] \tag{3.2.1}$$

where $\Phi(\vec{r},t)$ is the phase term. The amplitude $A(\vec{r},t)$ has to be zero in correspondence of the position of a wavefront dislocation, where the phase is not defined [23].

Coullet *et al.* [2] have introduced optical vortices (OVs) as new term to indicate screw dislocations. OVs are topological defects due to phase singularities in light beams, related to the helicoidal shape of the wavefront.

The propagation of OVs in paraxial approximation[1] is described with good approximation by the scalar wave equation

$$\nabla^2 E - \frac{1}{c^2}\frac{\partial^2 E}{\partial t^2} = 0 \tag{3.2.2}$$

The complex solution can be written in cylindrical coordinates [24]:

$$E = (r,\varphi,z,t) \propto \begin{cases} r^{|\ell|}\exp[i(kz-\omega+\ell\varphi)] \\ r^{-|\ell|}\exp[i(kz-\omega+\ell\varphi)] \end{cases} \tag{3.2.3}$$

In both solutions the phase depends on azimuthal angle φ and on the integer number ℓ called *topological charge*. Before explaining the physical meaning of the topological charge, we notice that these solutions cannot describe any real wave because the first equation diverges for $r \to \infty$, whereas the second one tens to infinity for $r \to 0$. The problem is the amplitude growth, that can be avoid by introducing an additional amplitude term so that the amplitude ($A(\vec{r},z)$) results zero at the center ($r = 0$) and decreases in periphery ($\propto 1/r$).

The topological charge is defined by the path integral

$$\ell = \frac{1}{2\pi}\oint \nabla\Phi \cdot d\vec{r} \tag{3.2.4}$$

taken along a closed circuit $\vec{r}$ around the vortex and which involves the phase gradient $\nabla\Phi$. It indicates the number of 2π phase changes along any closed circuit around the dislocation center.

The helicoidal wavefront, when $\ell \neq 0$, is defined by the equation

$$\ell\varphi - kz = \text{const} \tag{3.2.5}$$

whereas, if $\ell = 0$, it describes a planar surface. The topological charge attributed to this wavefront structure is positive for a right-screw helicoid. When $|\ell| > 1$, the wavefront is composed by $|m|$ identical helicoids nested on the z axis and separated by the wavelength λ.

The value of the topological charge indicates also the number of the lobes of the helicoidal wavefront, as shown in Fig. 3.1.

[1] Paraxial approximation is valid when the propagation vector $\vec{k}$ forms a small angle with the propagation axis.

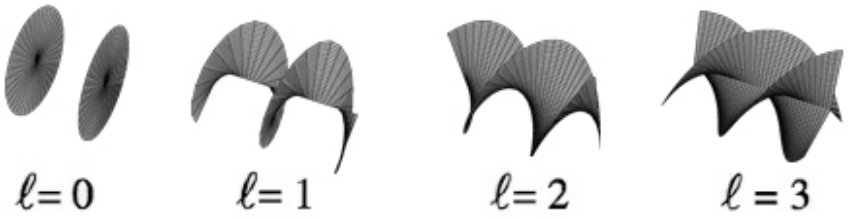

Figure 3.1: Wavefronts of light beams containing OVs with $\ell = 0, 1, 2, 3$. Source: `http://www.physics.gla.ac.uk/Optics/play/photonOAM/`.

3.3 Orbital angular momentum

That electromagnetic (EM) fields can carry not only energy and linear momentum but also angular momentum over very large distances has been known for over a century. However, it is less than twenty years ago that optical methods for the manipulation of light in well-defined EM orbital angular momentum (OAM) eigenstates were developed [8]. In classical electrodynamics terms, the electromagnetic field (E, B) in a volume V of free space, where the dielectric permittivity is ε_0, carries the total linear momentum

$$\vec{p} = \varepsilon_0 \int_V dx^3 (\vec{E} \times \vec{B}) \tag{3.3.1}$$

associated with translational dynamics and force action, and the total angular momentum

$$\vec{J} = \varepsilon_0 \int_V dx^3 (\vec{x} - \vec{x_0}) \times (\vec{E} \times \vec{B}) \tag{3.3.2}$$

associated with rotational dynamics and torque action about the moment point $\vec{x_0}$. To leading order in distance from the source

$$r = |\vec{x} - \vec{x_0}| \tag{3.3.3}$$

the conserved physical observables $\vec{p}$ and $\vec{J}$ are independent of r. It is worth noticing that the linear momentum $\vec{p}$ from a radiation source may tend to zero at infinity, while the angular momentum $\vec{J}$ from the same source may tend to a non-zero constant there. This is typically the case of an OAM structured electromagnetic beam whose field intensity falls off sufficiently rapidly with distance from the beam axis.

The total angular momentum density $\vec{\mathcal{J}}$ is given by

$$\vec{\mathcal{J}} = \vec{r} \times \vec{\mathcal{P}} \tag{3.3.4}$$

where $\vec{r}$ is the vector from the chosen origin around which the total angular momentum density is measured to the point under consideration, $\vec{\mathcal{P}}$ is the linear momentum density at that point. This angular momentum density can be separated into two parts when integrated over the volume of the system,

$$\vec{J} = \int \vec{\mathcal{J}} d^3r = \vec{L} + \vec{S} \tag{3.3.5}$$

The vector $\vec{L}$ is the orbital angular momentum, intimately related to beam vorticity and phase singularities, spans a state space of a denumerably infinite dimension and $\vec{S}$ is the spin angular momentum, associated with the two states of wave polarisation. Spin and orbital angular momenta of a light beam can be divided only for the component of the total angular momentum parallel (or at least paraxial) to the propagation axis [25].

OAM was already theoretically predicted at the quantum level by Poynting and later also by Majorana in his unpublished notes about the formulation of quantum electrodynamics [26]. Heitler, in 1936 [27] wrote a classical formulation of the OAM by using multipolar expansions. Allen *et al.* [1] in 1992 showed that light beams with phase singularities can carry orbital angular momentum (OAM). This is a property of the electromagnetic field, related to the helicoidal shape of the wavefront.

The amplitude of this electromagnetic field is usually described in terms of superpositon of Laguerre-Gauss (LG) modes, a particular class of cylindrically symmetric laser cavity modes. LG modes are characterized by two indices: l, the azimuthal index indicating the number of twists of the helical wavefront within a wavelength, and which coincides with the topological charge ℓ, and p the number of radial nodes present in the LG mode (see Fig. 3.2).

In cylindrical coordinates, in the plane orthogonal to the beam propagation direction, z, the Electromagnetic field is given by

$$u_{pl}(r,\varphi,z) = \sqrt{\frac{2p!}{\pi(p+|l|)!}}\frac{1}{w}\left(\frac{r\sqrt{2}}{w}\right)^{|l|} L_p^{|l|}\left(\frac{2r^2}{w^2}\right) \times \\ \times \exp\left(\frac{-r^2}{w^2}\right)\exp\left(\frac{-ikr^2}{2R}\right)\exp[-i(2p+|l|+1)\psi]e^{-il\varphi} \tag{3.3.6}$$

where w is the beam width (the radius at which the amplitude decreases by a factor e^{-1}), z_R is the Rayleigh range, R is the curvature radius, $\varphi(z) = arctan(z/z_0)$ is the Gouy phase and L_p^l is the generalized Laguerre polynomial. The phase varies linearly with the azimuthal angle, φ, as expressed by the term $\exp(-i\ell\varphi)$.

The physical form of a beam carrying orbital angular momentum is shown in Figure 3.3.

A three dimensional plot of the azimuthal phase variation of the beam shows a linearly increasing phase change about the azimuthal direction. The phase variation along a closed path

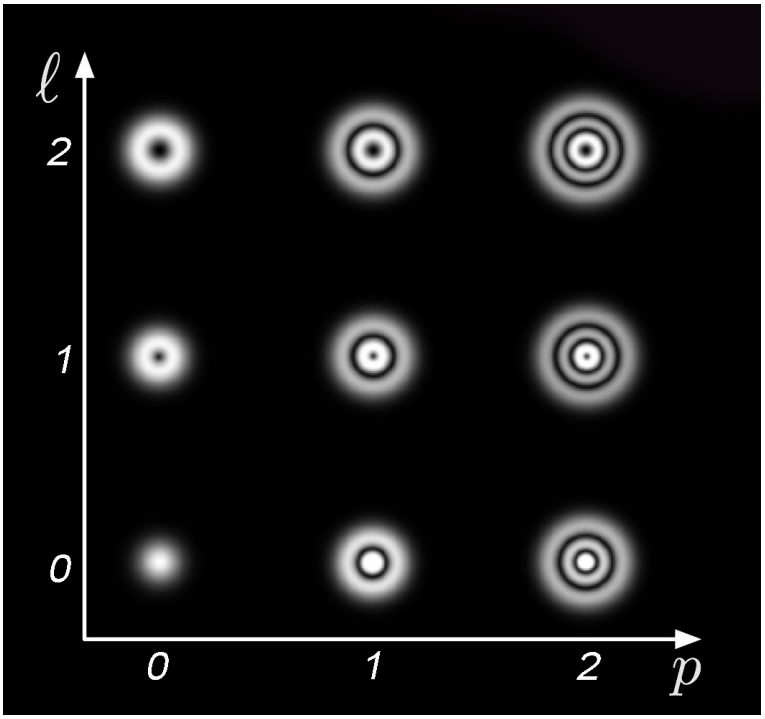

Figure 3.2: Various intensity distributions of LG modes. For each increment of p, an additional concentric ring is added to the mode profile while an increment of l results in an increase in the diameter of the dark core located on the beam axis.

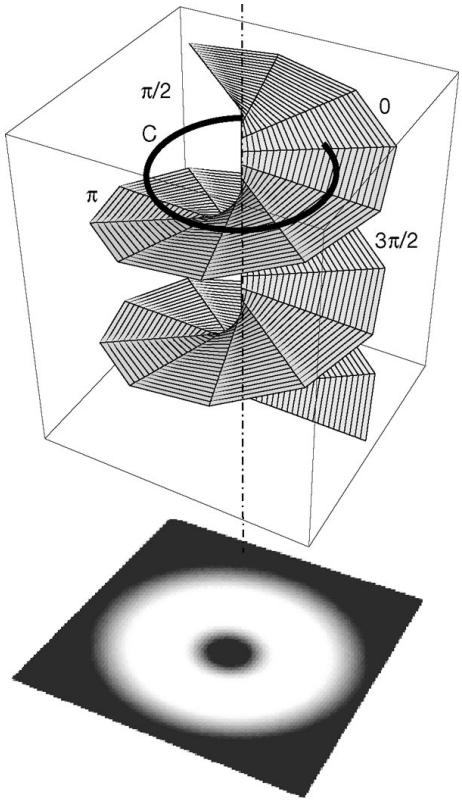

Figure 3.3: Wavefront of the Laguerre - Gausse mode LG_0^1 and, at the bottom, the intensity distribution, i.e. linear momentum. Source: Mair et al. *Entanglement of the orbital angular momentum states of photons*, Nature (2001).

C around the optical axis is 2π. The intensity distribution shows a distinctive doughnut pattern that is directly due to the azimuthal phase variation and the consequent destructive interference along the beam centre. The associated Poynting vector precesses around the optical axis, with constant inclination with respect to the propagation axis [28, 29].

Returning to the eq.(3.2.1) we can define the amplitude $A(\vec{r},t)$ of the EM field of a generic vortex beam as

$$\vec{A}\,(\vec{r},t) = \vec{\sigma}u(\vec{r})e^{i(kz-\omega t)} \tag{3.3.7}$$

where $\vec{\sigma}$ is a complex vector that describes the polarization of the field, ω is the frequency and $u(\vec{r})$ describes the field amplitude distribution in the paraxial approximation [1]

$$u(r,\varphi) = u(r)e^{i\ell\varphi} \tag{3.3.8}$$

For this kind of beam, the linear momentum density, $\vec{\mathcal{P}}$, in cylindrical coordinates with unit vectors $\hat{r}$, $\hat{\varphi}$, and $\hat{z}$ is [30]

$$\mathcal{P} = \frac{\varepsilon_0}{2}(\vec{E}^* \times \vec{B} + \vec{E} \times \vec{B}^*) = i\omega\frac{\varepsilon_0}{2}(u^*\nabla u - u\nabla u^*) + \omega k\varepsilon_0|u|^2\hat{z} + \omega\sigma_z\frac{\varepsilon_0}{2}\frac{\partial|u|^2}{\partial r}\hat{\varphi} \tag{3.3.9}$$

The first two terms are independent of polarization and refer to the orbital angular momentum, while the third term recognizes the spin angular momentum, related to polarization. The term $u^*\nabla u - u\nabla u^*$ has reference to the quantum-mechanical expression of the expectation value of the linear momentum of a wave function. From this equation it is evident that only beams that contain at least one discontinuity ($\nabla u \neq 0$) can carry OAM.

For a circularly polarized beam propagating in the z-direction the r, φ and z components of linear momentum density are given by [28]

$$\mathcal{P}_r = \varepsilon_0\frac{\omega kr}{R(z)}|u|^2 \tag{3.3.10}$$

$$\mathcal{P}_\varphi = \varepsilon_0\left[\frac{\omega\ell}{r}|u|^2 - \frac{1}{2}\omega\sigma\frac{\partial|u|^2}{\partial r}\right] \tag{3.3.11}$$

$$\mathcal{P}_z = \varepsilon_0\omega k|u|^2 \tag{3.3.12}$$

The first component refers to the enlargement of the beam during its propagation; the azimuthal component $\mathcal{P}_\varphi$ has two terms: the first depends on the topological charge ℓ, therefore on OAM, whereas the second term depends on spin (σ). The last component, $\mathcal{P}_z$, is the linear momentum along the propagation axis. Using eq.(3.3.5), it is simple to obtain the z component of the total angular momentum density:

$$\mathcal{J}_z = \varepsilon_0\left(\omega\ell|u|^2 + \frac{1}{2}\omega\sigma r\frac{\partial|u|^2}{\partial r}\right) \tag{3.3.13}$$

Integrating the previous equation over the cross-section of the beam we obtain the z component of the total angular momentum; dividing by the total energy W we have the total angular momentum per unit of energy. The two components of J_z are evident: the first one depends on OAM (ℓ) and the second one on the spin (σ). We can conclude that any photon of a vortex beam with an energy $W = \hbar\omega$ carries a quantity of $\ell\hbar$ of OAM.

$$\frac{J_z}{W} = \frac{\ell}{\omega} + \frac{\sigma}{\omega} \tag{3.3.14}$$

The same result is obtained in the next section, describing the problem from a quantistic point of view.

3.3.1 Orbital angular momentum in quantum regime

The wavefunction in Dirac notation is $|\psi\rangle$. In a paraxial mode, say an LG mode, we can write the wave function as

$$|\psi\rangle = |\ell\rangle = u(r)e^{i\ell\varphi} \tag{3.3.15}$$

where $e^{i\ell\varphi}$ is a phase term. The stationary solution $\psi(\vec{r})$ satisfies three eigenvalue equations of three different quantum operators. The equations relate the Hamiltonian $\hat{H}$, i.e. the operator associated to the total energy of the system, the momentum operator $\hat{P}$ and the projection along the z axis of total angular momentum $\hat{J}_z$.

$$\hat{H}\Psi = \hbar\omega\Psi \qquad \text{con} \qquad \hat{H} = c\left(\vec{s}\cdot\frac{\hbar}{i}\nabla\right) \tag{3.3.16}$$

$$\hat{P}\Psi = \hbar k\Psi \qquad \text{con} \qquad \hat{P} = \frac{\hbar}{i}\nabla \tag{3.3.17}$$

$$\hat{J}_z\Psi = \hbar j\Psi \qquad \text{con} \qquad \hat{J} = \vec{r}\times\frac{\hbar}{i}\nabla + \hbar\vec{s} \tag{3.3.18}$$

$\vec{s}$ is the spin vector. $\vec{s} = (s_x, s_y, s_z)$, with:

$$s_x = \begin{pmatrix} 0 & 0 & 0 \\ 0 & 0 & -i \\ 0 & i & 0 \end{pmatrix} \quad s_y = \begin{pmatrix} 0 & 0 & i \\ 0 & 0 & 0 \\ -i & 0 & 0 \end{pmatrix} \quad s_z = \begin{pmatrix} 0 & -i & 0 \\ i & 0 & 0 \\ 0 & 0 & 0 \end{pmatrix} \tag{3.3.19}$$

The equation (3.3.18) shows that each photon carries both spin and orbital angular momentum. The first term of the expression of $\hat{J}$ is the z component of the orbital angular momentum operator $\hat{L}$. The Cartesian components of $\hat{L}$ are [31]

$$\hat{L}_y = -i\hbar\left(y\frac{\partial}{\partial z} - z\frac{\partial}{\partial y}\right) \tag{3.3.20a}$$

$$\hat{L}_y = -i\hbar\left(z\frac{\partial}{\partial x} - x\frac{\partial}{\partial z}\right) \tag{3.3.20b}$$

$$\hat{L}_x = -i\hbar\left(x\frac{\partial}{\partial y} - y\frac{\partial}{\partial x}\right) \tag{3.3.20c}$$

In cylindrical coordinates (r, φ, z) they are

$$\hat{L}_x = -i\hbar\left[\sin\varphi\left(z\frac{\partial}{\partial r} - r\frac{\partial}{\partial z}\right) + \frac{z}{r}\cos\varphi\frac{\partial}{\partial\varphi}\right] \tag{3.3.21a}$$

$$\hat{L}_y = -i\hbar\left[\cos\varphi\left(z\frac{\partial}{\partial r} - r\frac{\partial}{\partial z}\right) + \frac{z}{r}\sin\varphi\frac{\partial}{\partial\varphi}\right] \tag{3.3.21b}$$

$$\hat{L}_z = -i\hbar\frac{\partial}{\partial\varphi} \tag{3.3.21c}$$

and in spherical coordinates (r, φ, θ) they are

$$\hat{L}_x = -i\hbar\left(\sin\varphi\frac{\partial}{\partial\theta} + \cos\varphi\cot\theta\frac{\partial}{\partial\varphi}\right) \tag{3.3.22a}$$

$$\hat{L}_y = -i\hbar\left(\cos\varphi\frac{\partial}{\partial\theta} + \sin\varphi\cot\theta\frac{\partial}{\partial\varphi}\right) \tag{3.3.22b}$$

$$\hat{L}_z = -i\hbar\frac{\partial}{\partial\varphi} \tag{3.3.22c}$$

For an electric field $\vec{E}$ that depends on the azimuthal angle φ in such a way that

$$\vec{E} = \vec{E}_0(t, \vec{x})\Phi(\varphi) \tag{3.3.23}$$

we find that

$$\hat{L}_z\vec{E}(t, \vec{x}) = -i\hbar\left(\frac{\partial\vec{E}_0(t, \vec{x})}{\partial\varphi}\Phi(\varphi) - \vec{E}_0(t, \vec{x})\frac{\partial\Phi(\varphi)}{\partial\varphi}\right) \tag{3.3.24}$$

If $\vec{E}_0$ is rotationally symmetric around the z axis, so that $\vec{E}_0 = \vec{E}_0(t, r, z)$ in cylindrical coordinates, $\vec{E}_0 = \vec{E}_0(t, r, \theta)$ in spherical coordinates *etc.*, and if the azimuthal part is expressed n a Fourier series

$$\Phi(\varphi) = \sum_{\ell=-\infty}^{\infty} c_\ell e^{i\ell\varphi} \tag{3.3.25}$$

we see that

$$\hat{L}_z\vec{E}(t, \vec{x}) = \sum_{\ell=-\infty}^{\infty} c_\ell\ell\hbar\vec{E}_0 e^{i\ell\varphi} = \sum_{\ell=-\infty}^{\infty} c_\ell\ell\hbar\vec{E}_\ell \tag{3.3.26}$$

$\vec{E}$ is a weighted superposition of OAM eigenstates $\vec{E}_\ell = \vec{E}_0 e^{i\ell\varphi}$. In other words, equation (3.3.26) represents the OAM spectrum of the electromagnetic field $\vec{E}$. Furthermore,

$$\hat{L}_z\vec{E}_\ell = \ell\hbar\vec{E}_\ell \tag{3.3.27}$$

which means that the z component of the orbiatl angular momentum of each photon is $\ell\hbar$ [1].

The OAM of classical beams can be measured when absorbed by small particles [32]. Instead, the OAM of a single photon is difficult to measure, since it only contains an angular momentum of

order $\hbar$. Leach *et al.* [33] introduced a technique to overcome this problem based on a modified Mach-Zehnder interferometer. A single photon interferes with itself, so the technique depends on examining the local phase distribution of the mode in which the photon resides. The interferometer sends the even OAM states to one output port, while the odd OAM states appear at the second output port. By cascading such interferometers in combination with vortex-generating devices and single-photon detectors, it is possible to determine the OAM value of an incoming photon in an integer basis.

3.4 Intrinsic or extrinsic nature of OAM

It is well known that spin angular momentum is an intrinsic property[2] of the photons, but the question for orbital angular momentum was debated for a long time [34, 32].

The covariant formulation of the photon wave function has been shown to be formally equivalent to quantum electrodynamics [26]. This implies that OAM is not an intrinsic property of single photons. In fact, the rank of the spinor representation of the photon is 1, representing its lowest boson degree of its wavefunction in the momentum/space representation. If OAM were intrinsic, the rank of the spinor representation would be infinite, according to Majorana infinite component equation [26].

At the same time Berry demonstrated that the magnitude of the orbital angular momentum, in paraxial approximation, is unchanged when measured about any axis for which the transverse linear momentum of the beam vanishes [35]. OAM therefore can exhibit both intrinsic and extrinsic behaviour and has thus been described as 'quasi-intrinsic' [36].

3.5 Generation of Optical Vortices

There are some spontaneous processes that were before postulated and, then, demonstrated in beams propagating through irregular refracting media or reflected from rough surfaces [37]. OVs were recognized in the phase fronts of light beams propagating through nonlinear media like Kerr refractive media [38], but also in nonlinear optical system [39]. The appearance of screw wavefront dislocations has been demonstrated also in the simple case of three (or more) interfering plane waves [40]. These spontaneous mechanism produce OVs with random value of topological charge and usually appear at random locations.

In laboratory experiments is necessary to produce OVs with a certain value of topological charge and in predefined locations. For this reason, several methods to produce OVs in light beams have been developed.

[2] The intrinsic properties of a particle are those that do not depend on the choice of a reference frame. Those quantities are simply rest mass, electric charge and spin.

There are several techniques that can be use to generate this form of azimuthal phase delay in conventional optics [41]. It is possible to generate the LG modes directly from within the laser resonator cavity by tuning the cavity mirrors [42].

Another method consist in the astigmatic conversion of an HG_{mn} Hermite-Gaussian laser cavity mode into an ℓ-charged LG_p^l vortex mode [43]. The mode conversion is achieved by using two cylindrical lenses placed consecutively along the propagation axis z of the HG_{mn} mode. The first cylindrical lens converts a HG_{mn} to a LG_p^l mode, producing a $\pi/2$ difference between the phases of the two modes. The second lens (a π converter) exchanges the indices of the incoming mode, converting an LG_p^l mode into one with opposite azimuthal dependence. Analogously it is possible to produce LG modes with the first cylindrical lens that focuses the light along a transverse axis. In the focal plane, the beam undergoes a rotation by 45° around the z axis. This is equivalent to have a superposition of the original HG_{mn} mode with a HG_{nm} mode. The position of the second lens can then be chosen in order to produce a $\pi/2$ difference between the phases of the two modes. The final result is an LG_p^l mode, with $l = |m - n|$ and $p = \min(m, n)$.

It is more convenient to generate LG beam modes directly from a fundamental Gaussian mode rather than a higher order HG mode due to accessibility of single mode Gaussian beam lasers. Here, I will describe two common optical elements use to generate LG beams directly from Gaussian beam, namely computer the generated hologram and the spiral phase plate.

3.5.1 Computer-generated fork hologram

We have introduced computer generated hologram in the previous chapter (Sect. 2.3) as numeric type elements. An hologram represents the synthetic image of an object. The most important property of computer-generated holograms is the possibility of reproducing optical fields from objects that do not physically exist, like light beams. For this reason, computer-generated holograms have been used to produce and study light beams containing screw wavefront dislocations [9, 44, 45].

The CGH used to produce OVs is a diffraction grating with a fork dislocation. For this reason it is called *fork hologram* (see Fig. 3.4). The beam crosses the discontinuity of the hologram, so that it acquires a certain value of orbital angular momentum. The value of ℓ depends on the number of dislocations in the fork of the hologram.

When a monochromatic beam with a wavelength λ intersects perpendicularly a FH, the grating structure ideally produces an infinite number of diffraction orders. The direction of an order m subtends an angle α_m with the propagation axis of the input beam. α_m is given by the grating equation [12]

$$\Lambda \sin \alpha_m = m\lambda \tag{3.5.1}$$

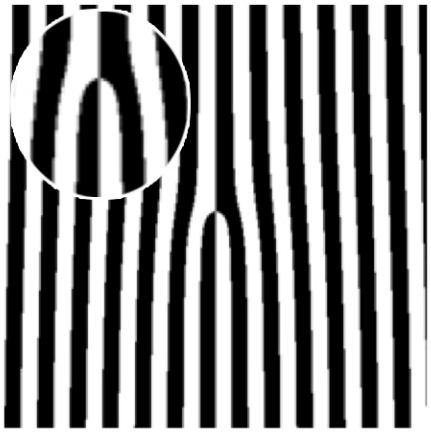

Figure 3.4: Interferogram of a single point vortex of charge ℓ = 1. The vortex core is located at the fork of the grating lines.

where Λ is the grating period, i.e. the spatial separation of the lines far from the center (see Fig. 3.5).

The pattern of the fork hologram is designed following the approach of Bazhenov [9]. It is the interferogram of two waves, a planar reference wave and the "object" wave that contains the holografic image.

In our case the object wave is

$$u_{obj} = C_{obj} \exp(i\ell\varphi) \tag{3.5.2}$$

where C_{obj} is the amplitude and φ the azimuthal angle in the (x, y) plane. The reference beam is a plane wave of amplitude C_{ref}, whose wavevector lies in (x, z) plane, forming an angle β with the optical axis z:

$$u_{ref} = C_{ref} \exp(-\frac{i2\pi x}{\Lambda}) \tag{3.5.3}$$

with $\Lambda = \lambda / \sin\beta$. The intensity of the interfering waves produce the desired interferogram:

$$I(x, \varphi) = |u_{obj} + u_{ref}|^2 = 2C^2 \left[1 + \cos\left(\frac{2\pi x}{\Lambda} + \ell\varphi\right)\right] \tag{3.5.4}$$

having set $C_{obj} = C_{ref} = C$ to achieve unity contrast ($(I_{max} - I_{min})(I_{max} = 1)$.

An alternative expression useful for computational purposes is the transmission function written as power spectrum of the Fourier series [46]

$$T(x, \varphi) = \sum_{-\infty}^{\infty} C_m \exp(im\ell\varphi) \exp\left(\frac{i2\pi mx}{\Lambda}\right) \tag{3.5.5}$$

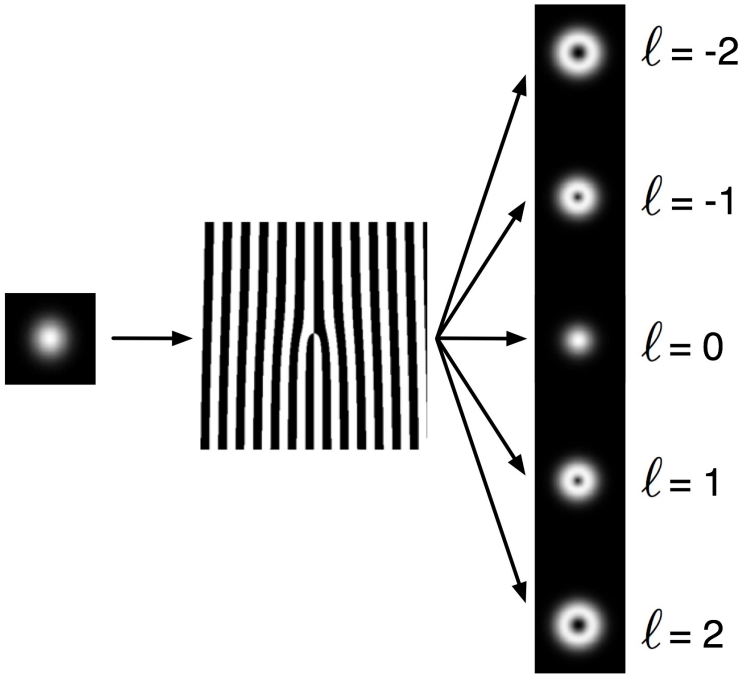

Figure 3.5: A fork hologram crossed by a light beam ideally produces an infinite number of diffraction orders.

A binary hologram (so called because each pixel can only assume one of two values, zero for black and one white) is poorly efficient: most of the crossing wavefront does not assume phase singularities. One can build the hologram so as to maximize the efficiency of diffraction in a particular order of diffraction. In other words the fork hologram can be blazed and the transmission function is expressed by:

$$T(r,\varphi) = \exp\left[i\delta \frac{1}{2\pi} \text{mod}\left(\mathcal{Q}\phi - \frac{2\pi}{\Lambda} r\cos\phi, 2\pi\right)\right] \tag{3.5.6}$$

where δ is the amplitude of the phase modulation and $\text{mod}(a,b) = a - b\,\text{int}(a/b)$.

3.5.2 Spiral Phase Plate

The spiral phase plate (SPP) is a helicoidal transmission optical device that imposes an azimuthally dependent phase retard on an incident optical wavefront [8, 47]. This is a transparent plate in which the thickness increases around the central axis of the plate. The SPP looks like a spiral staircase with a certain number of steps that progressively build the total phase gap h_s after a complete rotation of the azimuthal angle φ (see Fig. 3.6).

$$h = h_s \frac{\varphi}{2\pi} + h_0 \tag{3.5.7}$$

where h_s is the step height and h_0 the base height of the device.

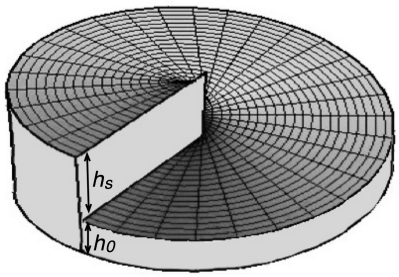

Figure 3.6: A spiral phase plate.

When an SPP is crossed by a light beam it imprints orbital angular momentum with a topological charge

$$\ell = \frac{h_s \Delta n}{\lambda} \tag{3.5.8}$$

where Δn is the difference between the refractive index of the SPPs material and the refractive index of the surrounding medium and λ the wavelength. The value of orbital angular momentum, expressed by ℓ, depends explicitly and implicitly (through the refractive index) on the wavelength of the incident light, betraying the chromatic nature of this device. The resulting phase distribution is visualized in Fig. 3.7

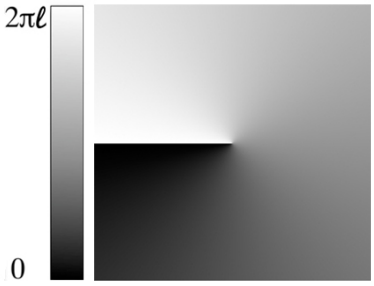

Figure 3.7: The phase distribution that an SPP imprints onto the transverse plane of an incident beam.

Differently from a FH, which imprints a vorticity with a topological charge depending on the diffraction order, an SPP has only the zero diffraction order. For this reason, the produced beam propagates along the same axis of the incident beam. A deeper investigation about spiral phase plate will be shown in the next chapter.

Chapter 4

Spiral phase plates $\ell = 2$ for optical vortex coronagraph

In this chapter we present the fabrication process and tests of two different types of $\ell = 2$ spiral phase plates (SPPs), designed for an Optical Vortex Coronagraph (OVC) in the visible wavelength regime. Each phase mask is realized dividing the spirals area in sectors respectively of 8 and 512 of levels using lithographic nanofabrication approach. The SPPs produces different optical vortices (OVs) with topological charge ℓ that depends on the number of steps and on the wavelength. We found that the residual light in the central dark region of the OV tends to zero as the number of steps increases.

E. Mari, G. Anzolin, F. Tamburini, M. Prasciolu, G. Umbriaco, A. Bianchini, C. Barbieri and F. Romanato *Fabrication and Testing of ℓ = 2 Optical Vortex phase masks for Coronography* Optics Express (2010) vol. 18 pp. 2339-2344

M. Prasciolu, F. Tamburini, G. Anzolin, E. Mari, M. Melli, A. Carpentiero, C. Barbieri and F. Romanato *Fabrication of a three-dimensional optical vortices phase mask for astronomy by means of electron-beam lithography.* Microelectronic Engineering (2009) vol. 86 (4-6) pp. 1103-1106

4.1 Introduction

The spiral phase plate (SPP) is a transparent plate, introduced in section 3.5.2, characterized by an increasing thickness around the central axis of the plate. It imposes an azimuthally dependent phase retard on an incident optical wavefront, imprinting a certain value of orbital angular momentum. We have characterized this particular optical device, designed for an optical vortex coronograph (OVC). The OVC is an innovative instrument that can be applied to both space and ground-based telescopes for direct imaging of planets around bright stars. It exploits the geometrical properties of the optical vortices produces by SPP inserted in the optical path rejecting the light of the on-axis star without altering that of off-axis sources. A deeper study of this instrument will be presented in the next chapter.

In the SPP, the total phase gap, h_s, after a complete rotation of the azimuthal angle φ, can be built in two possible ways (see Figure 4.1):

1. the thickness, and as a consequence also the phase of the light, is modulated smoothly and continuously. This is the ideal continuous phase mask (CSPP);

2. the SPP looks like a spiral staircase with a certain number of steps N that progressively build the total phase gap. This is called Multi-level Spiral Phase Plate (MLSPP) in which each step introduces a constant phase variation.

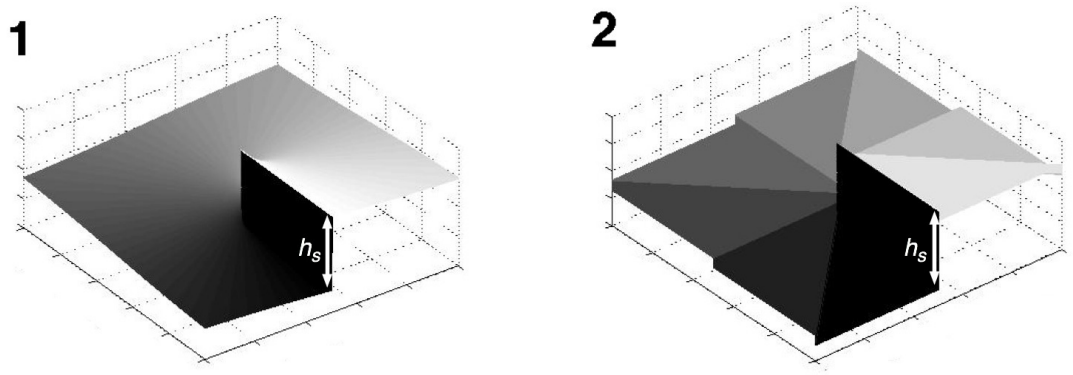

Figure 4.1: Simulated three-dimensional images of CSPP (left) and a MLSPP with 8 steps (right). h_s is the total phase gap built by the increasing thickness of the plate.

SPPs are built for a specific wavelength (λ_0) that produces a specific value of topological charge according to the formula [47]

$$\ell = \frac{\Delta n \cdot h_s}{\lambda_0} \tag{4.1.1}$$

where Δn is the difference between the refractive index of the SPPs material and the refractive index of the surrounding medium. This is valid for CSPPs. As a consequence the performances of SPPs are strongly dependent on the bandwidth of the incident beam.

We will illustrate the fabrication process and the optical tests of two different types of monochromatic $\ell = 2$ SPPs, designed for OVC in visible light (λ_0 = 550 nm). These SPPs differ from each other for the number of steps used to build the total phase gap.

4.2 Fabrication process

The SPPs were built by the Electron Beam Lithography (EBL). EBL is a powerful nanofabrication technique that allow the fabrication of three dimensional (3D) structures. It offers high flexibility in the elements design with good optical quality well adapted to the requirements of micro-optics [48]. The core of EBL process is the interaction between highly energetic electron beams and an electron-sensitive polymer material, called resist. The electron beam, entering the resist film, loses energy via elastic and inelastic collisions, namely electron scattering. The 3D profiles are obtained by changing locally the electron dosage, inducing changes in the dissolution rate of polymer film. After the development process, zones of polymer having different thicknesses are obtained.

For our experiments we have patterned a series of MLSPPs with 8 or 512 levels [49]. In Figure 4.2 scanning electron microscope (SEM) images of the optics are shown. The side of the squared MLSPP and the diameter of the other circular mask are 1 mm wide. The 3D-spiral phase

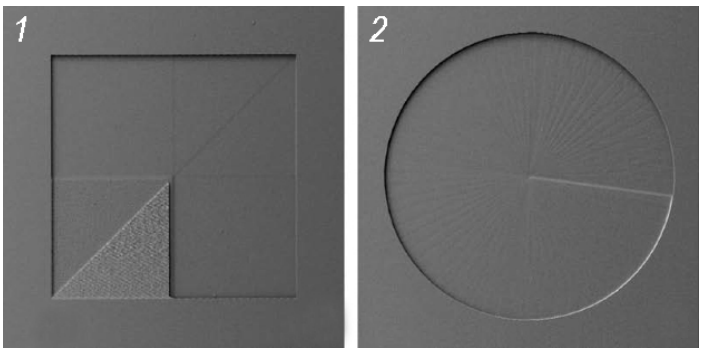

Figure 4.2: SEM images of fabricated SPPs with $\ell = 2$. (1) 8 phase levels, (2) 512 phase levels.

mask profiles were written on a 2.7 mm-thick polymethyl-methacrylate (PMMA) slide clinical grade free from Ultra-Violet absorber. The mechanical and optical properties of PMMA slide allow direct use as transmission phase mask in the OVC setup. Figure 4.3 shows the transmission profile of the PMMA slab used to build the SPPs. Data were obtained with a monochromator in an interval

spanning from 450 - 950 nm, i.e. from the Ultra Violet to the near infrared. In our range, λ_0 = 550 nm, the transmittivity function is quite good, of the order the 90%.

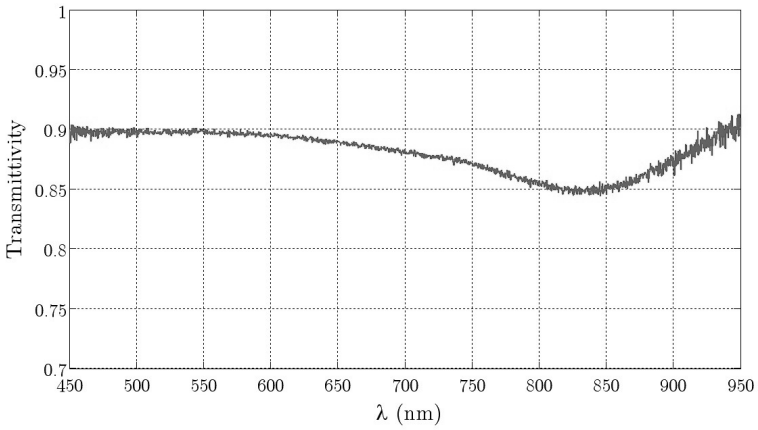

Figure 4.3: Transmittivity function of the PMMA bulk slab in the interval 450 - 950 nm.

The PMMA slide used for the fabrication of the masks has high electrical resistivity (about $10^{15}\Omega$ cm) that creates a charging effect highly affecting the EBL writing. In order to avoid this detrimental effect, on the top of the PMMA slide was evaporated a 50 nm-thick aluminum film. The thin layer was grounded with the EBL chuck, thus discarding the slide during the EBL writing. The metal layer can easily be removed in a 10:1 HF (10 H_2O : 1 HF 48%) solution bath before the development step. The 10:1 HF solution etching rate on PMMA is negligible. Electron-beam exposure was carried out at 30 kV with a beam probe currents of 100pA. The development process was performed in GG developer bath, a mixture of diethylene-glycolmonobutyl ether, morpholine, ethanolamine and deionized water, at 25°C for 30 minutes and rinsed in deionized water.

4.3 Optical tests

For the characterization of the SPPs we will show the results of our numerical simulations and we will discuss the tests of stepped SPPs performed at the Laboratory of Optics of the Department of Astronomy (University of Padova).

4.3.1 Numerical simulations

Continuous-SPPs produce OVs with a topological charge that depends on the jump h_s and on the wavelength λ_0 at which the maximum fainting of the on-axis source is obtained (equation 4.1.1) For a Multi Level SPP the equation (4.1.1) is not completely matched.

We found that the topological charge of the OVs depends also on the number of levels used to build the total phase gap. The structure of an MLSPP produces additional L-G terms in addition to the fundamental OAM mode. This implies that the central dark zone of the OV is partially filled, and its intensity distribution modified. As result, for given h_s and Δn, the maximum fainting inside the central singularity of the OV is obtained at a wavelength different than λ_0.

We developed new numerical codes in IDL to simulate the central fainting of the OVs produced by a CSPP and MLSPPs with different number of steps. We have encoded our SPPs and the Airy patterns of the simulated stars, like those produced by an ideal telescope without obstructions, in 4096 $\times$ 4096 matrices. The intensities of the ideal stellar sources were normalized to unity and the value of topological charge in equation (4.1.1) was fixed at $\ell = 2$. The fainting produced by the SPPs is defined as the ratio between the light passing through the phase mask and the Lyot stop, which aperture is equivalent to 0.8 times the exit pupil aperture, and the light that should pass through the same area when the SPP is removed. This ratio was calculated at the image plane, instead of in correspondence of the exit pupil plane [50]. This solution has minimized the error associated to the Fast Fourier Transform algorithm, hugely increasing the precision of the simulations.

Tab. 4.1 reports the new values of the maximum fainting obtained for the CSPP (indicated by symbol "∞") and for MLSPP having 8, 16, 32, 64, 128 and 512 steps and the corresponding wavelength at which the fainting is minimum.

Table 4.1: Values of the maximum fainting of the light passing through the SPPs and Lyot stop and the corresponding wavelengths at which they are obtained

N steps	Fainting	λ_{min}
8	2.27$\cdot 10^{-4}$	624
16	6.70$\cdot 10^{-5}$	585
32	1.75$\cdot 10^{-5}$	567
64	4.42$\cdot 10^{-6}$	558
128	1.09$\cdot 10^{-6}$	554
512	7.21$\cdot 10^{-8}$	551
∞	5.63$\cdot 10^{-10}$	550

We draw our attention to the fainting obtained in the ideal case of a CSPP. It resulted of the order of 10^{-10} in the monochromatic regime, which is close to the limit needed to image earth-like planets orbiting around nearby stars [51, 52]. This implies that the capability of the OVC is strongly connected with the technology and the challenging task of building the SPP device.

From our numerical results we can see that the wavelength at which the maximum fainting (λ_{min}) obtained is inversely proportional to the number of steps. We can express this behaviour, showed in Figure 4.4, with the approximated equation

$$\lambda_{min}^{N} = \lambda_{min}^{\infty} + \frac{\lambda_{min}^{\infty}}{N} \tag{4.3.1}$$

where λ_{min}^{∞} is the wavelength at which the maximum fainting of light is found for our CSPPs. We

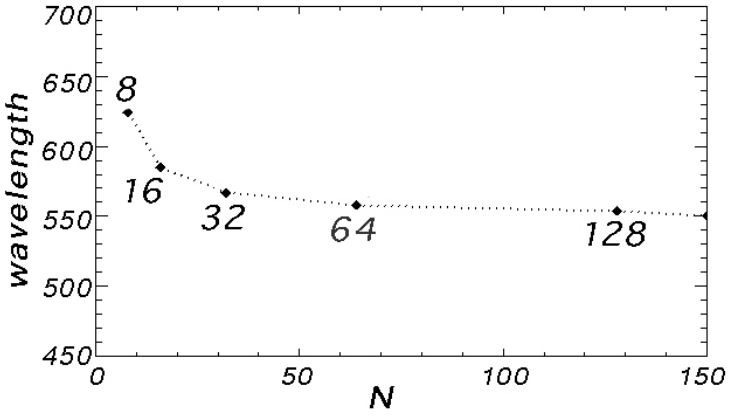

Figure 4.4: Maximum efficiency wavelenght for different MLSPPs. vs. number of steps.

can also define a relationship between the topological charge ℓ and N, starting from equations 4.1.1 and 4.3.1:

$$\ell = \frac{\Delta n \cdot h_s}{\lambda} \left(\frac{N+1}{N} \right) \tag{4.3.2}$$

Fig. 4.5 shows the fainting for each of the MLSPPs (8, 16, 32 steps) and for the CSPP with respect to the wavelength. The intensity scale has been normalized to that of a beam without any loss.

The dependence of the attenuation from the wavelength and the number of steps causes problems of chromaticity and contrast for the OVC. This behaviour strongly connects the capability of the instrument with the progress of technology. For this reason we have not used liquid crystal SPPs [53] because they have both a smaller spatial resolution and a smaller number of steps than those provided by EBL.

The best attenuation can be obtained with a CSPP within a narrow-band around the maximum efficiency wavelength. We estimate that a shift of $\pm$10 nm corresponds to a loss of contrast of about two orders of magnitude. The problem of chromaticity can be partially solved with the use of an achromatic SPP [54] that could guarantee a constant efficiency of the SPP across a bandwidth of 100 nm.

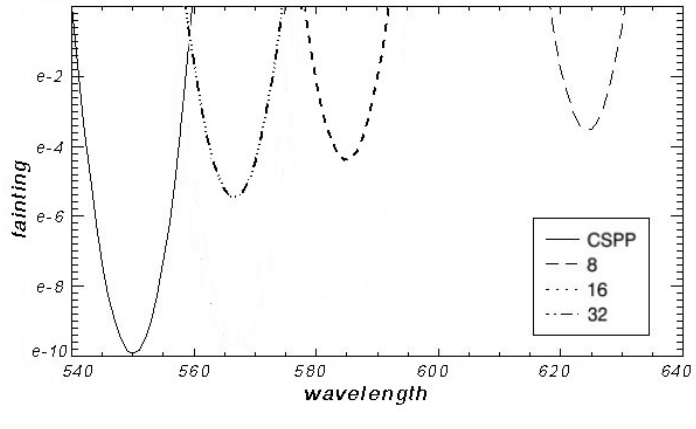

Figure 4.5: Fainting efficiency of the MLSPPs and of the ideal CSPP vs. the wavelength.

4.3.2 Laboratory tests

In this section we report the results of laboratory tests of two different MLSPPs with $N = 8$ and $N = 512$, having the same central jump of 2.2μm. We are interested in studying the behaviour of the masks also at wavelengths different than λ_0, for which the mask was designed. In fact, at the telescope it is not always possible to work in monochromatic regime because of the faintness of the sources. So, we tested the phase masks by comparing the experimental far-field diffraction pattern with numerical simulations using a He-Ne laser at 632.8 nm as the source of coherent light. Figure 4.6 shows the optical setup that reproduces the focal ratio $f/16$ of the Cassegrain configuration of the T122 Asiago Telescope. All images were recorded with a 1024 x 768 24-Bit Color CCD camera.

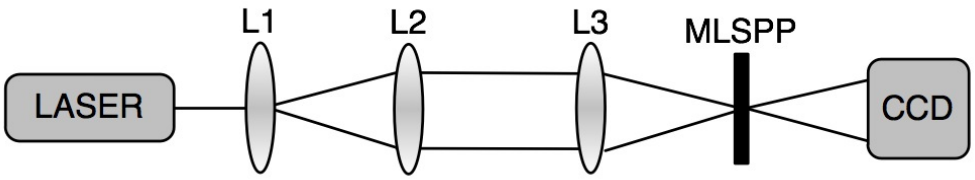

Figure 4.6: Optical setup used in laboratory for testing MLSPP. L1 and L2 are lenses that form a beam expander, L3 focuses light on the central dislocation of the SPP.

Examples of the experimental and simulated patterns are reported in top panel of Figure 4.7 for two differentely stepped SPPs. All the observed patterns contain spots with zero intensity in correspondence of the position of phase singularities. In the low panel isolines of the central zone

are reported.

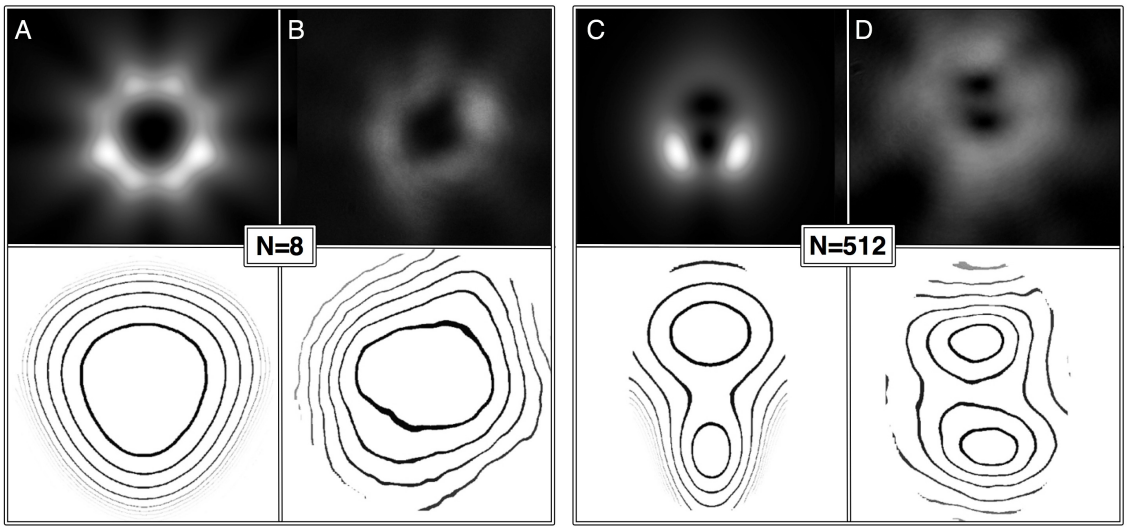

Figure 4.7: Simulated (A and C) and experimental (B and D) optical vortices obtained using SPPs with N=8 (left panel) and N=512 (right panel). Low panel shows the corresponding isolines of the dark zone of the optical vortices.

Fig. 4.8 shows the intensity profiles of the simulated (continuous line) and experimental (dash-dotted) OVs plotted with normalized intensities to put in evidence the existing similarities. In general, the experimental images are in quite good agreement with numerical simulations.

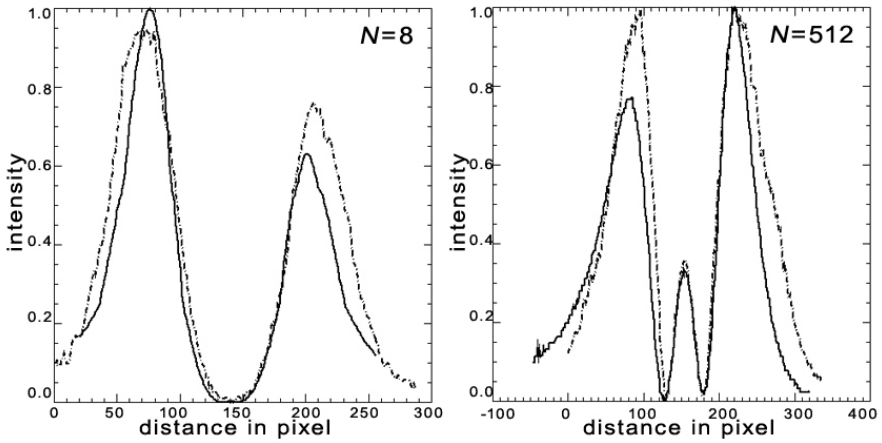

Figure 4.8: The profiles of the OVs shown in Fig. 4.7

The different patterns observed for the two MLSPP are due to the different topological charges of the OVs as predicted by equation 4.3.2. In fact, for $N = 8$ the maximum fainting is achieved at λ_{min}= 624 nm, that is quite close to that of the laser. For this reason, the OV of left panel present the expected central dark region. For $N = 512$, instead, the prediction is λ_{min}= 550 nm. As result, the light of the laser partially fills the central OV region, as shown by isolines of the right panel. The main differences observed between the numerical simulations and the corresponding experimental results are partially due to possible imperfections in the optical quality of the mask and/or to small misalignments in the optical setup affecting the symmetric shape of the OV.

So, we have analyzed the properties of MLSPPs at different wavelengths for future application in OVC. We have shown both numerically and experimentally that the topological charge of the OVs produced by MLSPPs depends on the number of steps N to build phase gap, even if the materials and the height of the total phase jump are the same. The number of steps N is crucial for the efficiency of the OVC.

Chapter 5

Optical Vortex Coronagraphy: introduction and astronomical demonstration

This chapter gives an overview of the instrumental concept of the otpical vortex coronagraph. I also report the results obtained with our first prototype of the optical vortex coronagraph, mounted at the 122 cm Asiago telescope. We test the instrument in the visible band, with a broad bandwidth filter, in seeing dominated visibility conditions. We used a chromatic spiral phase plate placed at the focus of the telescope to generate $\ell = 2$ optical vortex from the light of any star aligned with the telescope optical axis. The generated optical vortex is collimated and then blocked by a ring-shaped Lyot stop. The light of the off-axis sources remains unaffected. We have extinguished one of the component of the multiple stellar system Epsilon^2 Lyrae (ε^2 Lyr) by using the lucky imaging technique. A contrast of more than one order of magnitude was obtained at 2.3 arcsec from ε^2 Lyr C although it had a size of $\sim$1.75 arcsec FWHM with an almost Gaussian intensity profile because of the seeing effects.

E. Mari, F. Tamburini, G. Umbriaco, F. Romanato, G. A. Swartzlander Jr, Bo Thidé, C. Barbieri, and A. Bianchini *Astronomical demonstration of an optical vortex coronagraph at the 122 cm Asiago telescope in seeing dominated visibility conditions.* In preparation

5.1 Introduction

Coronagraphy was invented in 1939 by Lyot [55]. The first coronagraph was developed with the aim to suppress the light emitted by the disk of the Sun and observe the Solar corona. This first purpose gave the name to the instrument. Nowadays, with the term *coronagraph* we intend an optical device which allows to achieve high contrast with a single aperture telescope, without any connection with the original problem of observing the Solar corona. A practical definition that encompasses the current usage of this term is that a coronagraph is an optical system that rejects the stellar light from a predefined area of the focal plane of a telescope in order to reduce spurious effects produced by the associated speckle and photon shot noises [56].

Coronagraphic devices are at the present time being used for direct detection of faint sources around bright astrophysical objects. One of the primary goals of coronagraphs is to obtain images of terrestrial extrasolar planets. This important result was accomplished in 2010 by Serabyn *et al.* [57], when three exoplanets around the star HR 8799 have been discovered by using a phase mask coronograph.

The direct imaging of planets around a bright star is a challenging task because of the very high contrast ratio and the very small angular separation of the sources. In the case of giant extrasolar planets, a typical contrast ratio of $\sim 10^7$ is expected in the near infrared [58], while Earth-like planets are about $3-4$ orders magnitudes fainter, depending on the wavelength range (10^{-10} the visible [59] and 7×10^{-6} in the infrared [58]).

5.2 Visible or infrared?

Coronagraphs generally work within the visible bandwidth (700 - 400 nm, from red to violet), rather, for the moment, than within the infrared bandwidth (700 - 1000 nm). This is can be explained by several reasons:

- **Discoveries of extrasolar planets.**
  The wavelength (λ) is smaller within the visible bandwidth than the infrared. As a consequence the size of the optics (D) can be decreased, for a given angular resolution ($\Delta\theta = 1.22\lambda/D$). The second advantage is that the telescope can work at ambient temperature, while telescope that works in infrared band requires an environment cooled to 40 Kelvin. The third advantage is the flexibility that the visible allows in the design of a coronagraph for a given telescope. The visible band allows the direct application of conventional large telescopes for astronomical studies.

- **Chemical characterization of the planets.**
  The range of wavelengths in the visible band provides a set of spectral signatures much

broader than the infrared, from which one can derive many properties of the planets, including indicators of life and environmental conditions that lead to the creation and maintenance of life.

5.3 Coronagraphic concept

In the last years several coronagraphs have been developed, each of them characterized by different methods of rejection of the stellar light. This can be achieved basically in two ways:

- by inserting a stop in the image plane;
- by inserting a stop in the exit pupil plane.

The first solutions, like the original Lyot coronagraph, are generally one-stage Fourier spatial filters. Inserting a stop in the exit pupil plane implies that the coronographs have two (or in some cases more) stages of Fourier spatial filtering, one in the first image plane and one in the exit pupil plane.

Here we present a general model that describes the propagation of the wavefront between four consecutive planes [60] and that represents the current coronagraphic concepts. This general model is sketched in Fig. 5.1

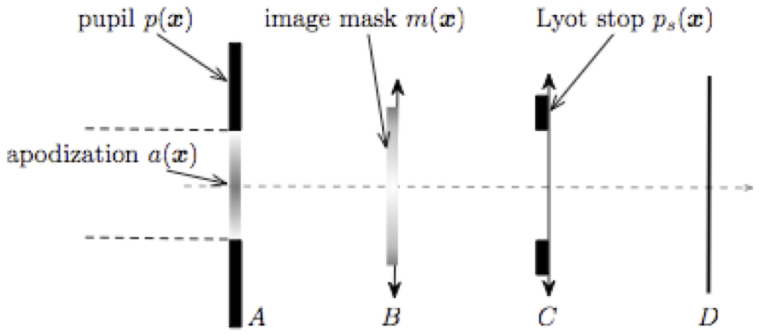

Figure 5.1: General and simplified model of a coronograph.

The four planes are A, B, C and D. A is the entrance pupil, usually is the aperture of the telescope, the coronagraphic mask is place in the plane B that represents the focal plane of the telescope, the Lyot stop is located in correspondence of the plane C, i.e. the exit pupil, D is the final focal plane where we collect the coronagraphic image. In each plane we define a complex transfer function of the position vector $\vec{r} = (r, \varphi)$ with respect to the optical axis: the aperture function of the telescope $A(\vec{r})$, the coronagraphic mask transmission function $T(\vec{r}) = 1 - M(\vec{r}))$

and the Lyot stop transmission function $LS(\vec{r})$. The exact mathematical expressions for $A(\vec{r})$, $T(\vec{r})$ and $LS(\vec{r})$ depends on the specific task required for the corresponding optical element.

Consider an optical wave $\Psi(\vec{r})$ with a complex amplitude before the aperture plane of the telescope. We assume that the wavefront is unaberrated, as it can be obtained in space or by using an adaptive optics system in ground-based telescopes. We make also the usual paraxial approximation, neglecting the quadratic phase terms associated with the propagation of the waves. So, we can easily explain the propagation of the wavefront between two consecutive planes in terms of classical Fourier optics [61]. Thus, the wavefront in the planes A, B, C and D can be calculated as:

$$\Psi_A(\vec{r}) = \Psi(\vec{r})A(\vec{r}) \tag{5.3.1a}$$

$$\Psi_B(\vec{r}) = \hat{\Psi}_A(\vec{r})T(\vec{r}) = \hat{\Psi}_A(\vec{r}) - M(\vec{r})\hat{\Psi}_A(\vec{r}) \tag{5.3.1b}$$

$$\Psi_C(\vec{r}) = \hat{\Psi}_B(\vec{r})LS(\vec{r}) = \Psi_A(\vec{r}) - [(\Psi_A(\vec{r}) \star \hat{M}(\vec{r}))]LS(\vec{r}) \tag{5.3.1c}$$

$$\Psi_D(\vec{r}) = \hat{\Psi}_C(\vec{r}) = \hat{\Psi}_A(\vec{r}) - [(\hat{\Psi}_A(\vec{r})M(\vec{r}))] \star \hat{LS}(\vec{r}) \tag{5.3.1d}$$

where $\hat{f}$ is the Fourier transform of a function f and $\star$ is the convolution operator defined by

$$(f \star g)(x) = \int f(y)g(x-y)dy = \int f(x-y)g(y)dy \tag{5.3.2}$$

The action of the phase mask is described in eq. (5.3.1b). The wave $\Psi_B(\vec{r})$ is the wave that have crossed the phase mask: the first term coincides with the wave entering the telescope pupil, while the second term corresponds to the wave diffracted by the phase mask. To obtain an efficient nulling effect, the second term must be canceled in the C plane by properly choosing the aperture, mask and Lyot stop functions (eq. (5.3.1c)).

Two techniques for design a coronagraph can be used:

1. concentrate the light of the on-axis star, thus reducing the diffracted light of off-axis sources;
2. reject the light of the on-axis star without altering that of off-axis sources.

The first case is to the *apodization* technique (see e.g. [62]). It can be achieved by using particular models of the aperture function $A(\vec{r})$. In the second case, instead, the two terms in eq. (5.3.1c) must balance each other (destructive interference) for the on-axis star, while only the second term must vanish for the off-axis source. This can be obtained by using coronagraphic masks having specific transmission functions that allow to modulate either the amplitude or the phase of the wavefront. Generally, phase masks are preferable with respect to amplitude masks. In fact, an amplitude mask produces an opaque zone that occults a significant fraction of the central field of view and, thus, all the sources located very close to the on-axis bright object.

Currently, a lot coronagraphic solutions containing phase mask have been developed. We report some examples.

- the phase mask coronagraph of Roddier and Roddier [63] based on a circular π-shifting focal plane mask;
- the phase knife coronagraph [64] based on a π-shifting screen;
- the annular groove phase mask coronagraph [58] based on a circular sub-wavelength grating.
- the vector vortex coronagraph [65, 57], based on the previous four quadrant phase mask coronagraph [66], based on a rotationally symmetric halfwave plate that provides a "geometrical" phase shift that applies opposite phase screws to the incident beam;
- the optical vortex coronagraph (OVC) [7] with a spiral phase plate inserted in the optical path.

The last two solutions exploit the nulling effect provided by the dark core of an OV.

5.3.1 Evaluation of coronagraphic performance

The performance of a coronagraphic design can be quantitatively described in terms of

- *useful throughput*, that is the maximum fraction of the companion light collected by the telescope that can be separated from starlight;
- *inner working angle* (IWA), commonly scaled to λ/D, defined as the minimal angular distance at which the throughput of the faint object is half of the maximal throughput [59].

5.4 Optical Vortex Coronagraphy: optical design for Asiago Galileo telescope

The Asiago OVC is designed in a Fourier transforming configuration, with the phase mask placed in the focal plane of the telescope. The optical scheme is shown in Figure 5.2.

The telescope scale in the $f/16$ Cassegrain configuration is 10.8″/mm. After the optics L_1 and L_2 the scale on the CCD plane is 8.5″/mm. which corresponds to a final $f/20$ relative aperture. On the left-hand side we show the image of a double stellar system S_1 and S_2 and on the right-hand side the output image produced by the OVC, where the on-axis S_1 is suppressed. The experimental results will be described in details in the next section. The light from the on-axis star S_1 is focused on the centre of the SPP and transformed into an OV with a central circular dark region. The so-called 'ring of fire' that surrounds the circular dark zone is collimated by lens L1, with focal length f_1, and blocked on exit pupil plane by the Lyot stop (LS) placed at a distance f_1 from the collimator L1. The light from the secondary source S_2 passes through the LS and then it

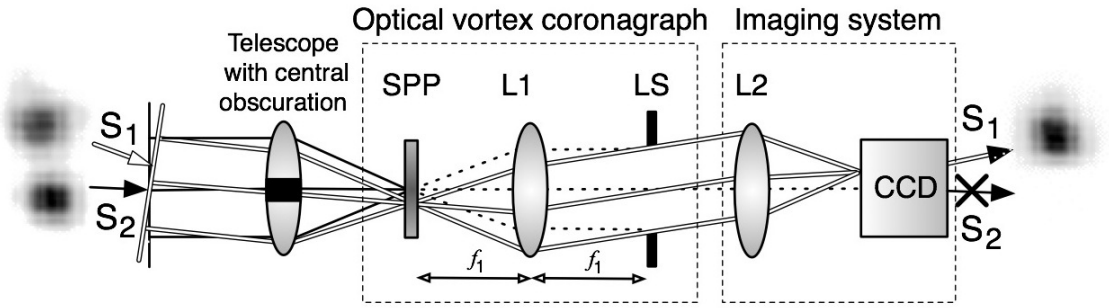

Figure 5.2: Optical vortex coronagraph at the Cassegrain focus of the 122 cm Galileo Telescope in Asiago (Italy).

is focused on the CCD by the camera lens L2. In fact, the secondary off-axis source crossing the phase mask far from the central optical singularity, does not acquire enough vorticity [67] and can be still detected. To illustrate an example of the performance of the OVC, we show in Figure 5.3 a laboratory test, performed using a SPP with 512 steps and two He-Ne lasers, with $\lambda = 632.8$ nm, separated by $4\lambda/D$. The optical system was design in order to simulate the same paraxial approximation of the $f/16$ Asiago Galileo telescope.

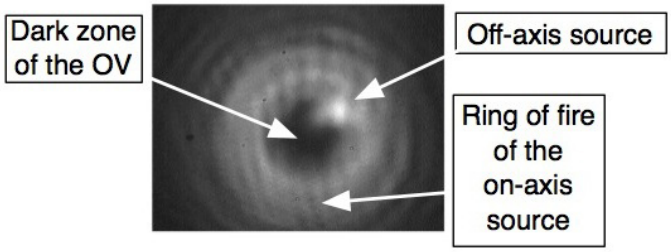

Figure 5.3: Laboratory test: image of the OV produced by an on-axis source. Inside the dark region the image of an off-axis source is clearly visible. The ring of fire can be suppressed by a Lyot Stop (see text).

The secondary source is clearly visible, as it is expected at the distance of $4\lambda/D$ from the primary [68].

5.5 Optical vortices produced by Airy diffraction pattern

In this section we present the mathematical description of the OV produced by incident beams with Airy diffraction pattern and the basic concepts of the Fourier transforming (FT) configuration of the OVC generated by an Airy disk.

In the ideal case of an OV produced by a diffraction limited telescope with a circular aperture and no central obscuration, the stellar image is described in terms of a separable and circularly symmetric function

$$E_\ell(r,\varphi) = A_\ell(r)\exp(\mathrm{i}\ell\varphi) \tag{5.5.1}$$

which FT, in the conjugated space (k,ϕ), is described in terms of the ℓ-th order Hankel transform ($H_\ell\{\}$)

$$u(k,\phi) = 2\pi(-\mathrm{i})^\ell\ \mathrm{e}^{\mathrm{i}\ell\phi}H_\ell\{A_\ell(r)\} \tag{5.5.2}$$

The circular aperture produces the Airy diffraction pattern

$$E(k,\phi) = 2\pi R^2 J_1(k\,R)/(k\,R) \tag{5.5.3}$$

where $J_1(k\,R)$ is the first-order Bessel function and R is the radius of the circular aperture. After having crossed the phase mask, the pattern of the diffracted light at the exit pupil is described by the FT of the product of equation (5.5.3) and a point vortex of even nonzero topological charge

$$\begin{aligned} E_\ell(r,\varphi) &= FT^{-1}\{2\pi R^2\mathrm{e}^{\mathrm{i}\ell\phi}J_1(k\,R)/k\,R\} \\ &= \mathrm{i}^\ell\mathrm{e}^{\mathrm{i}\ell\varphi}R\,H_\ell\{J_1(k\,R)/(k\,R)\} \end{aligned} \tag{5.5.4}$$

The pattern described by equation (5.5.4) is characterized by a circular dark region and $|\ell|/2-1$ concentric rings with zero amplitude superposed to the doughnut-shaped intensity distribution. In our case, the phase mask imprints to the on-axis beam the topological charge $\ell = 2$ and the solution becomes

$$E_{\pm 2} = \begin{cases} 0 & r < R \\ -\mathrm{e}^{\pm\,\mathrm{i}2\varphi}\,(R/r)^2 & r > R \end{cases}$$

where the second term describes the so-called *ring of fire* that surrounds the circular dark zone [52]. The choice of using an even-valued OV for the OVC is strongly recommended, because in this case OV provides an extended central zone of total darkness instead of the point-like region of darkness of an OV with odd ℓ [58, 52].

5.6 Optical vortices on ground-based telescopes

The intensity pattern of an OV generated with a phase mask placed near the focal plane of a telescope is affected by the point spread function (PSF), i. e. the spatial intensity distribution, of the stellar image [69]. Without the atmosphere, a stellar image would be determined by an Airy diffraction pattern, and the corresponding OV would be mathematically described as in the previous section 5.5.

Images taken with ground-based telescopes are instead subject to the blurring effect of the atmospheric turbulence (*seeing*). The typical *seeing image* of a star presents a Gaussian profile

with a full width at half maximum (FWHM) determined by the actual seeing conditions. Thus, when the seeing image crosses the SPP, it generates a different OV with respect to the one expected with a diffraction limited image. In Fig. 5.4 we show two numerically determined Fraunhofer diffraction images, in the exit pupil plane, for an $\ell = 2$ OV produced by a monochromatic Airy diffraction pattern (hereafter 'Airy-OV'), and one produced by a monochromatic Gaussian beam (hereafter 'Gaussian-OV').

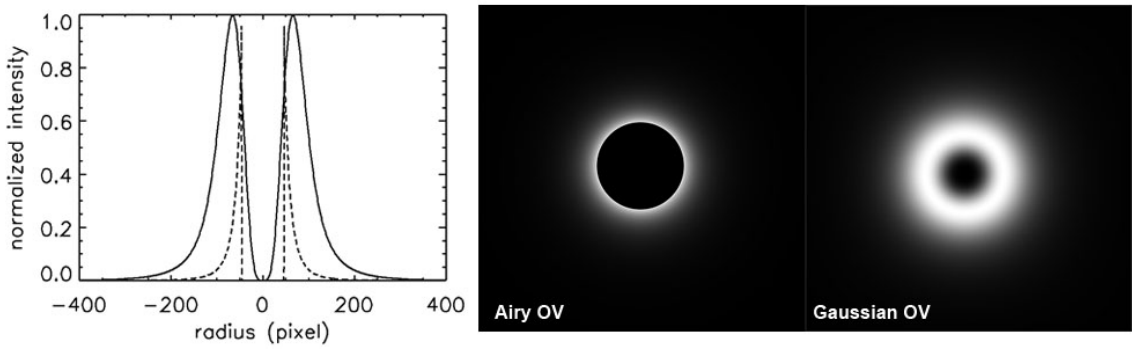

Figure 5.4: Numerically calculated intensity distributions of $\ell = 2$ monochromatic Airy-OV (center) and Gaussian-OV (right). Left panel: radial profiles of the two OVs. The solid line represents the Gaussian-OV, the dashed line the Airy-OV. In abscissa radius of the OVs in units of pixels. The Gaussian beam and the central Airy disk that produced the two OVs were simulated with the same FWHM.

In order to compare the two OVs, the input beams in the telescope focal plane, were chosen with the same FWHM. The intensity scale of the two profiles has been normalized to the maximum value. From the radial profiles shown in the left panel of Fig. 5.4 we see that in both cases the destructive interference due to the phase singularity along the optical axis produces a null intensity at the center. Gaussian-OV presents just a single point with zero intensity. Inside an Airy-OV, instead, the phase singularity produces an extended circular area with null intensity. Therefore, high-contrast OV coronagraphy can be achieved only with a diffraction-limited telescope. This is the reason why good adaptive optics correctors are required for the better performances of OVC on ground telescopes. Fig. 5.4 also shows that in an Airy-OV the light is concentrated in a sharp ring, whereas a Gaussian-OV produces smoother and broader intensity profiles with the results of a lower contrast in the central dark region [70].

A second critical task in the OV coronagraphy is to keep the stellar PSF on-axis with the central dislocation of the SPP. In fact, the atmospheric turbulence causes the stellar beam to wander around the line of sight. In this obseravtions we tried to solve this problem by adopting an imaging technique known as *lucky imaging* [71, 72, 73], adapted to the use of OVs [70].

Lucky imaging is one form of speckle imaging that can be used as alternative to adaptive optics in certain particular observing conditions. This technique uses a high-speed camera with

exposure times shorter than the turbulence timescale ($\sim 10 - 100$ ms in the optical/near infrared band). In this way single images, almost diffraction-limited and aligned with the dislocation of the SPP, can be occasionally produced. Typically, 1% - 10% of exposure frames are selected [73]. These 'lucky' exposures can be properly combined to produce a higher quality image.

5.7 Experimental results

The prototype of our OVC was tested at the Asiago 122 cm $f/16$ Galileo Telescope (Italy). We report the results obtained with the multiple system ε^2 Lyr under variable seeing conditions of $\sim 1.75 - 2.5$ arcseconds ($''$).

The multiple system ε^2 Lyr is composed by two stars: ε^2 Lyr C with magnitude mV = 5.1, and ε^2 Lyr D (mV = 5.5), separated by 2.3$''$ [74]. The components of this system have similar magnitudes, so we had a direct and immediate test of the efficiency of the OVC. ε^2 Lyr was observed in white light, with a bandwidth limited by the quantum efficiency response of the CCD camera, with a FWHM of 300 nm centered on $\lambda_0 = 550$ nm. The spectral transmittivity function of the lenses and of the SPP, made of polymethyl-methacrylate (PMMA), is flat in the interval 400 - 700 nm [75]. ε^2 Lyr D was suppressed by focusing the star onto the central dislocation of the SPP. The companion ε^2 Lyr C, instead, was imaged 2.3$''$ away from the central dislocation, so it passed almost unaffected through our 0.7 mm diameter LS.

We used a 1392$\times$1040 12-Bit CCD camera, with a pixel size of 4.65μm, in 4$\times$4 binning. The effective size of the pixels is therefore 18.6μm corresponding to 0.16$''$. This leads to a spatial Nyquist frequency of $(0.32'')^{-1}$[76]. Observing in the visible band, speckles [77, 78] have dimension of the order of $(550 \text{ nm}/D)$ radians, namely 0.09$''$. This value is lower than our 0.32$''$ sampling limit. For this reason we did not resolve individual speckles. We recorded a series of frames taken with an exposure time of $\sim$70 ms.

We made a selection of 'lucky' frames made of 39 frames , corresponding to the 2% of the total collected frames. In those frames the star is aligned with the central dislocation of the SPP in order to produce a fainting of at least one order of magnitude.

In Figure 5.5 we report the results obtained with the double system ε^2 Lyr observed without and with the insertion of the coronagraphic mask, respectively. The profile in the left hand-side upper panel shows the double system observed without phase mask. ε^2 Lyr C and D are both clearly visible. The result of inserting the SPP is shown in the right hand-side upper panel that represents the intensity profile taken along the intensity maxima of the double system so observed. The component ε^2 Lyr D of the double system was strongly attenuated. This intensity profile is the sum of the secondary off-axis star plus the residual light from the obscured star, so that in order to evaluate the actual perfomances of the OVC, we have de-blended the residual light of the on-axis star from the ideal Gaussian profile of the unobscured star (see Fig. 5.6).

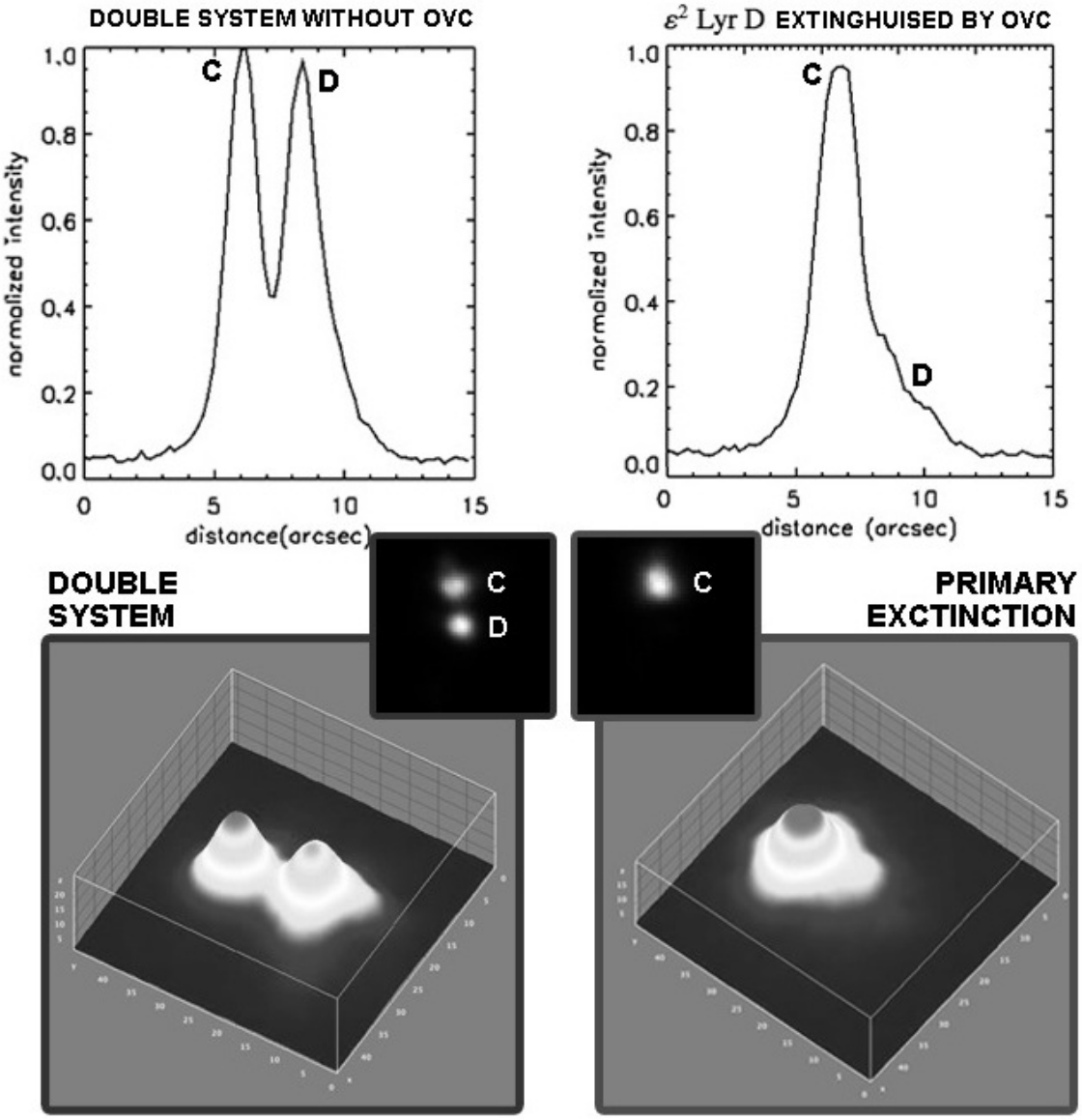

Figure 5.5: Coronagraphic experimental results of the double system Epsilon^2 Lyrae. 2% of total frames were selected and combined. *Left hand-side upper panel*: intensity profile taken without the phase mask along the intensity maxima of the two stars. *Right hand-side upper panel*: intensity profile of the double system observed with OVC. ε^2 Lyr D is extinguished. The abscissa reports distances in units of arcseconds. *Insets* represent the stellar images obtained with lucky imaging. The two *lower panels* show the respective three-dimensional intensity representations.

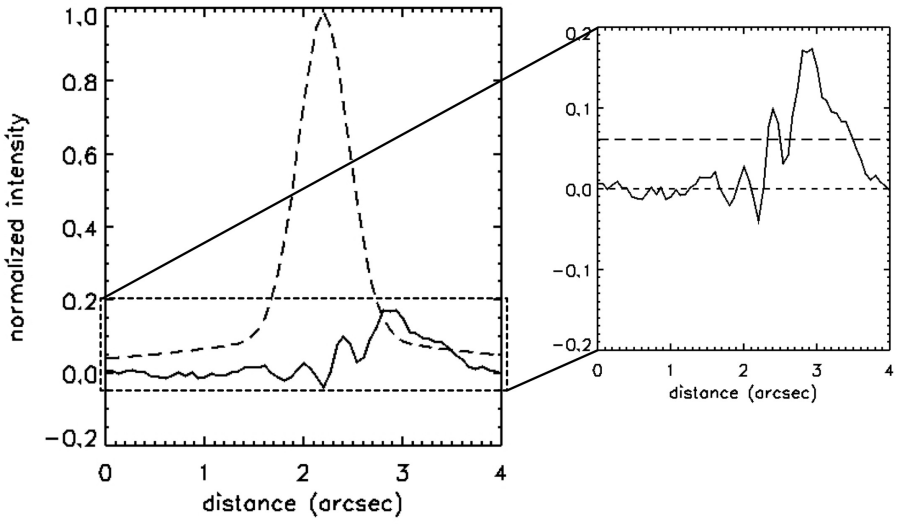

Figure 5.6: *Left panel*: the ideal Gaussian profile of the unobscured star (dashed line) and the residual light of Epsilon^2 Lyrae D (solid line). *Right panel*: enlargement of the residual light of Epsilon^2 Lyr D. The zero level corresponds to the average background calculated from the left portion of the residual light. The upper dashed line is the mean residual light.

The peak of the extinguished star passed from the normalized intensity value of one, to 0.171, whereas the mean residual light is around 0.06.

These results are not in agreement with a theoretical model [79, 80, 65] that puts in relationship the *Strehl ratio* with the rejection factor that is possible to achieved. The *Strehl ratio* (S) is defined as the ratio of the observed peak intensity at the detection plane from a point source as compared to the theoretical maximum peak intensity of a perfect imaging system working at the diffraction limit [12]. This is the simplest meaningful way of expressing the effect of wavefront aberrations on image quality. In our experiment we can estimate a Strehl ratio of the order of 10%.

Boccaletti *et al.* [79] defined the rejection factor R, i.e. the ratio of total intensity of the direct image to that of the coronagraphic image, at the first order, as $R \sim 4/\sigma^2$ where sigma is the amplitude of the phase aberrations. S allows to roughly estimate the attenuation by substituting the residual wavefront phase variance σ^2 from Marechal's approximation $S = e^{-\sigma^2}$, in the attenuation formula, obtaining

$$R = -4/\ln(S) \tag{5.7.1}$$

According to this equation the total rejection obtained by our prototype should result 1.7, whereas we have obtained a rejection factor of 5.85.

This mismatch could be explained by the optical quality or our spiral phase plate, carved in PMMA by electron beam lithography. The vector vortex coronagraph instrument [65], for example,

that have experimentally confirmed the eq. (5.7.1), that uses liquid crystal polymers, has a limited efficiency of attenuation around 10^{-6}. We have shown [50], through simulations, that OVC with a SPP placed in its optical path, can theoretically reach an attenuation of the order of 10^{-10}. This difference between the ideal attenuation that can be achieved with these two different instruments could be one of the reasons of the higher rejection factor obtained in the Asiago observations. A further investigation will be carried out.

5.8 Conclusions

We have built and mounted to the Asiago 122 cm Galileo telescope an optical vortex coronagraph prototype with a 512 step $\ell = 2$ SPP. We performed coronagraphic tests by fainting the light of one component of the double system Epsilon^2 Lyrae. Observations were performed under mediocre seeing conditions $\sim 1.75 - 2.5''$ with a 300 nm spectral bandwidth. The lucky imaging approach allowed to partially overcome the effects of the seeing. Selecting 2% of total frames in which the light from ε^2 Lyr D crossed the central singularity of the SPP, a fainting of the order of 10^{-1} was achieved, keeping unaffected the intensity of the secondary star.

We have thus shown that OV based coronography is a promising technique also for ground telescopes, provided adaptive optics is implemented, as demonstrated also by [81] and [57]. A further important improvement would be given by the use of an achromatic SPP [54] and a further analysis of the data will explain the mismatch with the theoretical model proposed by Boccaletti [79].

Chapter 6

Sub-Rayleigh resolution with optical vortices

We introduce a new optical vortex coronagraph(OVC) method to determine the angular distance between two sources when the separation is sub-Rayleigh. We have found a direct relationship between the position of the minima and the source angular separation. A priori knowledge about the location of the two sources is not required. The superresolution capabilities of an OVC, equipped with an $\ell = 2\,N$-step spiral phase plate in its optical path, were investigated numerically. The results of these investigations show that a fraction of the light, increasing with N, from the secondary source can be detected with a sub-Rayleigh resolution of at least 0.1 λ/D.

E. Mari, F. Tamburini, G. A. Swartzlander Jr., A. Bianchini, C. Barbieri, F. Romanato and B. Thidé *Sub-Rayleigh optical vortex coronagraphy.* Optics Express (2012) vol. 20 (3) pp. 2445–2451

6.1 Introduction

In 1879 Lord Rayleigh formulated a criterion that describes the resolving power of an imaging device, i.e. the ability to separate the superposed diffraction patterns of two equally-luminous point sources at a small angular distance.

I will consider only the case of a telescope, being relevent to this Thesis. The diffraction image produced by a diffraction-limited telescope with a circular aperture of radius a can be mathematically described by the Airy function

$$I(\theta) = I(0) \left[\frac{2J_1(ka \sin\theta)}{ka \sin\theta} \right]^2 \tag{6.1.1}$$

where $k = 2\pi/\lambda$ (λ is the wavelength), θ is the angle between the optical axis of the telescope and a point in the observation plane and J_m is the Bessel function of the first kind [12]. The Rayleigh criterion states that the diffraction images of two mutually incoherent point-like sources (Airy disks) are resolved when the maximum of intensity of one source overlaps the first intensity minimum of the second equally bright source. For a telescope having diameter $D = 2a$, at wavelength λ, the angular separation is achieved when [61]

$$\theta_R = 1.22 \, \frac{\lambda}{D} \tag{6.1.2}$$

This separability criterion for a telescope was based on the analysis of the superposed diffraction patterns produced by the two sources through a circular aperture. Lord Rayleigh said that *this rule is convenient on account of its simplicity and it is sufficiently accurate in view of the necessary uncertainty as to what exactly is meant by resolution* [82].

Fig. 6.1 shows how the superposed diffraction patterns appear for different separations of the two sources.

The separability limit defined by the Rayleigh criterion is a physical limit of any optical system. In the last decades different techniques to overcome this limit have been developed in certain special cases, especially in the fields of astronomical imaging [83] and microscopy [84]. For example, super-resolution can be achieved by using superlenses made with artificially engineered metamaterials [85, 86] or by using super-resolving pupils [87].

6.2 Optical resolution above Rayleigh criterion: methods exploiting OAM

The idea of using an optical vortex mask to detect faint objects with sub-Rayleigh resolution has been already suggested by Swartzlander [52] and Tamburini *et al.* [6].

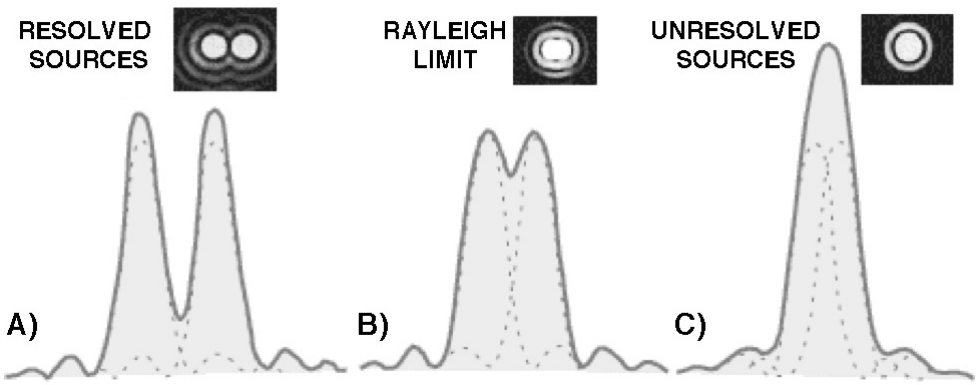

Figure 6.1: Images of the intensity distributions of two point sources as observed by a diffraction-limited telescope, and the corresponding radial profiles. (A) the two sources are resolved, (B) separated at the Rayleigh limit $\theta = 1.22\lambda/D$, (C) unresolved. Figure adapted from http://hyperphysics.phy-astr.gsu.edu/Hbase/phyopt/Raylei.html

Swartzlander proposed a method based on the analysis of the far-field intensity distributions produced by two vortex beams. Consider two infinitely-distant and incoherent point sources observed with a telescope having an aperture diameter D and a focal length f . The two fields radiate form distance monochromatic point source subtending an angle $\alpha \ll 1$. So, the corresponding EM waves are nearly collinear. An SPP is placed just before the aperture of the telescope in order to produce an optical vortex, opening a window that allows one to examine signals from other sources of light. The image formed at the focal plane of the telescope is the superposition of the intensity distributions produced by the two sources. Mathematically the intensity distribution at the focal plane can be calculated as the Fourier transform of the product between the fields of two plane waves and the transmission function of the SPP. When $\ell = 0$, two Airy patterns will be observed. In this case, the two sources are separated when $\alpha = \theta_R = 1.22\ \lambda/D$. Instead, if the SPP imposes a topological charge different from 0, then the two sources possess a symmetric 'doughnut' shape with a central dark spot. As a result, both radial profiles appear double peaked. When one of the two intensity peaks of one source overlaps with the vortex core of the other source, the Rayleigh criterion can be similarly satisfied. When $\ell = 1$, it can be demonstrated that the angular separation of the two sources corresponds to $0.64\theta_R$, which is lower than that provided by the Rayleigh criterion. By using SPPs with larger values of the topological charge, instead, the separation angles are larger than θ_R, namely $1.03\theta_R$ for $\ell = 2$, 1.37θ_R for $\ell = 3$, 1.71θ_R for $\ell = 4$ and so on.

This method could thus find its best application in astronomy, where it might be used to improve the resolving power of telescopes, but it would be necessary to built large SPPs to be placed before the aperture of the telescope. The application of this method is strongly limited by the

technological advance.

Another method to overcome the Rayleigh criterion that exploits the orbital angular momentum of light was proposed by Tamburini *et al.* It was demonstrated that, by using the topological properties of OVs, the resolving power of any optical instrument can be improved up to an order of magnitude below the Rayleigh criterion limit with white, incoherent light and even up to fifty times when monochromatic and coherent sources are used.

This criterion is based on the asymmetric intensity of the peaks of the OVs by using for two sources a combination of integer and non-integer values of ℓ, produced by a fork hologram blazed at the first diffraction order (see Sect. 3.5.1). One beam always coincides with the optical center of the hologram, thus generating an OV with integer topological charge $\ell = 1$. The other beam spanned the fork hologram in different positions starting from the optical center. For non-central positions the second beam formed an OV carrying non-integer components of OAM producing an asymmetric pattern. The central dark regions of the two OVs produced by the two sources are always superposed, because they have been generated by the same central optical singularity. When the two sources are superposed and they cross the optical singularity of the fork hologram, the profile is symmetric and the two maxima have the same intensity given by the exact superposition of two identical Laguerre Gauss modes. When the sources are separated by an angular distance below the Rayleigh criterion, the intensity of one of the two maxima decreases much faster than the other one, the latter tending to reach the intensity level of the single source. Using this property Tamburini *et al.* proposed a separability criterion based on the peaks intensity ratio, that can be resume as : *'that two identical sources are just resolved when the intensities of the asymmetric peaks differ by at least 5%'*.

6.3 Sub-Rayleigh coronagraphy

We now introduce a new criterion to determine the angular separation between two sources under sub-Rayleigh condition that exploits the position of the minima of the optical vortex generated by each off-axis source.This new method has been developed studying the superresolution capabilities of the optical vortex coronagraph (OVC), instrument described in the previous chapter. In order to clarify our results we report in this chapter the optical scheme of a general OVC (Fig.6.2).

We modeled two mutually incoherent monochromatic point sources, with the same wavelength, arranged at different angular separations. Observed by a diffraction-limited telescope, they would form two ideal Airy patterns that intersect the vortex lens at different transverse locations. Without vortex lens we should have the $\ell = 0$ case that for a single point source corresponds to the point spread function (PSF). When one of the source is aligned with the axis of the SPP, it forms a 'ring of fire' at the exit pupil plane (see Fig. 6.2), that then is ideally blocked from reaching the detector by the Lyot stop. A fraction of the light from the second off-axis source passes through

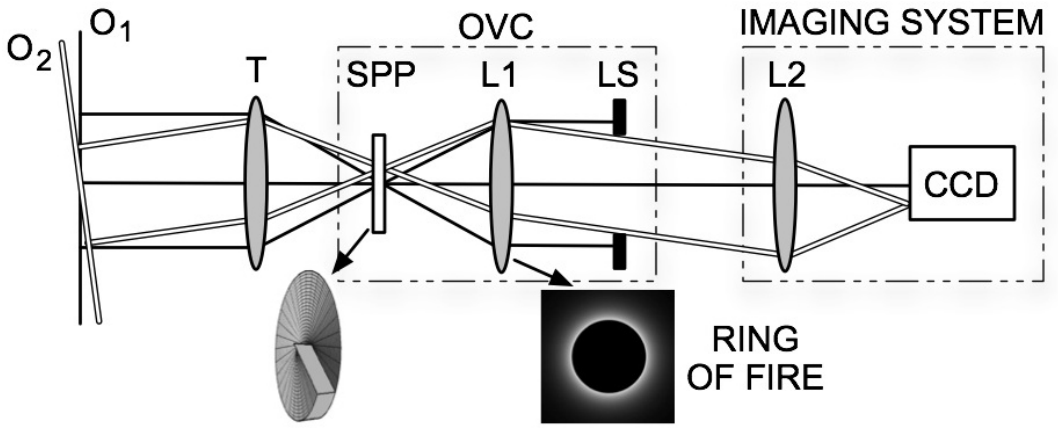

Figure 6.2: Optical scheme of an OVC. T is the telescope, L1 the collimating lens, and LS the Lyot stop, placed at the same focal distance as that of L1. The light of the on-axis object, O_1, crosses the central dislocation of the SPP and it is transformed into a 'ring of fire' in the back focal plane of L1. The ring of light is blocked by a Lyot stop LS placed in the back focal plane of L1. The light emitted by the off-axis source, O_2, evades the central dislocation of the SPP and the LS, so it is focused by L2 to be detected on the detector array CCD.

the Lyot stop and is recorded on the detector. The fraction depends on the angular separation of the sources, the diameter of the Lyot stop, and the surface profile of the SPP. Here we assume the area of the Lyot stop to be one half the area of the ring of fire [51]. This change the resolution criterion to $1.22\lambda/D'$, where $D' = D/\sqrt{2}$.

Fig. 6.3 shows the combined intensity distributions in the image plane for both sources, and the corresponding horizontal profiles observed without and with the $\ell = 2$ SPP with 512 steps. The unresolved peaks in Fig. 2(a) are separated by an angular distance of $0.1\lambda/D'$. The asymmetric doughnut pattern in Fig. 2(c) is attributed to the small separation of the image of the second source on the SPP from the vortex axis.

Figure 6.4 shows the separate image profiles for each source obtained by two independent measurements. Three cases are shown for different angular separations between the sources. We have found that the minima of the profiles of the asymmetric doughnut pattern occur exactly at the angular separation when the separation is sub-Rayleigh.

Fig. 6.5 shows a plot of minima position versus angular separation and an example of image profile for one beam when the other sources is completely nulled by the OVC. The two sources are separated by $0.2\lambda/D'$.

Therefore, a reliable measure of the sub-Rayleigh angular distance between two controlled point sources can be determined by measuring the position of the minimum of the OV generated by the off-axis source with respect to the optical axis. The measured profiles are the sum of the residual light of the primary plus that of the secondary source and the minima are absolute

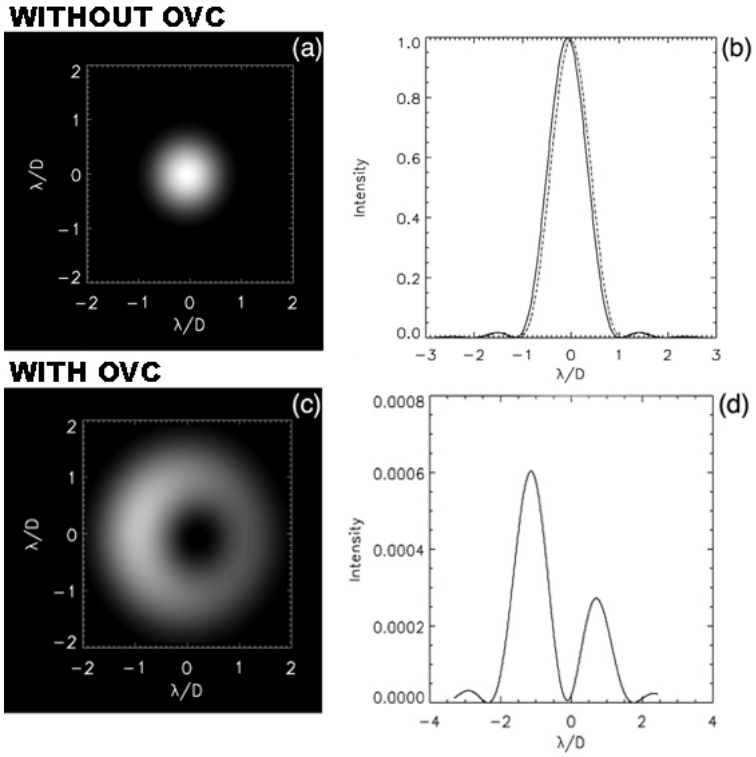

Figure 6.3: Numerically generated intensity distributions and profiles (a) Two unresolvable point sources with the same intensity separated by $0.1\lambda/D$ (b) corresponding intensity profiles (c) Intensity pattern of the off-axis source when crosses an $\ell = 2$ SPP (see text) and its intensity profile (d).

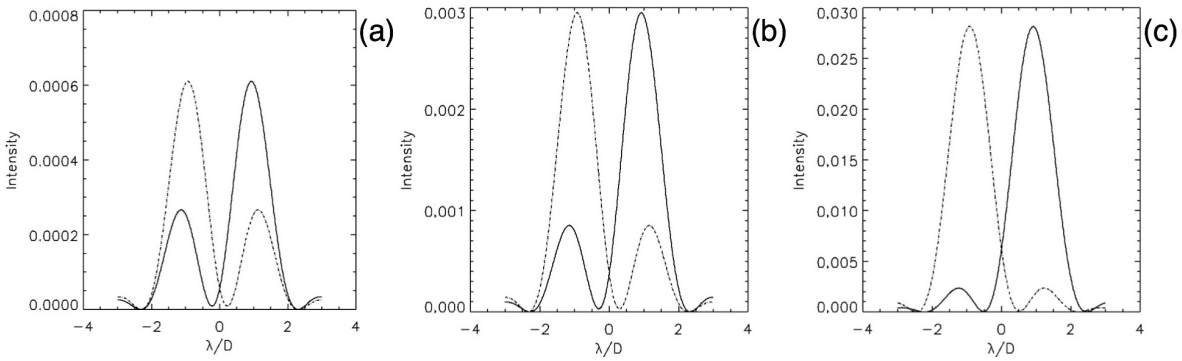

Figure 6.4: Numerically generated intensity profiles of two unresolvable point sources with the same intensity obtained by two independent measurements. Angular separations: (a) $0.1\lambda/D'$ (b) $0.2\lambda/D'$ (c) $0.5\lambda/D'$.

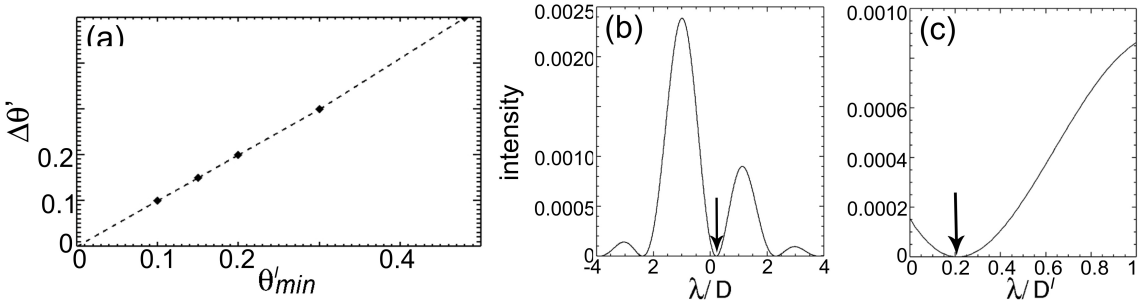

Figure 6.5: (a): Plot of minima position versus angular separation. points represent numerically calculated examples. (b): Numerically generated intensity profile of one of two unresolvable point sources with the same intensity. Arrow indicate the minimum position θ_{min} for the angular separation $0.2\lambda/D'$. (c) Enlargement of the minimum zone of the profile (b). The minimum occur exactly at the angular separation $0.2\lambda/D'$.

minima. The average power within the dark vortex core (see for example Fig. 6.4 (c)) is plotted in Fig. 6.6 for the case where the primary and secondary sources subtend a fixed angle of $\Delta\theta' = 0.3\lambda/D'$, and where the relative position of the axis of the SPP with respect to the primary source, $\Delta\theta'_{SPP}$ is varied. This corresponds to scanning the telescope across the sky and measuring the intensity within the vortex core on a CCD pixel. The plot demonstrates the correspondence between the minimum measured value(within the vortex core region) and the angle $\Delta\theta'$ when the primary is aligned with the SPP axis. The point $\Delta\theta'_{SPP} = 0$ corresponds to the alignment of the secondary source with the SPP axis. This plot shows that the position of the minimum power

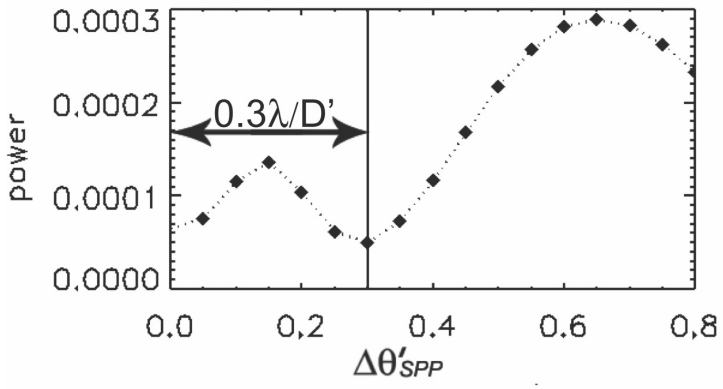

Figure 6.6: Power measured in the dark vortex core region when the sources subtend a fixed angle $\Delta\theta' = 0.3\lambda/D'$ and when the telescope is swept through an angle, $\Delta\theta'_{SPP}$ (along a line defined by the two sources). The position $\Delta\theta'_{SPP} = \Delta\theta'$ corresponds to an alignment of the SPP axis and the primary star.

indicates the angular distance of the secondary source from the primary. In other words the

absolute minimum is obtained when the primary is aligned with the SPP and, as a consequence, when $\Delta\theta' = \Delta\theta'_{SPP}$.

6.3.1 Numerical evaluation of the efficiency of detection of a secondary source

We calculated the percentage of power of the off-axis source transmitted through the LS. From an experimental point of view it is important to consider the surface profile of the SPP when it is multi-stepped. We numerically examined how the ideal results will differ when $N = 8, 16, 64$ and 512. Note that the $N = 8$ is the easiest to fabricate using lithographic methods [88].The Interactive Data Language (IDL) software routines encoded and manipulated the images by using a set of 4096×4096 matrices, where the diameter of the Airy disks were encoded in 20 pixels, and the exit pupil in 256 pixels. When the Airy diffraction pattern intersects the SPPs, the IDL routine calculates the output image point by point using the Fourier imaging technique [89, 90]. The intensities of the stellar sources were normalized to unity.

The secondary source is displaced in order to avoid that the center of the Airy disk falls on the highest step, i.e. the phase pitch. When the off-axis source is at sub-Rayleigh distance the Airy disk partially always cross the central singularity (Fig. 6.7).

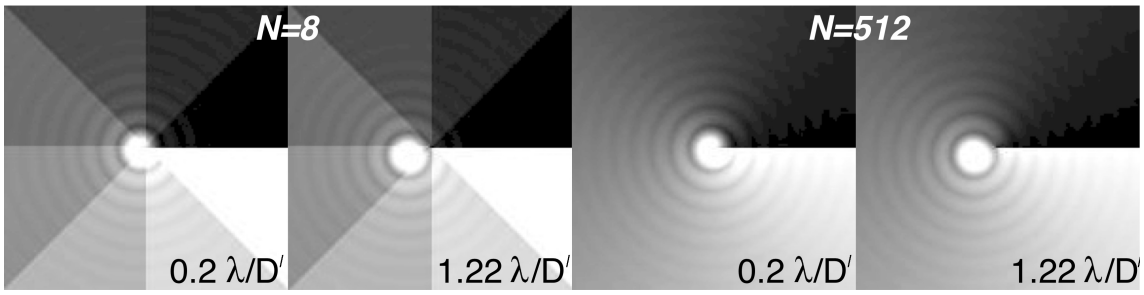

Figure 6.7: Off-axis secondary source crossing the SPPs at different distances. The center of the Airy disk does not cross the highest step.

Table 6.1 shows the numerical results obtained for different angular separations of the two sources.

From the calculated percentage of light, we see that the OVC has a transmission up to 100% at angular separations larger than $3\lambda/D'$. A certain percentage of the light from the secondary source passes through the LS to be detected even below the Rayleigh criterion [52, 6]. We find that the amount of light increases with the number of steps of the SPPs.

N \ $\Delta\theta'$	**0.1**	**0.2**	**0.5**	**1**	**1.22**	**1.5**	**2**	**3**
∞	0.58	2.36	15.39	56.94	74.25	88.17	97.25	100
512	0.57	2.35	15.37	56.84	74.13	88.17	97.16	100
64	0.54	2.28	15.21	56.16	73.25	87.42	96.31	100
16	0.52	2.06	13.94	51.72	67.76	81.39	90.09	98.99
8	0.49	1.99	10.78	40.07	53.32	69.98	79.22	95.37

Table 6.1: The percentage of the light of the secondary source passing through the LS with a diameter 0.7 times that of the exit pupil of the telescope. It depends on the number of the steps N used to build the total phase gap and on the angular distance $\Delta\theta$ in units of λ/D.

6.3.2 Results in graphical form

In confirmation of the numerical results shown in the previous section, we present here, in graphical form, some results obtained in the image plane with our numerical simulations of Table 6.1, below and above the Rayleigh criterion limit.

Figure 6.8 shows the intensity plots obtained by inserting an ideal continuous SPP in the OVC when around the primary star there is a companion with intensity 10^{-8} times lower that of the main source. When the secondary source is at angular distance $0.5\lambda/D'$, 15.4% of its light is visible. At

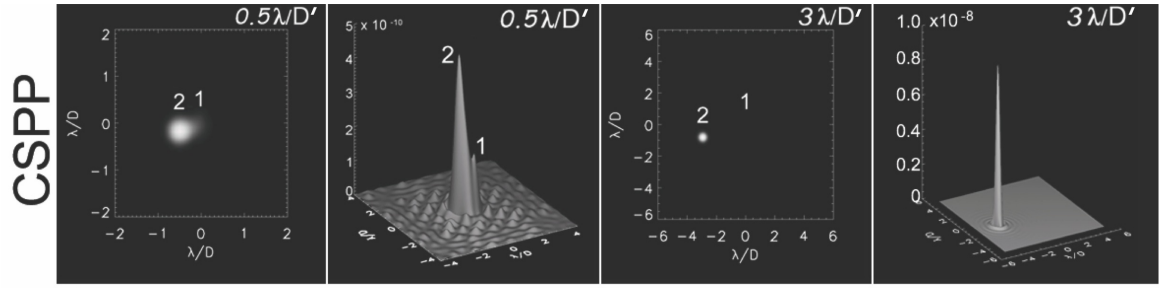

Figure 6.8: Coronagraphic image (2D and 3D) of a CSPP-OVC, when the two sources have an intensity ratio of 10^{-8}. 1 indicates the on-axis star and 2 the detected secondary source. Angular distances between two objects: $0.5\lambda/D'$ and $3\lambda/D'$.

$3\lambda/D'$, 100% of the detectable light of the secondary source passes through the LS.

Figure 6.9 presents the results obtained with $N = 8$ stepped SPP. The intensity ratio between the two sources was set to 10^{-2}. We have used different intensity ratios between two sources because each SPP has a different efficiency that depends on the number of steps [75].

For an SPP with $N = 8$, when $\Delta\theta = 0.5\lambda/D'$, the percentage decreases to 10.78%. From these plots we see that at $\Delta\theta = 0.5\lambda/D'$ the coronagraphic image loses its symmetry because of the presence of the secondary source. In fact, the OV produced by the on-axis source is partially

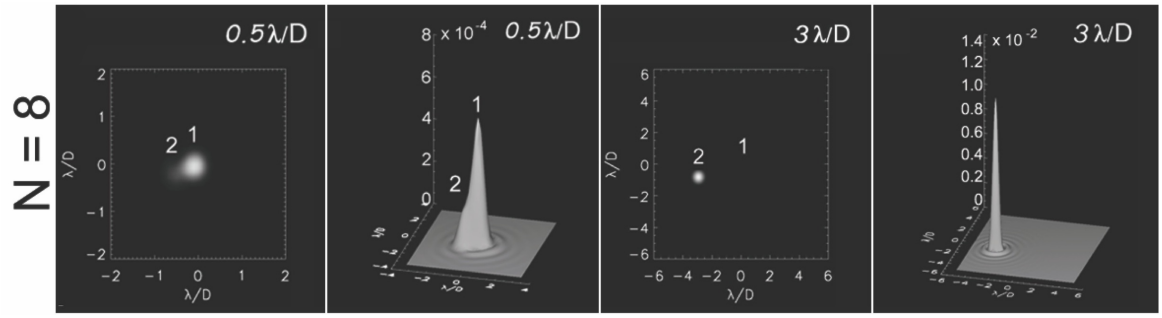

Figure 6.9: Simulated coronagraphic image in 2D and 3D for a MLSPP with 8 levels. Intensity ratio: 10^{-2}. Angular distances between two objects: $0.5\lambda/D'$ and $3\lambda/D'$.

filled by a portion of the light of the fainter companion, revealing its presence. Our results suggest that the OVC could be applied to the detection of the unresolved companions in double systems and to the study of planets that are approaching the star before a transit, i.e. when the planet is at angular distance below the Rayleigh limit.

6.4 Conclusions

We have introduced a new criterion to determine the angular separation between two sources above sub-Rayleigh condition. We exploit the asymmetric intensity distribution of the OVs produced by a double system that crosses an $\ell = 2$ SPP, and we found that the distance from the optical axis of the absolute minimum of the intensity of the OV is equal to the angular separation between the two sources. As a consequence, measuring the displacement of the absolute minimum of the OV from the center, we can determine the sub-Rayleigh angular distance. This minimum is obtained when the telescope is pointing exactly at one of the sources. So, the exact position of the bright source does not need to be known a priori. This is a new criterion different from the ones proposed in [6] and [52]. In fact, those schemes require the measurement of the maxima of an intensity distribution, whereas we propose to exploit the positions of the absolute minima.

We have also made a numerical study of the efficiency of the OVC simulating the separation of two sources at different angular distances with different $\ell = 2$ SPP. In the simulations the instrument was assumed to operate in the monochromatic regime. In all optical configurations considered, there is always a fraction of light from the fainter companion that becomes visible even below the Rayleigh criterion limit. The percentage of light from the secondary star passing through the LS increases with increasing angular separation. For this reason we suggest that OVC could be used as a pratical method to detect faint unresolved companions with ground-based and space-based telescopes, where the detrimental effects of the atmospheric turbulence

do not affect the profile of the OVs. The possibility of observing solar systems below the Rayleigh criterion will open new frontiers in the study of planet transit.

Chapter 7

Orbital angular momentum and vorticity in radio

The first experimental evidence that radio techniques can be used for synthesizing and analyzing non-integer electromagnetic orbital angular momentum of radiation is presented. The technique used amounts to sampling, in space and time, the EM field vectors and digitally processing the sampled data to calculate the vortex structure, the spatial phase distribution, and the OAM spectrum of the radiation. The experimental verification that OAM-carrying beams can be readily generated and exploited by using radio techniques paves the way for entirely new paradigms of radar and radio communication protocols.

F. Tamburini, E. Mari, B. Thidé, C. Barbieri, F. Romanato *Experimental verification of photon angular momentum and vorticity with radio techniques*. Applied Physics Letters (2011) vol. 99 (20) pp. 204102

7.1 Introduction

During the past few decades the use of orbital angular momentum has come to the fore in the optics range of the electromagnetic spectrum with several possible applications. Of course, the basic physical properties of the EM fields can be translated from optics to radio, but not too much work on this has been reported in the literature. In fact, OAM in radio range has been explored only since 2007 when numerical experiments showed how low-frequency radio beams can be readily prepared in pure OAM eigenstates and their superpositions by using antenna arrays of a kind already in use [91]. Thidé *et al.* [91] proposed to use such antenna arrays for generating and detecting both spin and orbital angular momentum in radio beams. The OAM-carrying fields can be generated in a simple way by a phased circular antenna array, where the N array elements are distributed equidistantly around the perimeter of the circle. The antennas are fed the same signal, and delayed relative to each other of a phase difference $\delta\varphi = 2\pi\ell N$ such that after a full circuit around the antenna array axis, the phase has been incremented by $2\pi\ell$. Singular antenna arrays of a similar type are used for various applications, including generating the so called phase modes in radio. The results of Thidé *et al.* shows that these modes may contain electromagnetic OAM.

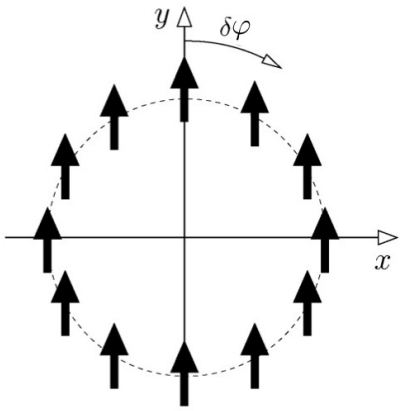

Figure 7.1: Configuration of a typical OAM-generating antenna array. In this case $N = 12$ antennas are equidistantly spaced along the perimeter in a circular geometry, phased such that $\delta\varphi = 2\pi\ell N$ [92].

If one wants to produce or detect OAM-carrying beams in arbitrary directions, one needs in such arrys to have access to the complete 3D vectors of the radio EM field. This can accomplished with vector antennas, e.g., tripoles [93]; crossed dipole antennas will be useful for beam directions nearly perpendicular to the antenna planes. The local 3D radio field vectors can be measured using digital samplers connected to each tripole. In this way they can be manipulated freely in software. This is in contrast to infrared and optical frequencies for which current detectors are incapable of measuring first-order field quantities, but are based on the use of second-order

quantities such as intensities and correlations, i.e. products of field quantities. Far field intensity patterns, calculated in these numerical simulations are displayed in Fig. 7.2 and are very similar to those obtained in paraxial optics.

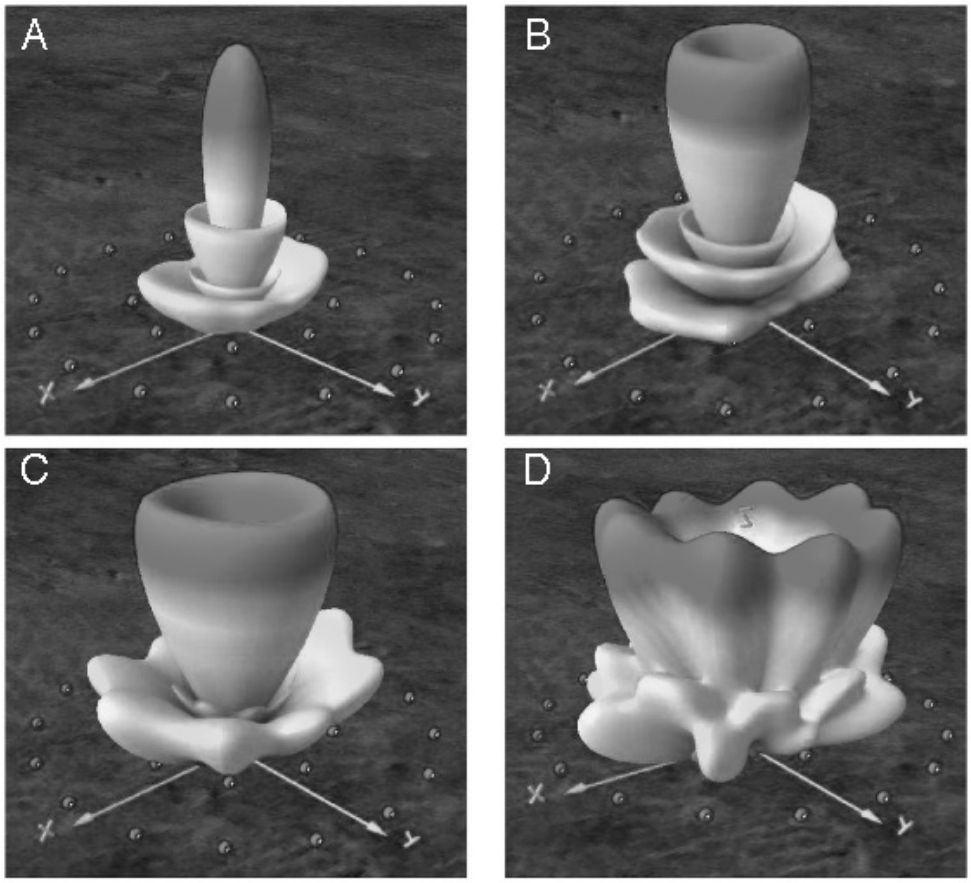

Figure 7.2: Radiation patterns for radio beams with $\ell = 0$ (A), $\ell = 1$ (B), $\ell = 2$ (C), and $\ell = 4$ (D). They have been numerically generated by one circle of 8 antennas and radius λ plus a concentric circle with 16 antennas and radius 2λ [91].

The results from these numerical calculations were experimentally confirmed in the laboratory tests reported in this chapter.

7.2 Experimental setup

In order to test the validity of the numerical experiments and to explore radio OAM, we performed a laboratory experiment in the large anechoic antenna chamber of the Ångström Laboratory of the Uppsala University, Sweden. The chamber is electromagnetically as well as acous-

tically/vibrationally shielded. The measurements were performed at 2.4 GHz (12.49 cm wavelength) and the source was realized with a commercial off-the-shelf (COTS) seven-element Yagi-Uda antenna for 2.4-2.5 GHz WLAN communications, fed with a continuous 0.01 watt monochromatic signal from a signal generator. The radio beam was reflected off a discrete eight-step staircase phase mask, that represent a discrete approximation of a non-focusing spiral reflector designed for a total 2π phase shift spiral; see fig. 7.3.

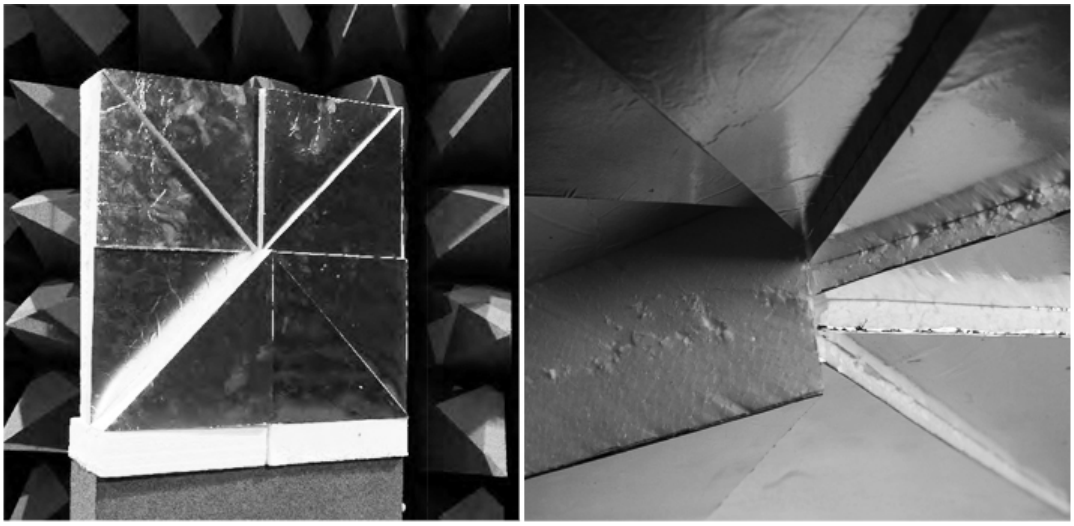

Figure 7.3: Spiral phase plate with 8 steps. Left: SPP inside the anechoic antenna chamber. Right: zoom of the central dislocation

The spiral reflector that imposes OAM to the antenna beam was made from styrofoam blocks, trimmed into a staircase-like structure with eight steps. Each of the eight surfaces were clad with aluminium foil, causing the corresponding part of the incident linearly polarised beam from the Yagi-Uda transmitting antenna to experience near total reflection. Each staircase of the structure introduced a local, successive, discontinuous phase step of $-\pi/8$ radians, except in the -45° direction where the phase step was 2π radians, causing the given part of the incident beam to acquire a phase shift. The reflector had N discrete jumps and a surface pitch h_s (in the right-handed sense). At the wavelength λ the reflected beam acquires a total OAM value evaluated as [50]

$$\ell = \frac{2h_s}{\lambda}\left(\frac{N+1}{N}\right) \tag{7.2.1}$$

For $h_s = -6.22$ cm, λ= 12.49 cm (ν= 2.40 GHz) and $N = 8$ as in the experiments reported here, this formula predicts that the reflected radio beam had a total non-integer OAM value of $\ell \approx 1.12$.

7.3 Results and data analysis

As first measurement we have detected the horizontal transverse component of the electric field of the reflected, twisted radio beam, E_x (Fig. 7.4), by using a single COTS electric dipole antenna for WLAN. The E_x was sampled in correspondence of fixed square grid points of 3 cm lattice period, reported on a plane placed in the far zone, about 55λ away from the non-focusing reflector.

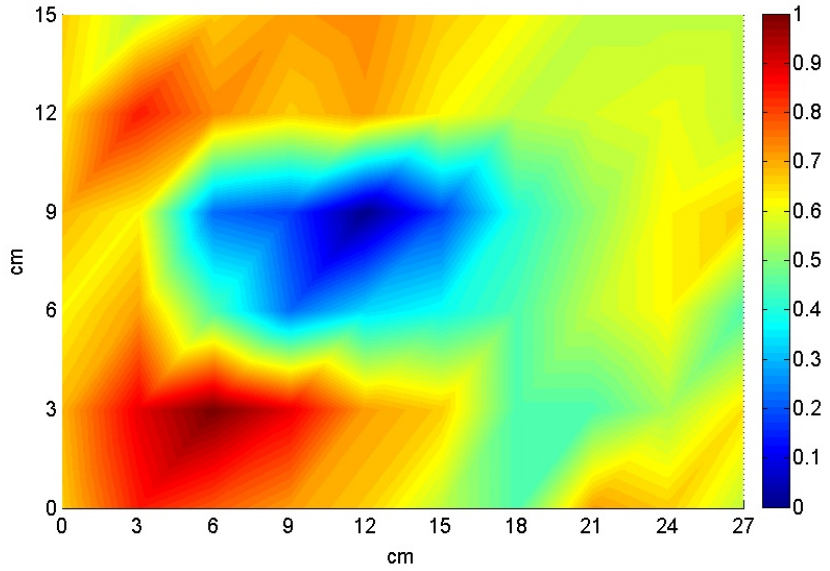

Figure 7.4: Map of the transverse electrical field intensity. Experimental map obtained by probing the radio beam in a plane perpendicular to the beam axis.

The spatial map of E_x shows the existence of OAM spatial field distribution in the radio beam represented by a sub-wavelength hairpin shaped configuration centered around a central minimum $(x = 12)$, $(y = 9)$ cm. In the ideal case of a beam endowed with a pure state OAM $\ell = \pm 1$, the typical fingerprint of a field intensity is a perfect doughnut-shaped intensity map (Fig. 7.3).

In our case the E_x field intensity distribution is slightly suppressed in the $+45°$ direction as an effect of the non-integer character of ℓ and of the corresponding imperfect phase matching over the full circuit around the central minimum. We have taken into account the expected non-integer OAM value $\ell = -1.12$ in the simulation of E_x map (Fig.7.6) obtaining a quite satisfactorily agreement with our experimental findings.

To determine the phase in the far zone, two identical COTS WLAN dipole antennas, both oriented along x-direction transverse to the radio beam axis, were used in a interferometric configuration set up. One of the receiving antennas was held at a fixed position far from the singularity, E_{x_0}, and conventionally taken at the maximum of E_x in order to maximize the signal response. The other antenna was moved around to sample the field signal at different fixed grid points. The

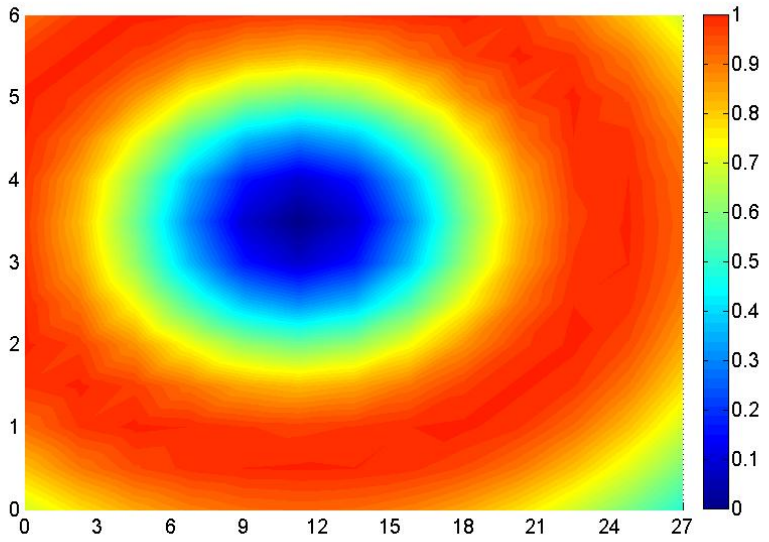

Figure 7.5: Simulation of the field intensity for the ideal case of $\ell = 1$. The intensity distribution show the typical symmetric doughnut shape.

difference of two antenna signals, $\Delta E_x = E_x - E_{x0}$, has been mapped out (Fig.7.7) and compared with the corresponding fields difference simulation (Fig. 7.8). The row experimental data show the presence of a strong modulation of the ΔE_x field characterized by a change of the sign along the direction of the step ($-45°$) and roughly centered on the singularity point.

The experimental and simulated phase distributions (Fig.7.9 and 7.10 respectively) have been extracted from the ΔE_x field (Fig.7.7 and 7.8) and the E_x field intensity map (Fig.7.4 and 7.6) by using the simple analytical formula

$$\cos\varphi = \frac{\Delta E_x^2 - E_{x_0}^2 - E_x^2}{2E_x E_{x_0}} \tag{7.3.1}$$

Notwithstanding some spurious signal in the experimental map, the major features of the spatial phase distribution are clearly recognizable. Namely, we observe the predicted distribution around the singularity point that eventually results in the 2π phase step line structure across $-45°$ to $+45°$ direction expected in correspondence of the phase mask cut (see Fig. 7.3). As expected, we found that the symmetry axis of the vortex structure and the phase singularity are both aligned with the mask center. Our simulations show that the monochromatic and coherent beam propagates in vacuum without any modification of the line phase singularity and without decaying into a cascade of pairs of vortex-antivortex like expected in a turbulent inhomogeneous medium. These features of phase map dependence clearly indicate the $\exp(\mathrm{i}\ell\varphi)$ electromagnetic OAM vortex structure harboured in the reflected radio beam.

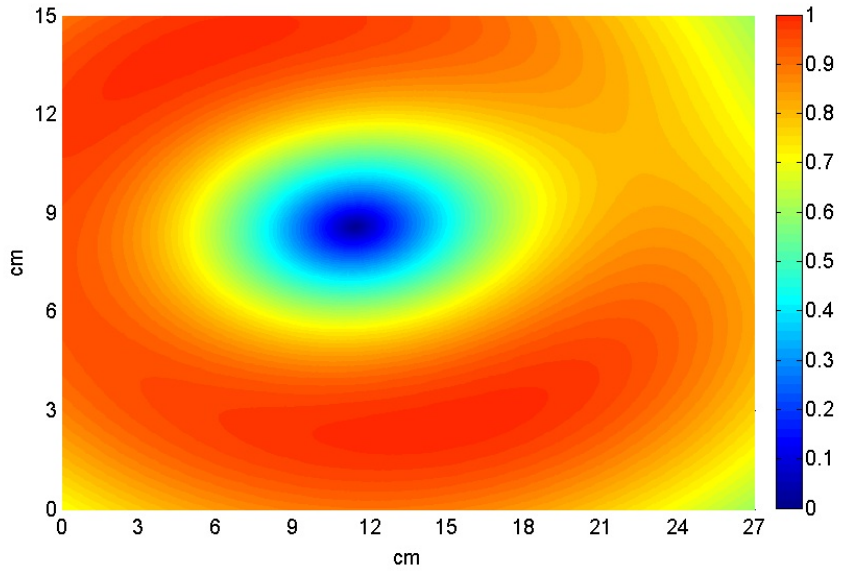

Figure 7.6: Simulation of the field intensity for $\ell = 1.12$. The colour scale is normalized to the maximum value measured of 7.5 μV/cm. The experimental map exhibits a deep minimum in the position correspondent of that where is expected from simulation the vortex singularity.

The OAM (spiral) spectrum of the experimental phase map has been computed [94] and reported in the inset of Fig. 7.9. The OAM components $\ell = 0, \ell = \pm 1$ and $\ell = \pm 2$ are the most relevant in particular for the experimental map, whereas the other higher OAM components ($|\ell| = 3, 4, ..., 10$) give only minor contributions to the intensity. Both the experimental and simulation OAM spectra show an asymmetric dominance towards the negative OAM components that represent an effect of the harbored vorticity, determining the direction of the phase gap rotation. More details can be found in Ref. [95] and references therein.

The presence of a range of integer OAM components in the experimental spiral spectrum confirms that the radio beam was not in a pure OAM state but, in accordance with Eq. (3.3.26), was a superposition of several orthogonal states, independent of each other and all at the same frequency. Each of these orthogonal OAM states of the total non-integer OAM beam can propagate, be detected, and characterized individually, thus enabling new methods and techniques for wireless communications based on topological diversity. The use of spiral spectra will reveal both the OAM content of an EM wave and the additional information of the spatial orientation of the source. This is a distinctive advantage over conventional experiments in which only products of EM field components (intensities, correlations, averages) are measurable. The emergence of completely new classes of fundamental as well as applied OAM-based studies in disciplines ranging from astrophysics [81, 57, 96] to high spectral efficiency wireless communications, both classically [97, 98] and quantum mechanically [99, 100], can therefore be envisaged.

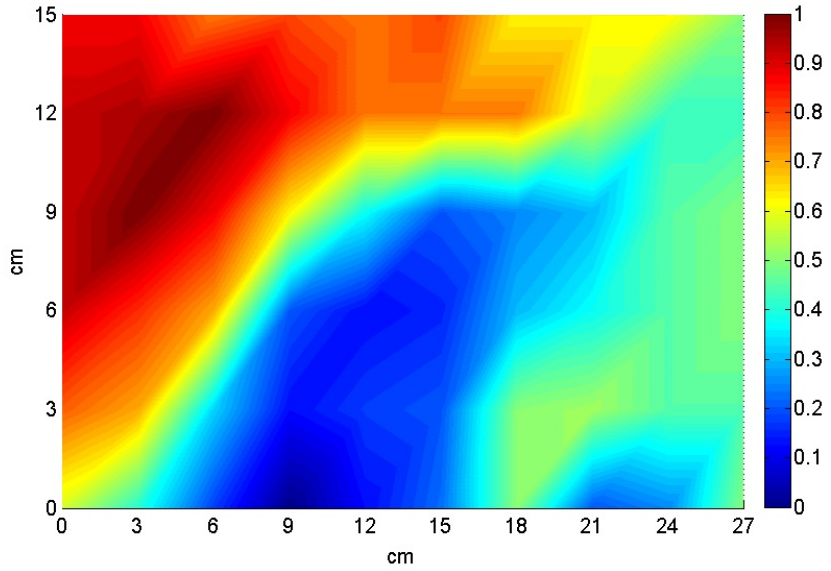

Figure 7.7: Experimental sum of the fields: sum of two antenna signals. The colour scale is normalized to the maximum value measured of $\approx 1m$ V/m.

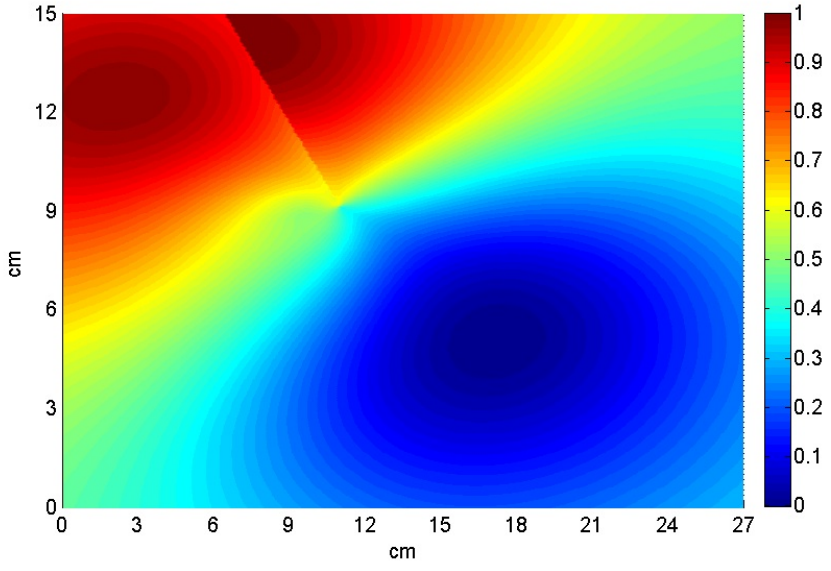

Figure 7.8: Numerical simulated sum of the fields.

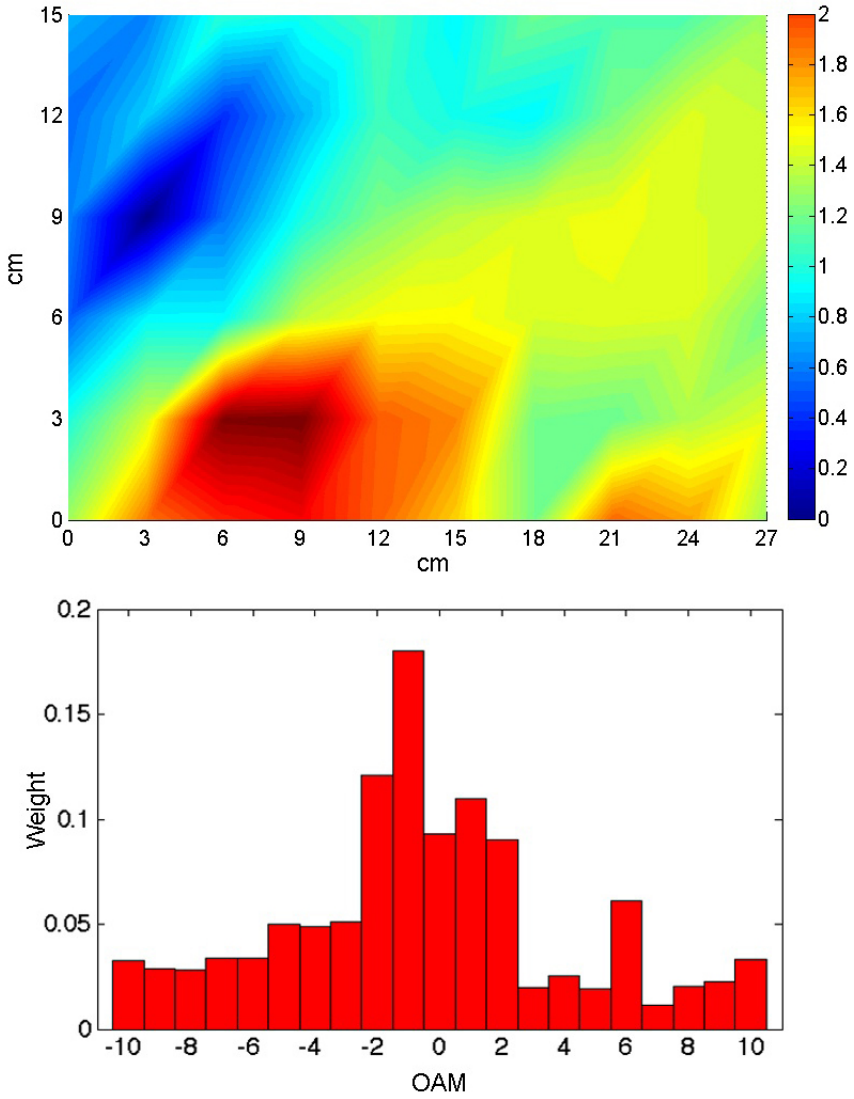

Figure 7.9: Phase map, based on measurements of the interference of two antenna signals as described in the text and, in the lower panel, the corresponding OAM spectrum. The biggest contribution is given, as expected, by $\ell = -1$. The map indicates the predicted phase step indicating the presence of a vortex structure, across the direction $-45°$ to $+45°$.

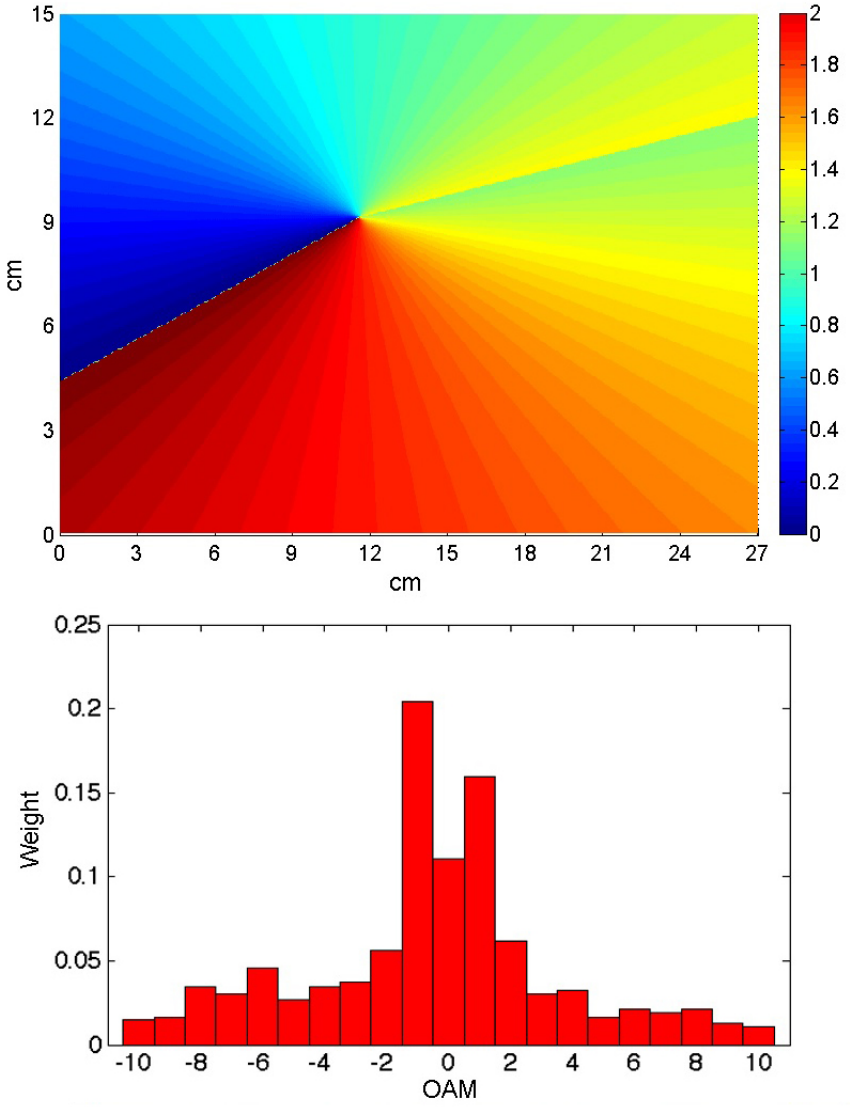

Figure 7.10: Simulated phase map and its corresponding OAM (spiral) spectrum.

Chapter 8

Communication with radio vorticity: more channels on the same frequency

We have shown experimentally how to propagate and use the properties of twisted non-monochromatic incoherent radio waves to simultaneously transmit two radio channels on the same frequency encoded with different orbital angular momentum states. This novel radio technique allows, in principle, the implementation of an infinite number of channels on one and the same frequency, even without using polarisation, multiport or dense coding techniques. This might represent a possible solution for the problem of radio band congestion, paving the way for entirely new paradigms in radio communication protocols.

F. Tamburini, E. Mari, B. Thidé, F. Romanato and C. Barbieri **Experimental verification of photon angular momentum and vorticity with radio techniques.** *Applied Physics Letters (2011) vol. 99 (20) pp. 204102*

8.1 Introduction

The first radio signal transmitted and received by Guglielmo Marconi on 8 December 1895 started the revolution of wireless communication in our modern world [101]. Nowadays, information is mostly exchanged through wireless channels and the rapid increase of the use of mobile devices has led to a congestion of the available radio bands even after the application of dense coding and channel sharing techniques [102].

Here we report results from real-world, outdoor experiments that demonstrate the feasibility of wireless information transfer over large distances that exploits the orbital angular momentum (OAM) states [103] of general electromagnetic waves. OAM states have been proved to be independent orthogonal physical states and can be generated, modulated and propagated independently without causing mutual interference between each other. EM-OAM is a fundamental physical property of the EM field that, applied to wireless communication, may offer additional degrees of freedom to use as a set of new orthogonal and independent communication channels at any given frequency become available.

Unlike already existing communication protocols that use the spatial phase distribution generated by a set of antennas to artificially increase the transmission bandwidth, the immediate advantage that can be provided by a protocol based on OAM states as independent communication channels is that of using the peculiar spatial phase distribution of each of these states as a reference pattern to generate, modulate and detect them in a better way.

In this chapter i report the proof that this property can be used for certain types of long-range communications, allowing for innovative physical coding schemes.

8.2 Experimental setup

To date, no one has managed to do a real radio transmission of twisted beams outdoor, in a real world-setting outdoor experiment, by using an that makes use of an incoherent achromatic wide frequency band of twisted radio beams. We prove experimentally that on one and the same frequency, the natural orthogonality of these states provide ideally an infinite set of independent transmission channels, each characterized by their unique spatial phase front topological charge.

To this end, we set up an experiment, generating and detecting two different channels on the same frequency: the first untwisted, with $\ell = 0$ orbital angular momentum, and the other with an $\ell = 1$ OAM twist. We have adopted a very basic hardware configuration made by two identical WiFi-FM transmitters, each with an output power of 2 Watts, driven by a signal generator. The transmitters were tuned to the carrier frequency of 2.414 GHz to feed the $\ell = 0$ and $\ell = 1$ antennas. In an FM transmission the amplitude and intensity of the EM wave remain constant in time; only the carrier frequency is modulated. The signal-to-noise ratio of the Wifi modules was 38 dB for the video channel and 45 dB for the audio band. The receiver sensitivity was -90dBm. The transmitted signal bandwidths of both signals were 15 MHz, such as those used in video signals.

The $\ell = 0$ source was generated by a commercial 16.5 dBi Yagi-Uda antenna [104, 105]. To generate the $\ell = 1$ vortex beam, we mechanically modified a 26 dBi commercial off-axis parabolic antenna, with diameter $D = 80$ cm, to attain an off-axis shaped spiral parabolic.

Yagi-Uda antennas

A Yagi-Uda antenna is a directional antenna consisting of a driven element (typically a dipole or folded dipole) and additional parasitic elements (usually a so-called reflector and one or more directors) [104, 105]. The reflector element is slightly longer (typically 5% longer) than the driven dipole, whereas the so-called directors are a little bit shorter (see Fig. 8.1). This design achieves a very substantial increase in the antenna's directionality and gain compared to a simple dipole.

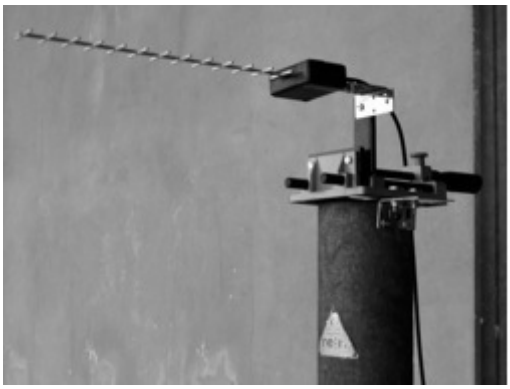

Figure 8.1: Yagi-Uda antenna in one of the interferometer's arms

In our experiments we used twelve-element, 16.5 dBi Yagi-Uda antennas for WiFi communications, tuned to 2.4 GHz. One as a linear polarisation, $\ell = 0$ emitter at the transmitting end, and two as a linear-polarisation phase interferometer at the receiving end. In Tab.8.1 we report technical details of the Yagi-Uda antennas.

Transmitter/receiver modules

The radio signals for the calibration and radio transmission were generated with commercial high-quality super-heterodyne frequency modulating (FM) transmitting modules using audio generator as modulation signal input. The deviation in frequency (≤ 27 MHz) due to the FM modulation of the carrier frequency (2.4 GHz) can be considered negligible and do not cause a significant distortion of the vortex or an ensuing change of the topological charge obtained with the twisted antenna. For modulation of the $\ell = 0$ beam, a sinusoidal audio modulation with the frequency of 400 Hz was used, while in the twisted channel was modulated at 1 KHz.

Table 8.1: Yagi-Uda antennas 16.5 dBi

Frequency [MHz]	2400-2480
Gain	$\approx$ 16.5 dBi
Size	$\approx 45\times5\times4$ cm
Vertical Irradiation (linear momentum)	35°
Horizontal Irradiation (linear momentum)	35°
Impedance	50 Ohm
SWR	< 1.3

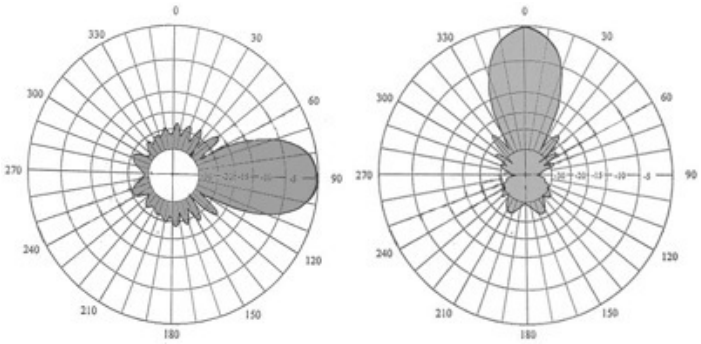

Figure 8.2: Horizontal and vertical diagram of the lobes of the Yagi-Uda antennas. The diagrams show a complicated pattern of the secondary lobes.

Offset vortex parabolic antenna

In order to have a single source of OAM radiation, we built a vortex reflector, using a pair of equal 80 cm, 15° offset, steel parabolic antennas for WiFi. One of the dishes was transformed by incrementally elevating, from the original shape, the surface of the quantities reported in the table 8.2 for given values of the azimuthal angle. The unmodified dish was used as mechanical support for the vortex antenna (Fig. 8.3).

Phase-difference interferometer

Since the $\ell = 0$ and $\ell = 1$ wavefronts have different shapes, we identified and measured the two radio signals, twisted and untwisted, by using an interferometric phase discrimination method that puts in evidence the wavefront phase fingerprints due to the twisting of electromagnetic waves [106, 3, 107, 108, 109].

The receiving station comprised a COTS (commercial off the shelf) frequency-modulation (FM)

Figure 8.3: Twisted parabolic antenna for generating $\ell = 1$ OAM channel.

Table 8.2: Offset vortex parabolic antenna: elevation of the surface with azimuthal angle.

Azimuthal angle	Elevation (in units of λ)	Elevation (cm)
$0 = 2\pi$	1/2	6.25
π/2	3/4	4.69
π	1/4	3.12
3/2π	1/8	1.56

radio module receiver fed by two identical 16.5 dBi Yagi-Uda antennas (hereafter antenna A and B), mounted on the top of two identical plastic columns connected together with 180° - phase-shifted cables through a beam adder module, in order to obtain a phase-difference interferometer. The baseline was of 4.50 meters, with laser controlled levelling and calibrated mutual distance. We decided to use such directive antennas to spatially reduce any possible background interference due to the presence of other WiFi sources. Antenna A was mounted on a mechanical translator oriented towards the direction of the transmitting station to select one of the two channels by exploiting the spatial phase front properties of different OAM states present in the two beams, whereas antenna B could be moved mechanically in the orthogonal horizontal direction only.

8.3 Intensity mapping of the field

As a first step, we characterized experimentally the physical properties of the twisted uncorrelated achromatic EM wave train, proving that vorticity can be actually radiated all the way to infinity [31]. In this way, we also proved that the topological properties of the twisted waves, namely the

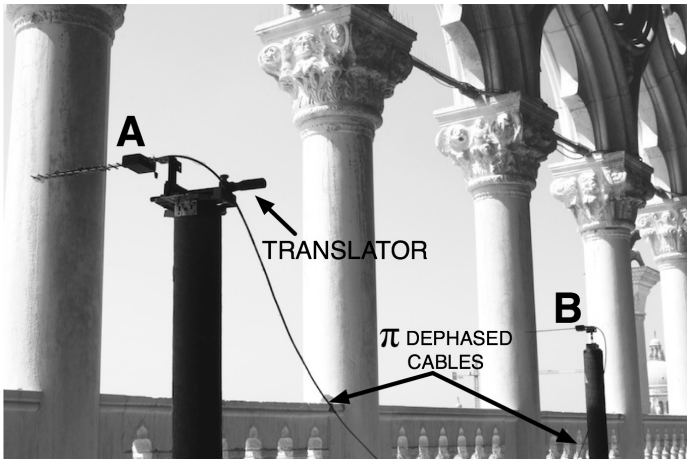

Figure 8.4: Phase-difference interferometer. Two identical Yagi-Uda antennas connected together with π dephased cables through a power-combiner adder module.

presence of the singularity and the spatial phase signature, are preserved in the far-field zone.

The intensity distribution of the radio vortex was mapped out 40 metres (320λ) distant from the transmitting antenna. We inserted a signal attenuator in the output of the transmission line for safety reasons. The mean signal background measured at $\lambda = 2.414$ GHz inside the 15 MHz bandwidth was -90 dBm. The polarisation was kept horizontal. The expected beam waist was given by the diffraction limit of the antenna, $\delta\varphi = 1.22(\lambda/D) \approx 10.9^{\circ}$ and the half-power beam width (HPBW), the angular separation between the points on the antenna radiation pattern at which the power drops to one-half (-3 dB) its maximum value, was found to be $\theta = k\lambda/D = 8.75^{\circ}$. The characteristic parameter of the antenna k is a factor that depends on the shape of the reflector and the method of illumination. The HPBW diameter of the twsted parabolic antenna at 40 metres distance is on the order of 6 meters. As shown in Figure 8.5, the region where the radio signal intensity, i.e., its linear momentum, was not detectable had a diameter of 21 cm ($\sim 1.7\lambda$) and we determined the position of the field singularity with an inaccuracy of 3 cm ($\sim 0.24\lambda$). The experimental limitations were dictated by the resolving power of the spectrum analyzer used in the field sampling. The average intensity measured in the 3 cm region around the singularity was -82 dBm.

The confirmation that the minimum found was the phase singularity of the field was obtained by measuring the phase distribution around it with a phase interferometer constructed from two identical Yagi-Uda antennas deployed along a baseline perpendicular to the direction of the transmitters. First we positioned the centre of the interferometer's baseline where the minimum of the field was measured, then, we mechanically tilted the transmitting antenna in the horizontal and vertical directions and measured the phase change. Finally, we verified the phase and field intensity distribution of the Yagi-Uda antenna used for transmitting the untwisted signal. No appreciable

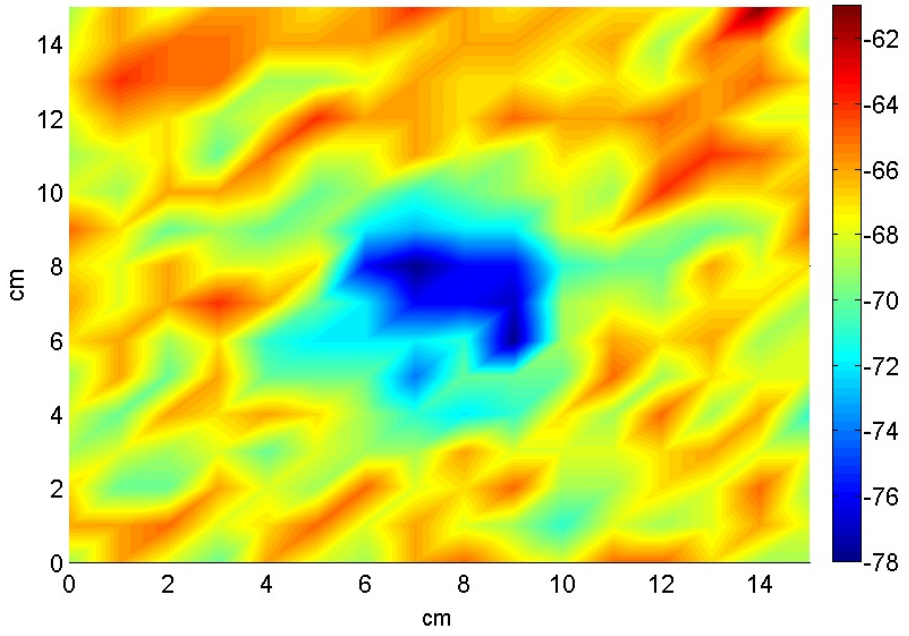

Figure 8.5: Intensity map of the radio beam vortex at 40 metres in free space in the region harbouring the singularity. The beam was attenuated because of its high strength. The intensity distribution in this region exhibits fluctuations caused by environmental interference effects. The central dip indicates the region where the field singularity is located, less than 3 cm wide, with a measured intensity of -82 dBm. The actual position of the singularity was confirmed by the phase change measured by the two-antenna interferometer.

phase twist in the Yagi-Uda beam was detected.

8.4 Radio transmission with OAM

After having verified that the properties of the twisted beam were preserved, by analyzing the beam shape with an intensity/spectrum analyzer, we performed the experiment with the purpose of encoding two different signals in the two different spatial modes on the same frequency of 2.414 GHz, and within a fixed given bandwidth. We transmitted and received the two channels in the directory from the lighthouse of San Giorgio island to the balcony of Palazzo Ducale in Venice, separated by 442 metres (3536λ). The HPBW diameter of the main lobe was 67 meters. At the point of the phase singularity we expect the field to drop almost to zero, as found in experiments at optical frequencies.

The darker zone where the central singularity was located, identified by a dramatic drop down to 10 dBm of the averaged field intensity, had a diameter of about 2λ. This small region was

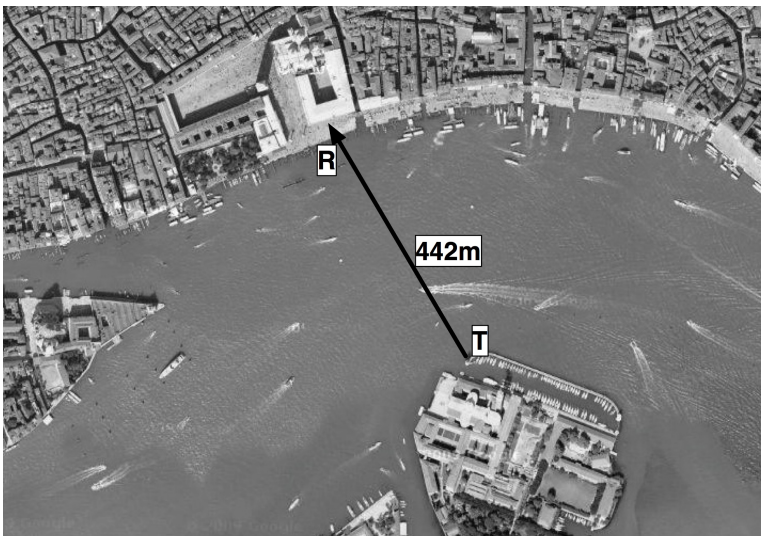

Figure 8.6: Site of San Marco experiment in Venice. T: transmitter inside the lighthouse of San Giorgio island. R: receiving station in Palazzo Ducale.

contained inside a wider zone with ~ 190 cm ($\sim 15\lambda$) diameter where a smooth decrease of the mean field intensity from 3 to 5 dB was observed. Outside this region, at distances larger than 2 meters ($\sim 16\lambda$) from the singularity, the field intensity was found to be more stable and flatter. The measured signal intensity was only 3 dB lower than what is expected from a non-helicoidal parabolic antenna with the same diameter and focal length. The field strength, measured around the beam singularity, was higher than expected from a perfectly coherent beam. In fact, the antenna lobe presented an intensity shape similar to that of a non-coherent beam. So, the expected central intensity dark hole was partially filled up and the phase distribution preserved. After the propagation, the signal intensity near the singularity, where the electric field is expected to tend to zero, exhibited a more uniform and flatter intensity profile as would be expected from a coherent beam with a Laguerre-Gaussian profile. This actually suggests behaviour typical of incoherent beams carrying OAM. Such beams preserve the phase profile but the region of the lobe in which the singularity is located appears much more filled by the signal because of the presence of a large width of the transmission band and, probably, also because of the shape of the transmitting antenna. The only insignificant variable interference effects that were detected during the experiments were due to reflections of the beam from the water surface of the lagoon that varied with the tidal height of the sea.

The interferometer, i.e. the receiving station, measured the phase difference between the two antennas, $A - B$, and therefore characterized the spatial phase properties of the beams, that are the fingerprints of different vorticity OAM states of the field. To discriminate the two different spatial modes of the EM field, we aligned antenna A, antenna B and the field singularity along

the same line parallel to the horizon, and the singularity was set in the middle of the segment delimited by antennas A and B (Fig 8.7).

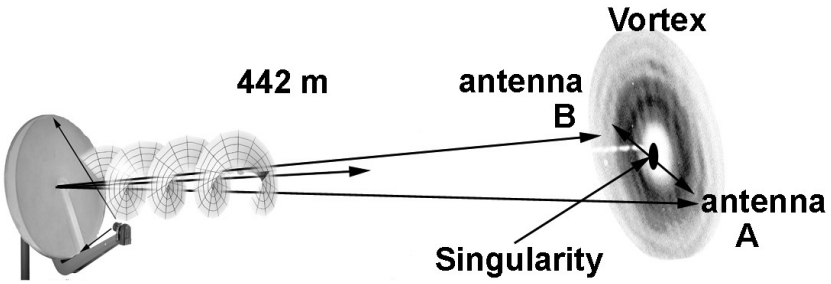

Figure 8.7: Scheme of the experiment in San Marco (not in scale). From left to right: the transmitting antenna, the two antennas A and B aligned with the singularity of the beam, located in the middle of the segment AB.

During the experiment, the main practical difficulty was that of positioning the singularity in the middle of the two Yagi antennas, that was then solved with the find-and-track direction method [110], commonly used to locate with precision a radio transmitter. If the setup were perfectly aligned, the twisted EM wave would have shown an exact π azimuthal phase difference between the two antennas, subsequently compensated by the cable electric delay thus producing an intensity maximum. For the untwisted beam, instead, a minimum is found in the same position.

EM waves with wavelength λ, propagating along the two paths from the source to the two receiving antennas A and B, acquired a phase difference, φ that depends on the angle θ between the incident plane wavefront and the interferometer baseline, the relative azimuthal term between the two receiving antennas φ_ℓ due to the beam vorticity ($\varphi_\ell = 0$ when $\ell = 0$ and $\varphi_\ell = \pi$ when $\ell = 1$) and a generic additional spatial/temporal phase term φ_0 introduced by the experimental setup (e.g. cable delay, non perfect parallelism of the receiving antennas, etc.),

$$\varphi = 2\pi \frac{d \sin\theta}{\lambda} + \varphi_\ell + \varphi_0 \tag{8.4.1}$$

The parameter d is the separation of the two antennas. The signal was collected equally by antenna A and B in phase and the signal of antenna A arrives at the signal adder π out of phase with respect that of antenna B because of the electric $\lambda/2$ cable delay, resulting in a difference signal configuration, $|A - B|$ such that

$$|A - B| \approx |V_0 - V_0 e^{i\varphi}| = 2V_0 \sin\frac{\varphi}{2} \tag{8.4.2}$$

where V_0 is the voltage measured by the receiver at the antenna cable end. The direction of the transmitter, in the ideal case, is identified by a minimum or absence of signal. A maximum is

obtained when

$$\varphi = (k+1)\pi$$

and k is an integer. By introducing an additional phase term to the antenna A, one can change the pointing direction of the antenna system, in such a way the segment AB, delimited by the two antennas, would rigidly rotate around the field singularity in the direction orthogonal to the propagation of the EM signal, with the result of moving the position of the null interference fringes and compensate for the additional phase term and inclination of the interferometric base with respect to the direction of the source. Alternatively, a similar compensation is obtained by moving the antenna A along the direction of the source by a quantity $\Delta x = \lambda n/2\pi$. Consequently, the phase difference between the two paths can be written as

$$\varphi = 2\pi \frac{d \sin\theta}{\lambda} - n \tag{8.4.3}$$

The parameter n can be adjusted to improve the tuning of the receiving system and read a signal minimum in the exact direction of the transmitting antenna. Here, n is negative when the antenna A is moved towards the source.

If the beam carries OAM, the phase distribution of the wavefront arriving to antenna A and B will exhibit a characteristic topological signature. In the simplest case, when the centre of the vortex coincides with the centre of the interferometer, the two antennas will experience a phase gap due to the OAM of the EM wave $\varphi_{OAM} = \ell\pi$ and a maximum of the signal is obtained when the phase factor is

$$\varphi = 2\pi \frac{d \sin\theta}{\lambda} - n + \ell\pi = (k+1)\pi; \quad k \in \mathbb{Z} \tag{8.4.4}$$

where $\mathbb{Z}$ is the set of positive and negative integer numbers. When $\ell = 1$, a maximum for the vortex is achieved when $n = 0$ and $k = 0$. Because of destructive interference, at the same time, the $\ell = 0$ signal intensity will experience a minimum. On the other hand, a maximum, for the $\ell = 0$ mode will be found when $n = -\lambda/2$, corresponding to a minimum for the vortex. Following these considerations, we aligned the interferometer on the center of the singularity so to have the field singularity in the centre of the segment joining the two receiving antennas (i.e. the interferometer basis) and obtain the phase gap $\varphi_\ell = \pi$ between the two antennas expected during the reception of the $\ell = 1$ vortex. To better optimize the interference fringe structure we oriented the baseline by an inclination $\theta \sim 10^\circ$ with respect to the balcony in order to be orthogonal to the incoming beam.

In order to have a simple, straightforward practical method to discriminate the two orthogonal OAM channels, transmitted on the same carrier frequency, we frequency modulated them with constant-level audio signals at different modulation frequencies (400 Hz and 1000 Hz for the untwisted and twisted wave, respectively) by injecting a -5dBm monophonic audio signal in the video band of each transmitter. The radio signal was received by the two Yagi-Uda antennas, summed by the a beam adder module and then re-converted in a monophonic audio signal, subsequently digitally sampled, recorded and analyzed in real time with 32-bit resolution. Each dataset so produced is 22870008 bytes long.

The total signal loss measured in the receiving line of the interferometer was 6 dB. We attribute this to cables losses the use of the 3 dB a beam adder module (power splitter-combiner Mini-Circuits ZX10-2-42+). In order to reduce the power of the signal we added a 10dB attenuator in the receiving line to reduce the power of the signal so that the audio digitalizer connected to the receiver output would not saturate due to overvoltage. In a conventional single-antenna receiver set up for detection of linear momentum only, the two radio signals were audible simultaneously. By mechanically moving the antenna A with respect to B to select one of the two orthogonal OAM beams, one signal was alternately suppressed with respect to the other due to the different spatial phase signature of the two OAM states. We adjusted the baseline in order to optimize the discrimination of the two different OAM channels by movements of antenna A. As a frequency modulation transmission has the property of generating a constant amplitude output, we adjusted the output of the two transmitters to measure the same positive output voltage in the FM reception, 1 Vcc (Volt in continuous current) for each channel. In this way we were able to characterize the transition between equal-intensity twisted and untwisted channels. Fig. 8.8 shows the maximum positive voltage of the signal measured at the output of the antenna receiver and amplifier. The untwisted beam (blue line) showed destructive interference in the interval 8.5 $-$ 9.4 cm from the initial antenna position. In the corresponding audio track, that the carrier disappears and the 400 Hz tone is suddenly replaced by white noise, which appears louder due to the automatic gain control, AGC, of the receiver, indicating destructive interference. This behaviour is seen in two other smaller regions and is possibly due to effects of the secondary Yagi lobes that were not considered in our autocorrelation analysis. The twisted beam (red line) , on the other hand, presented a richer forest of alternating maxima and minima; only near the initial position of the antenna (0.4 $-$ 1.6 cm) a wide region of total destructive interference was observed.

In Fig. 8.9 we display the audio frequency spectrum, from 0 to 3 kHz, of the two separate OAM channels ($\ell = 0$, upper panel, $\ell = 1$, middle panel) obtained from the best acquisition made during our OAM tuning experiments.

Each single channel is tuned when the other one experiences destructive interference and the corresponding audio tone disappears. In the lower panel we show the spectrum of both the channels superposed measured outside the regions of destructive interference. This result is confirmed by the Tolonen-Karjalainen autocorrelation for multi-pitch detection [111], as shown in Fig. 8.10. Whereas the $\ell = 0$ mode always showed a clear autocorrelation, the $\ell = 1$ mode always presents a series of harmonic tones at higher frequencies.

Already with this setup one can obtain four physically distinct channels on the same frequency by additionally introducing the use of polarization (spin angular momentum, SAM) that is independent from OAM; the vector sum of SAM and OAM is the total angular momentum which is a conserved quantity. A further multiplication of a factor five after the implementation of multiplexing would yield a total of 20 channels in the same frequency. The utilization of multiport techniques can increase the capacity further.

8.5 Conclusions

Our results may open new perspectives in wireless communications and demonstrate the possibility of tuning along different orbital angular momentum channels without increasing the frequency bandwidth from a physical principle. Looking back to the past, history books report that Marconi invented wireless telegraph and from that the communication world spread its branches in all directions [101]. All the wireless devices are based on various forms of phase, frequency and/or amplitude modulation of the electromagnetic (EM) radiation. In order that many different broadcasting stations could transmit simultaneously without overlapping their radio signals, Marconi suggested a division of the available spectrum of radio frequencies in different bands [106]. Nowadays, the wide use of wireless has unavoidably led to the saturation of all available frequency bands, even with the adoption of artificial techniques to increase the band capacity. With this experiment we have shown that the use of orbital angular momentum states might dramatically increase the capacity of any frequency band, allowing the use of dense coding techniques in each of these new vortex radio channels. This might represent a concrete proposal for the solution of the band saturation problem. Moreover, our experimental findings show that the propagation of the physical properties of twisted radio beams is preserved after the propagation. We found that the spatial phase signature was preserved even in the far-field region and for incoherent non-monochromatic wave beams. These results open new concrete perspectives for science, including astronomy and in particular radio-astronomy.

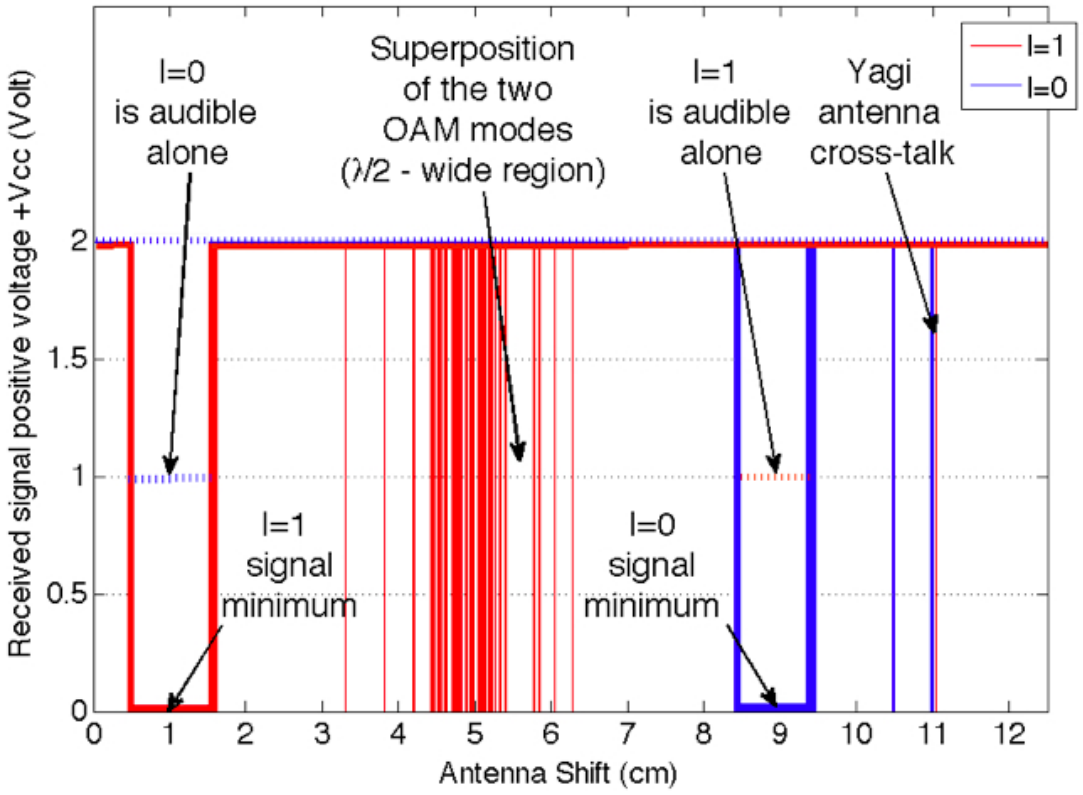

Figure 8.8: Diagram of the monophonic audio recordings of the twisted/untwisted beams. The output of the two transmitters were adjusted to ensure the same maximum input voltage of 2 volts when both channels were present, and 1 Vcc max for each individual channel. The first minimum is found at around 1 cm of antenna shift for the $\ell = 1$ mode. Here the $\ell = 0$ channel has a maximum and the associated audio tone is clearly audible. The same was found for the $\ell = 0$ mode around the 9 cm antenna position. The inner boundaries of the two minima regions are separated in distance by half a radio wavelength. Between these positions there was a forest of minima of the $\ell = 1$ mode, a phenomenon due to the sampling of the field from a finite-sized antenna. Beyond the minimum located at 9 cm, two additional alternating signal minima due to the cross talk of the two Yagi-Uda antennas were found.

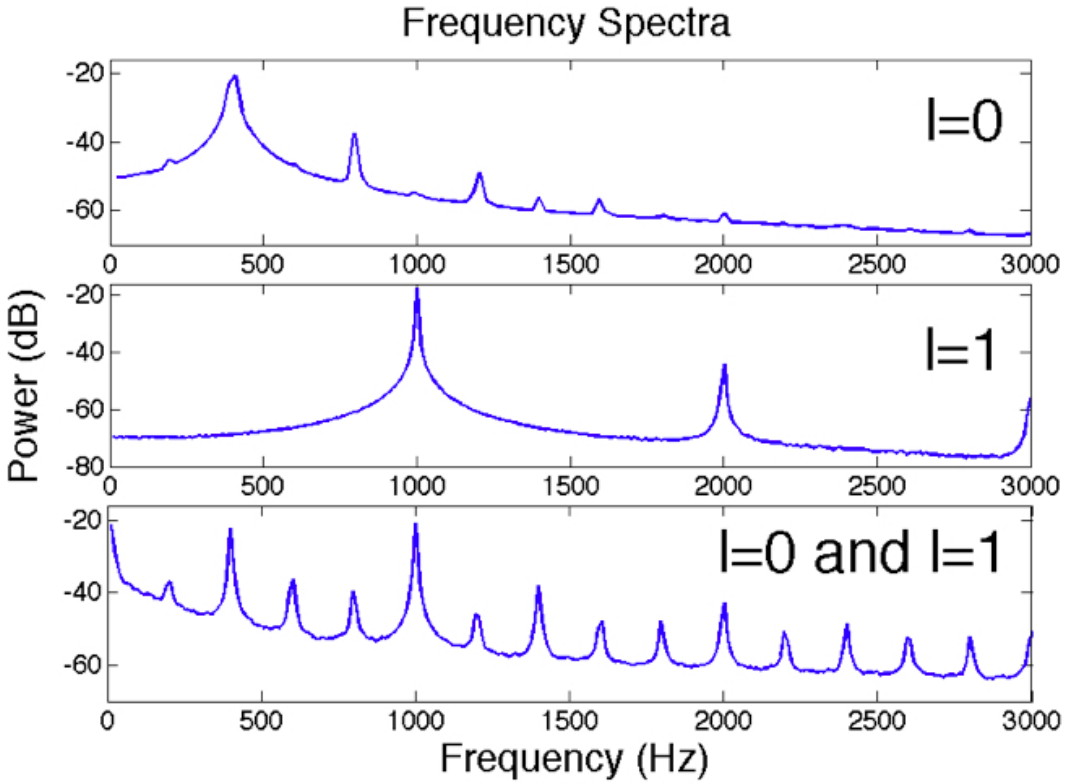

Figure 8.9: Spectral analysis of the demodulated audio signal when the antenna interferometer was tuned by the spatial motion of one antenna to receive two independent and superposed OAM modes in the same frequency band. The spectra are truncated at 3 kHz for better clarity. Upper panel: audio frequency spectrum of the beam in the region where the interferometer is tuned for the $\ell = 0$ mode signal. Clearly visible is the main peak at 400 Hz followed by the higher-frequency harmonics. The power of the signal is distributed with decreasing power at higher frequencies. Middle panel: audio spectrum in the position where only the $\ell = 1$ mode audio signal is audible. Also in this case the power is distributed with less power for higher frequency harmonics of the 1 kHz main frequency. In both the two spectra there are no spurious frequencies introduced by the other twisted signal. Lower panel: audio spectrum of the signal where the two twisted beams are not separated. Both the audio frequencies are visible.

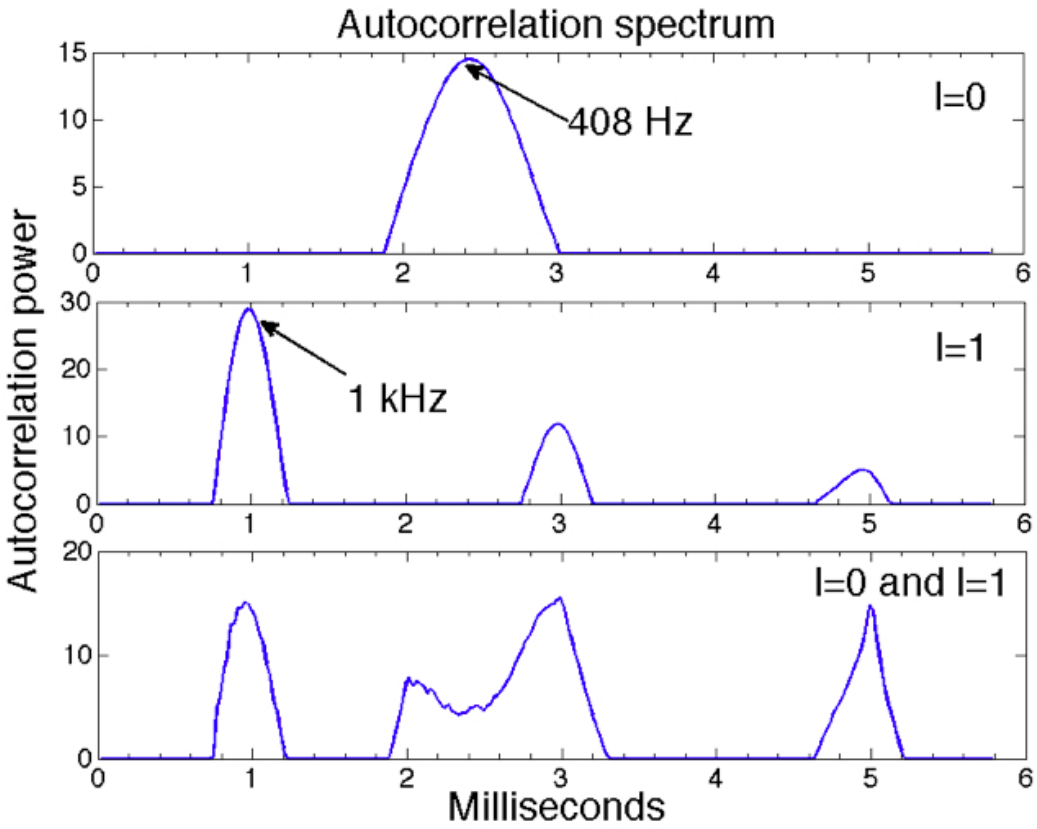

Figure 8.10: Autocorrelation spectral analysis of the audio transmission in three different antenna positions. Upper panel: the $\ell = 0$ mode ($\sim$ 408 Hz) detectable when the antenna is at a position between 0.4 and 1.6 centimetres and (middle panel) the $\ell = 1$ (1 KHz), from 8.5 cm to 9.4 cm, with the exception of the two small intervals where a cross talk of the two antennas was observed. In the lower panel, the superposition of both the audio signals at 400 Hz and 1 kHz is clearly evident, showing the impossibility of separating the two channels when the moving antenna is in the interval (1.8 - 8) cm.

Bibliography

[1] L. Allen, "Orbital angular momentum of light and the transformation of Laguerre-Gaussian laser modes," *Physical Review A*, vol. 45, no. 11, pp. 8185–8189, 1992.

[2] P. Coullet, L. Gil, and F. Rocca, "Optical vortices," *Optics Communications*, vol. 73, no. 5, pp. 403–408, 1989.

[3] D. M. Palacios, I. D. Maleev, A. S. Marathay, and G. A. Swartzlander, "Spatial correlation singularity of a vortex field," *Physical Review Letters*, vol. 92, p. 143905, Apr 2004.

[4] D. Grier, "A revolution in optical manipulation," *Nature*, Jan 2003.

[5] A. Vaziri, G. Weihs, and A. Zeilinger, "Superpositions of the orbital angular momentum for applications in quantum experiments," *Journal of Optics B: Quantum and Semiclassical Optics*, vol. 4, p. S47, 2002.

[6] F. Tamburini, G. Anzolin, G. Umbriaco, A. Bianchini, and C. Barbieri, "Overcoming the Rayleigh Criterion Limit with Optical Vortices," *Physical Review Letters*, vol. 97, no. 16, p. 163903, 2006.

[7] G. Foo, D. M. Palacios, and G. A. Swartzlander, Jr., "Optical vortex coronagraph," *Optics Letters*, vol. 30, pp. 3308–3310, Dec. 2005.

[8] M. W. Beijersbergen, R. P. C. Coerwinkel, M. Kristensen, and J. P. Woerdman, "Helical-wavefront laser beams produced with a spiral phaseplate," *Optics Communications*, vol. 112, pp. 321–327, Dec 1994.

[9] V. Y. Bazhenov, M. V. Vasnetsov, and M. S. Soskin, "Laser beams with wave front screw dislocations," *Pis'ma v Zhurnal Eksperimental'noi i Teoreticheskoi Fiziki (ISSN 0370-274X)*, vol. 52, pp. 1037–1039, 1990.

[10] A. J. Fresnel, *Mémoire sur la diffraction de la lumière*, vol. 1. Annales de la Chemie et de Physique, 2nd series, 1816.

[11] C. Huygens, “Traité de la lumiere,” *Leyden: Pierre van der Aa*, 1690.

[12] M. Born and E. Wolf, *Principles of optics*. Cambridge University Press, Jan 1999.

[13] G. R. Kirchhoff, “Towards a theory of light rays,” *Annalen der Physik und Chemie*, vol. 18, pp. 663–695, 1883.

[14] D. O’Shea, *Diffractive optics: design, fabrication, and test*. Society of Photo Optical, 2004.

[15] A. W. Lohmann and D. P. Paris, “Binary fraunhofer holograms, generated by computer,” *Applied Optics*, vol. 6, no. 10, pp. 1739–1748, 1967.

[16] B. Kress and P. Meyrueis, *Applied digital optics: from micro-optics to nanophotonics*. Wiley, 2009.

[17] R. E. Fischer, *Optical system design, second edition*. McGraw-Hill, Jan 2008.

[18] D. Gabor, “A new microscopic principle,” *Nature*, vol. 161, no. 4098, pp. 777–778, 1948.

[19] E. Leith and J. Upatnieks, “Wavefront reconstruction and communication theory,” *J. Opt. Soc. Am*, vol. 52, pp. 1123–1134, 1962.

[20] B. Brown and A. Lohmann, “Computer-generated binary holograms,” *IBM Journal of Research and Development*, vol. 13, no. 2, pp. 160–168, 1969.

[21] O. K. Ersoy, *Diffraction, fourier optics, and imaging*. Jossey-Bass, 2007.

[22] M. Berry, “Making waves in physics,” *Nature*, p. 21, 2000.

[23] J. F. Nye, “The motion and structure of dislocations in wavefronts,” *Proceedings of the Royal Society of London. Series A, Mathematical and Physical Sciences*, vol. 378, no. 1773, pp. 219–239, 1981.

[24] M. S. Soskin, V. N. Gorshkov, M. V. Vasnetsov, J. T. Malos, and N. R. Heckenberg, “Topological charge and angular momentum of light beams carrying optical vortices,” *Physical Review A*, vol. 56, pp. 4064–4075, Nov. 1997.

[25] S. J. van Enk and G. Nienhuis, “Eigenfunction description of laser beams and orbital angular momentum of light,” *Optics Communications*, vol. 94, pp. 147–158, Nov. 1992.

[26] F. Tamburini and D. Vicino, “Photon wave function: A covariant formulation and equivalence with qed,” *Physical Review A*, vol. 78, no. 5, p. 52116, 2008.

[27] W. Heitler, *The quantum theory of radiation*. Dover Pubns, 1984.

[28] L. Allen and M. J. Padgett, “The Poynting vector in Laguerre-Gaussian beams and the interpretation of their angular momentum density,” *Optics Communications*, vol. 184, pp. 67–71, Oct. 2000.

[29] M. J. Padgett and L. Allen, "The poynting vector in laguerre-gaussian laser modes," *Optics Communications*, vol. 121, no. 1-3, pp. 36–40, 1995.

[30] J. D. Jackson and R. F. Fox, "Classical electrodynamics," *American Journal of Physics*, vol. 67, p. 841, 1999.

[31] B. Thidé, *Electromagnetic field theory. 2nd edition*. Dover Publications (in press), 2012.

[32] A. T. O'Neil, I. MacVicar, L. Allen, and M. J. Padgett, "Intrinsic and extrinsic nature of the orbital angular momentum of a light beam," *Physical Review Letters*, vol. 88, p. 53601, Feb 2002.

[33] J. Leach, M. J. Padgett, S. M. Barnett, S. Franke-Arnold, and J. Courtial, "Measuring the orbital angular momentum of a single photon," *Physical Review Letters*, vol. 88, p. 257901, Jun 2002.

[34] A. Mair, A. Vaziri, G. Weihs, and A. Zeilinger, "Entanglement of the orbital angular momentum states of photons," vol. 412, pp. 313–316, 2001.

[35] M. Berry, "Paraxial beams of spinning light," *Proceedings of SPIE*, vol. 3487, p. 6, Aug 1998.

[36] R. Zambrini and S. M. Barnett, "Quasi-intrinsic angular momentum and the measurement of its spectrum," *Physical Review Letters*, vol. 96, p. 113901, Mar 2006.

[37] J. Nye and M. Berry, "Dislocations in wave trains," *Proceedings of the Royal Society of London. Series A, Mathematical and Physical Sciences*, pp. 165–190, 1974.

[38] G. A. Swartzlander Jr. and C. T. Law, "Optical vortex solitons observed in Kerr nonlinear media," *Physical Review Letters*, vol. 69, no. 17, pp. 2503–2506, 1992.

[39] F. T. Arecchi, G. Giacomelli, P. L. Ramazza, and S. Residori, "Vortices and defect statistics in two-dimensional optical chaos," *Physical Review Letters*, vol. 67, no. 27, pp. 3749–3752, 1991.

[40] K. O'Holleran, M. Padgett, and M. Dennis, "Topology of optical vortex lines formed by the interference of three, four, and five plane waves," *Optics Express*, vol. 14, pp. 3039–3044, 2006.

[41] S. Franke-Arnold, L. Allen, and M. Padgett, "Advances in optical angular momentum," *Laser & Photonics Reviews*, vol. 2, no. 4, pp. 299–313, 2008.

[42] A. A. Ishaaya, N. Davidson, and A. A. Friesem, "Very high-order pure laguerre-gaussian mode selection in a passive q-switched nd: Yag laser," *Optics Express*, vol. 27, pp. 1908–1910, 2002.

[43] M. W. Beijersbergen, L. Allen, H. E. L. O. van der Veen, and J. P. Woerdman, "Astigmatic laser mode converters and transfer of orbital angular momentum," *Optics Communications*, vol. 96, pp. 123–132, Feb 1993.

[44] J. Arlt, K. Dholakia, L. Allen, and M. J. Padgett, "The production of multiringed Laguerre-Gaussian modes by computer-generated holograms," *Journal of Modern Optics*, vol. 45, pp. 1231–1237, June 1998.

[45] N. R. Heckenberg, R. McDuff, C. P. Smith, and A. G. White, "Generation of optical phase singularities by computer-generated holograms," *Optics Letters*, vol. 17, pp. 221–223, Feb 1992.

[46] A. Y. Bekshaev and A. I. Karamoch, "Spatial characteristics of vortex light beams produced by diffraction gratings with embedded phase singularity," *Optics Communications*, vol. 281, pp. 1366–1374, Mar 2008. Elsevier B.V.

[47] S. S. R. Oemrawsingh, J. A. W. van Houwelingen, E. R. Eliel, J. P. Woerdman, E. J. K. Verstegen, J. G. Kloosterboer, and G. W. 't Hooft, "Production and characterization of spiral phase plates for optical wavelengths," *Applied Optics*, vol. 43, no. 3, pp. 688–694, 2004.

[48] E. B. Kley, "Continuous profile writing by electron and optical lithography," *Microelectronic Engineering*, vol. 34, pp. 261–298, 1997.

[49] M. Prasciolu, F. Tamburini, G. Anzolin, E. Mari, M. Melli, A. Carpentiero, C. Barbieri, and F. Romanato, "Fabrication of a three-dimensional optical vortices phase mask for astronomy by means of electron-beam lithography," *Microelectronic Engineering*, vol. 86, no. 4-6, pp. 1103–1106, 2009.

[50] E. Mari, G. Anzolin, F. Tamburini, M. Prasciolu, G. Umbriaco, A. Bianchini, C. Barbieri, and F. Romanato, "Fabrication and testing of ℓ= 2 optical vortex phase masks for coronography," *Optics Express*, vol. 18, pp. 2339–2344, 2010.

[51] J. H. Lee, G. Foo, E. G. Johnson, and G. A. Swartzlander, "Experimental verification of an optical vortex coronagraph," *Physical Review Letters*, vol. 97, p. 53901, Aug 2006.

[52] G. A. Swartzlander, Jr, "Peering into darkness with a vortex spatial filter," *Optics Letters*, vol. 26, no. 8, pp. 497–499, 2001.

[53] D. Ganic, X. Gan, M. Gu, M. Hain, S. Somalingam, S. Stankovic, and T. Tschudi, "Generation of doughnut laser beams by use of a liquid-crystal cell with a conversion efficiency near 100%," *Optics Letters*, vol. 27, no. 15, pp. 1351–1353, 2002.

[54] G. A. Swartzlander, Jr., "Achromatic optical vortex lens," *Optics Letters*, vol. 31, pp. 2042–2044, Jul 2006.

[55] B. Lyot, "The study of the solar corona and prominences without eclipses (George Darwin Lecture, 1939)," *Monthly Notices of the Royal Astronomical Society*, vol. 99, p. 538, May 1939.

[56] A. Quirrenbach, "Coronographic methods for the detection of terrestrial planets," *Conclusions from a workshop held February 02-06, 2004 at Leiden University*, pp. 1–105, Feb 2005.

[57] E. Serabyn, D. Mawet, and R. Burruss, "An image of an exoplanet separated by two diffraction beamwidths from a star," *Nature*, vol. 464, pp. 1018–1020, Apr 2010.

[58] D. Mawet, P. Riaud, O. Absil, and J. Surdej, "Annular groove phase mask coronagraph," *The Astrophysical Journal*, vol. 633, no. 2, pp. 1191–1200, 2005.

[59] O. Guyon, E. A. Pluzhnik, M. J. Kuchner, B. Collins, and S. T. Ridgway, "Theoretical limits on extrasolar terrestrial planet detection with coronagraphs," *The Astrophysical Journal Supplement Series*, vol. 167, pp. 81–99, 2006.

[60] A. Ferrari, R. Soummer, and C. Aime, "Introduction to stellar coronagraphy," *Comptes Rendus Physique*, vol. 8, no. 3, pp. 277–287, 2007.

[61] E. Hecht, *Optics 4th edition*. Addison-Wesley Publishing Company, 2001.

[62] O. Guyon, "Phase-induced amplitude apodization of telescope pupils for extrasolar terrestrial planet imaging," *Astronomy and Astrophysics*, vol. 404, p. 379, Jun 2003.

[63] F. Roddier and C. Roddier, "Stellar coronograph with phase mask," *Publications of the Astronomical Society of the Pacific*, vol. 109, p. 815, 1997.

[64] L. Abe, F. Vakili, and A. Boccaletti, "The achromatic phase knife coronagraph," *Astronomy and Astrophysics*, vol. 374, pp. 1161–1168, Aug 2001.

[65] D. Mawet, E. Serabyn, K. Liewer, R. Burruss, J. Hickey, and D. Shemo, "The vector vortex coronagraph: Laboratory results and first light at palomar observatory," *The Astrophysical Journal*, vol. 709, p. 53, 2010.

[66] D. Rouan, P. Riaud, A. Boccaletti, Y. Clénet, and A. Labeyrie, "The four-quadrant phase-mask coronagraph. i. principle," *Publications of the Astronomical Society of the Pacific*, vol. 112, pp. 1479–1486, Nov 2000.

[67] G. Anzolin, F. Tamburini, A. Bianchini, and C. Barbieri, "Method to measure off-axis displacements based on the analysis of the intensity distribution of a vortex beam," *Physical Review A*, vol. 79, pp. 033845–+, Mar. 2009.

[68] E. Mari, F. Tamburini, G. A. Swartzlander, A. Bianchini, C. Barbieri, F. Romanato, and B. Thidé, "Sub-rayleigh optical vortex coronagraphy," *Optics Express*, vol. 20, pp. 2445–2451, Jan 2012.

[69] C. Jenkins, "Optical vortex coronagraphs on ground-based telescopes," *Monthly Notices of the Royal Astronomical Society*, vol. 384, pp. 515–524, Feb 2008.

[70] G. Anzolin, F. Tamburini, A. Bianchini, G. Umbriaco, and C. Barbieri, "Optical vortices with starlight," *Astronomy and Astrophysics*, vol. 488, pp. 1159–1165, Sept. 2008.

[71] D. L. Fried, "Probability of getting a lucky short-exposure image through turbulence," *Optical Society of America*, vol. 68, pp. 1651–1657, Dec 1978.

[72] N. M. Law, C. D. Mackay, and J. E. Baldwin, "Lucky imaging: high angular resolution imaging in the visible from the ground," *Astronomy and Astrophysics*, vol. 446, pp. 739–745, 2006.

[73] R. N. Tubbs, J. E. Baldwin, C. D. Mackay, and G. C. Cox, "Diffraction-limited ccd imaging with faint reference stars," *Astronomy and Astrophysics*, vol. 387, pp. L21–L24, 2002.

[74] M. Scardia, "Micrometer measurements of visual double stars - part three -," *Astronomische Naschrichten*, vol. 308, pp. 271 – 281, Jan 1987.

[75] E. Mari, F. Tamburini, C. Barbieri, A. Bianchini, M. Prasciolu, M. Massari, and F. Romanato, "Fabrication and testing of phase masks for optical vortex coronagraph to observe extrasolar planets," *Proceedings of SPIE*, vol. 7735, p. 773534, Jan 2010.

[76] C. E. Shannon, "Communication in the presence of noise," *Proceedings of the IRE*, vol. 37, no. 1, pp. 10–21, 1949.

[77] J. C. Dainty, "Laser speckle and related phenomena," *Laser Speckle and Related Phenomena*, Jan 1984.

[78] E. Jakeman and W. T. Welford, "Speckle statistics in imaging systems," *Optics Communications*, vol. 21, pp. 72–79, Apr 1977.

[79] A. Boccaletti, P. Riaud, P. Baudoz, J. Baudrand, D. Rouan, D. Gratadour, F. Lacombe, and A. M. Lagrange, "The four-quadrant phase mask coronagraph. iv. first light at the very large telescope," *The Publications of the Astronomical Society of the Pacific*, vol. 116, pp. 1061–1071, Nov 2004.

[80] D. Mawet, E. Serabyn, K. Liewer, C. Hanot, S. McEldowney, D. Shemo, and N. O'Brien, "Optical vectorial vortex coronagraphs using liquid crystal polymers: theory, manufacturing and laboratory demonstration," *Optics Express*, vol. 17, pp. 1902–1918, Feb 2009.

[81] G. A. Swartzlander Jr, E. L. Ford, R. S. Abdul-Malik, L. M. Close, M. A. Peters, D. M. Palacios, and D. W. Wilson, "Astronomical demonstration of an optical vortex coronagraph," *Optics Express*, vol. 16, p. 10200, Jun 2008.

[82] J. W. Strutt and L. Rayleigh, "On the electromagnetic theory of light," *Philosophical Magazine*, vol. 12, pp. 81–101, 1881.

[83] K. G. Puschmann and F. Kneer, "On super-resolution in astronomical imaging," *Astronomy and Astrophysics*, vol. 436, no. 1, pp. 373–378, 2005.

[84] N. I. Zheludev, "What diffraction limit?," *Nature materials*, vol. 7, no. 6, pp. 420–422, 2008.

[85] Z. Jacob, L. Alekseyev, and E. Narimanov, "Optical hyperlens: Far-field imaging beyond the diffraction limit," *Optics Express*, vol. 14, no. 18, pp. 8247–8256, 2006.

[86] X. Zhang and Z. Liu, "Superlenses to overcome the diffraction limit," *Nature materials*, vol. 7, no. 6, pp. 435–441, 2008.

[87] A. Ranfagni, D. Mugnai, and R. Ruggeri, "Beyond the diffraction limit: Super-resolving pupils," *Journal of applied physics*, vol. 95, p. 2217, 2004.

[88] M. Pitchumani, H. Hockel, W. Mohammed, and E. Johnson, "Additive lithography for fabrication of diffractive optics," *Applied optics*, vol. 41, no. 29, pp. 6176–6181, 2002.

[89] G. A. Swartzlander, Jr., "The optical vortex coronagraph," *Journal of Optics A: Pure and Applied Optics*, vol. 11, p. 094022, Sept. 2009.

[90] G. A. Swartzlander, Jr., "Obtaining spatial information from an extremely unresolved source," *Optics Letters*, Jan 2011.

[91] B. Thidé, H. Then, J. Sjöholm, K. Palmer, J. Bergman, T. D. Carozzi, Y. N. Istomin, N. H. Ibragimov, and R. Khamitova, "Utilization of photon orbital angular momentum in the low-frequency radio domain," *Physical Review Letters*, Jan 2007.

[92] S. Mohammadi, L. Daldorff, K. Forozesh, B. Thidé, J. Bergman, B. Isham, R. Karlsson, and T. Carozzi, "Orbital angular momentum in radio: Measurement methods," *Radio Science*, vol. 45, no. 4, p. RS4007, 2010.

[93] R. Compton Jr, "The tripole antenna: An adaptive array with full polarization flexibility," *Antennas and Propagation, IEEE Transactions on*, vol. 29, no. 6, pp. 944–952, 1981.

[94] D. B. Nguyen and S. Berntsen, "The reconstruction of the relative phases and polarization of the electromagnetic field based on amplitude measurements," *Microwave Theory and Techniques, IEEE Transactions on*, vol. 40, no. 9, pp. 1805–1811, 1992.

[95] J. Torres and L. Torner, *Twisted Photons: Applications of Light with Orbital Angular Momentum*. Wiley-VCH, 2011.

[96] M. Berry, "Optical vortices evolving from helicoidal integer and fractional phase steps," *Journal of Optics A Pure and Applied Optics*, vol. 6, no. 2, pp. 259–268, 2004.

[97] R. Čelechovský and Z. Bouchal, "Optical implementation of the vortex information channel," *New Journal of Physics*, vol. 9, p. 328, 2007.

[98] G. Gibson, J. Courtial, M. J. Padgett, M. Vasnetsov, V. Pas'ko, S. M. Barnett, and S. Franke-Arnold, "Free-space information transfer using light beams carrying orbital angular momentum," *Optics Express*, vol. 12, pp. 5448–5456, Sep 2005.

[99] J. T. Barreiro, T. Wei, and P. Kwiat, "Beating the channel capacity limit for linear photonic superdense coding," *Nature Physics*, vol. 4, no. 4, pp. 282–286, 2008.

[100] J. B. Pors, S. S. R. Oemrawsingh, A. Aiello, M. P. Van Exter, E. R. Eliel, G. W. 't Hooft, and J. P. Woerdman, "Shannon dimensionality of quantum channels and its application to photon entanglement," *Physical Review Letters*, vol. 101, no. 12, p. 120502, 2008.

[101] O. E. Dunlap, *Marconi: The man and his wireless*. Arno Press, 1971.

[102] G. Li and G. Stüber, *Orthogonal frequency division multiplexing for wireless communications*. Springer, 2006.

[103] G. Molina-Terriza, J. P. Torres, and L. Torner, "Twisted photons," *Nature Physics*, vol. 3, p. 305, May 2007.

[104] S. Uda, "High angle radiation of short electric waves," *Proceedings of the Institute of Radio Engineers*, vol. 15, no. 5, pp. 377–385, 1927.

[105] H. Yagi, "Beam transmission of ultra short waves," *Proceedings of the Institute of Radio Engineers*, vol. 16, no. 6, pp. 715–740, 1928.

[106] G. Marconi and G. Giorgi, *Scritti di Guglielmo Marconi*. Reale accademia d'Italia, 1941.

[107] F. Tamburini, B. Thidé, G. Molina-Terriza, and G. Anzolin, "Twisting of light around rotating black holes," *Nature Physics*, vol. 7, pp. 195–197, Feb 2011.

[108] F. Tamburini, E. Mari, A. Sponselli, B. Thidé, A. Bianchini, and F. Romanato, "Encoding many channels on the same frequency through radio vorticity: first experimental test.," *Accepted for publication by New Journal of Physics*, 01 2012.

[109] L. Torner, J. P. Torres, and S. Carrasco, "Digital spiral imaging," *Optics Express*, vol. 13, pp. 873–881, Feb 2005.

[110] K. Chang and J. Wiley, *RF and microwave wireless systems*. Wiley Online Library, 2000.

[111] T. Tolonen and M. Karjalainen, "A computationally efficient multipitch analysis model," *Speech and Audio Processing, IEEE Transactions on*, vol. 8, no. 6, pp. 708–716, 2000.